1. Alma Mater Studiorum – Università di Bologna

DOTTORATO DI RICERCA IN

NANOSCIENZE PER LA MEDICINA E PER L'AMBIENTE

Ciclo 33

Settore Concorsuale: 03/B1 - FONDAMENTI DELLE SCIENZE CHIMICHE E SISTEMI INORGANICI

Settore Scientifico Disciplinare: CHIM03 – CHIMICA GENERALE E INORGANICA

NANOSTRUCTURED LUMINESCENT CHEMOSENSORS FOR ENVIRONMENTAL AND BIOMEDICAL APPLICATIONS

Presentata da: Liviana Mummolo

Coordinatore Dottorato

Prof. Dario Braga

Supervisore

Prof. Luca Prodi

Co-supervisore

Prof. Massimiliano Bonafé

Esame finale anno 2021

List of abbreviations

A	Adenine
BPA	Bisphenol A
bpy	2,2’-bipyridine
C	Cytosine
DEAC	Diethylamino Coumarin
DEA	Diethanolamine
DLS	Dynamic Light Scattering
DMF	Dimethylformamide
DPPZ	Dipyrido[3,2-a:2’,3’-c]phenazin
DoF	Degree of functionalization
dsDNA	Double strand Deoxyribonucleic Acid
EDC·HCl	N-(3-Dimethylaminopropyl)-N′-ethylcarbodiimide hydrochloride
FRET	Forster Resonance Energy Transfer
G	Guanine
EP	Emerging pollutants
EPR	Enhanced Permeability and Retention
F-127	Pluronic F-127
FBS	Fetal bovine serum
HA	Hyaluronic Acid
L	4-(4’-methyl-[2,2’-bipyridin]-4-yl)butan-1-amine
L_a	4,4’-bis[methylen-(1,4,7,10-tetraazacyclododecane)]-2,2’-bipyridine
H-bonds	Hydrogen Bond
HDPs	Hairpin DNA probes
H-FRET	High FRET state
IKK	IκB kinase
L-FRET	Low FRET state
NF-κB	Nuclear Factor kappa-light-chain-enhancer of activated B cells
PA	1-Aminopyrene
PBS	Phosphate Buffer Saline
PC3	Prostate cancer cells
PCC	Pearson correlation coefficients
PEG	Polyethylene Glycol
PFA	Para formaldehyde
PluSNP	Pluronic F-127 Silica Nanoparticle
PPCPs	pharmaceutical and personal care products
PMA	1-Pyrenemethylamine

PPO	Polypropylene Oxide
QY	Quantum Yield
RB	Rhodamine B
RITC	Rhodamine isothiocyanate
Ru(bpy)	Cis-$[Ru(bpy)_2(L)]Cl_2$
Ru(DPPZ)	$[Ru(bpy)(L)(DPPZ)](PF_6)_2$
RU	Repetitive unit
Sulfo-NHS	N-Hydroxysulfosuccinimide sodium salt
T	Thymine
T6	Thymine 6
T33	Thymine 33
TEOS	Tetra Ethyl Orthosilicate
TEA	Trimethylamine
TF	Transcriptor factors
T_m	Melting temperature
TMSCl	Trimethylsilyl chloride
U	Uracil

Contents

Chapter 1 – General introduction ... 1

- 1.1 Biocompatible Nanomaterials for Biomedical Applications ... 1
- 1.2 Biosensors ... 4
  - 1.2.1 Optical biosensors ... 5
- 1.3 Nanomaterials for bio-sensing applications ... 8
  - 1.3.1 DNA: a target and a probe ... 9
  - 1.3.1.3. DNA-based BIOSENSORS ... 13
- 1.4 Hyaluronic acid ... 14
  - 1.4.1 Hyaluronic acid interaction with nanomaterials ... 15
- 1.5 References ... 17

Chapter 2 – ... 19

DNA-based probe for NF-κB protein detection in living cells ... 19

- 2.1 introduction ... 19
- 2.2 Materials and methods ... 21
- 2.3 Results and discussion ... 23
- 2.4 Conclusions ... 33
- 2.5 References ... 35

Chapter 3 - Derivatization of HA with dansyl chloride ... 36

- 3.1 Introduction ... 36
- 3.2 Materials and methods ... 37
  - 3.2.1 functionalization of hyaluronic acid with dansyl chloride ... 37
  - 3.2.2 synthesis of PluSNPs ... 39
- 3. 3 Results and discussion ... 39
  - 3.3.1 Synthesis and characterization of hyaluronic acid with dansyl chloride ... 39

3.3.1 Photophysical characterisation of HA@Dansyl 41

3.3.3 Interactions with nanomaterials 43

3.4 Conclusions 47

3.5 References 48

Chapter 4 - Derivatization of HA with pyrene 49

4.1 Introduction 49

4.2 Materials and methods 49

4.2.2 Functionalization of hyaluronic acid with 1-aminopyrene 50

4.2.3 Functionalization of hyaluronic acid with methyl-aminopyrene 51

4.3 Results and discussion 52

4.3.1- Synthesis and characterization of hyaluronic acid with aminopyrene 52

4.3.2 - Photophysical characterisation of HA@PA and HA@PMA 52

4.3.3 – interaction of HA@PA and nanomaterials 54

4.3.4 – interaction of HA@PMA and nanomaterials 58

4.4 Conclusions 61

4.5 References 63

Chapter 5 - Derivatization of HA with ruthenium complexes 64

5.1 Introduction 64

5.2 Materials and methods 65

5.2.1 Functionalization of hyaluronic acid with cis-$[Ru(bpy)_2(L)]Cl_2$ or $[Ru(bpy)(L)(DPPZ)](PF_6)_2$ 66

5.3 Results and discussion 66

5.3.1 Synthesis and characterization of HA@Ru derivatives 66

5.3.2 Photochemical characterization 67

5.3.3 Interactions among HA-$[Ru(bpy)_2(L)]Cl_2$ and PluSNPs 69

5.3.4 Interactions between HA@$[Ru(bpy)_2(L)]Cl_2$ and salmon sperm DNA..... 73

5.3.5 Interactions between HA-[Ru(bpy) (L)(DPPZ)]$(PF_6)_2$ and salmon sperm DNA ... 75

5.3.6 Interactions between HA-[Ru(bpy) (L)(DPPZ)]$(PF_6)_2$ and Hybrid DNA . 77

5.4 Conclusions ... 78

5.5 References ... 80

Chapter 6 – Supramolecular systems for BPA detection ... 81

6.1 Introduction ... 81

6.2 BPA detection through metal complex ... 82

6.2.1 Experimental section ... 82

6.2.2 Results and discussion ... 83

6.3 BPA detection with nanomaterials ... 90

6.3.1 Experimental section ... 90

6.3.2 Results and discussion ... 91

6.4 Conclusion ... 98

6.5 References ... 100

Chapter 7 – ... 101

General conclusions ... 101

APPENDIX - PRYNCIPLES OF PHOTOPHYSICS ... 127

A.1 ELECTRONIC EXCITED STATE, JABLOSNKY DIAGRAM ... 127

A.2 SOLVATOCHROMISM ... 129

A.3 ELECTRONIC EXCITATION ENERGY TRANSFER ... 131

A4 ELECTRONIC ABSORPTION SPECTRA ... 135

A5 LUMINESCENCE QUANTUM YIELD ... 136

A6 EXCITED STATE LIFETIME MEASUREMENTS ... 137

A.7 DYNAMIC LIGHT SCATTERING ... 138

Chapter 1 – General introduction

1.1 Biocompatible Nanomaterials for Biomedical Applications

In 2011, the European commission defined Nanomaterials as “A natural, incidental or manufactured material containing particles, in an unbound state or as an aggregate or as an agglomerate and where, for 50 % or more of the particles in the number size distribution, one or more external dimensions is in the size range 1 nm - 100 nm” [1]. At this scale, physical and chemical properties of materials differ from those in larger scale and their behaviour is governed by quantum mechanics. Moreover, regardless of their shape or composition, the key feature of nanomaterials is a large surface/volume ratio which influences their optical, mechanical or magnetic properties. These unique characteristics of nanomaterials made them suitable for a variety of applications, ranging from technology, computer science, food industry, telecommunications and medicine [2].

Indeed, in the last decades nanotechnology and nanomaterials found applications in the biomedical field including *in vitro* diagnostics, *in vivo* imaging, drug delivery, tissue engineering, particularly in the field of cancer diagnostics and therapy, but with an increasing attention in the treatment and diagnosis of other diseases, as cardiovascular, neurological and infectious diseases or autoimmune inflammations [3].

Nanomaterials for biomedical applications can be divided into the following groups, depending on their nature:

organic nanomaterials, as lipid arranging in liposome or micelles, polymers like PLGA, chitosan, hyaluronic acid, PLA forming nanoparticles, dendrimers or fibres.
inorganic nanomaterials, based on noble metals (Au, Pt, Ag), carbon-based (as fullerenes or nanotubes), oxide-based (as magnetic nanoparticles) or semiconductors;
mesoporous silica nanomaterials.[4]

Many efforts in understanding the nano-bio interactions and the relationships between the nanomaterial properties/structure and their activity led to the ability to rationally design nanomaterials and their safe use in nanomedicine.

What indeed makes nanomaterials such good candidates for several biomedical applications are a number of features. First of all, their size – which is comparable to the one of biomolecules – is potentially suitable for letting them being integrated into cellular uptake processes, via phagocytosis or pinocytosis [5]. Moreover, the possibility to tune their dimensions allows to control properties as their time of clearance or their accumulation in critical areas.

Indeed, a very useful strategy in cancer treatment is the one exploiting the so called EPR (Enhanced Permeability and Retention) effect. This phenomenon is caused by the state of hypoxia in cancer cells, which thus require more afflux of oxygen from the blood. This demand results in the phenomenon of angiogenesis, that is the creation of new blood vessels in proximity of cancer tissues. Thanks to their size, nanomaterials are big enough to enter and then to remain entrapped into the intricate newly vascularised area. Their accumulation is then selective for ill tissues, which experience higher permeability and retention compared to healthy ones. Typically, a strong EPR effect is reached using objects with sizes ranging from 10 to 200 nm [6].

Furthermore, the pharmacokinetics of several nanomaterials has been extensively studied, in order to understand their bio-distribution, bioavailability and time of clearance. In fact, not only their biocompatibility has been proved over several cell lines, but it has also been proved that several nanomaterials are characterized by high stability in physiological environment, which ensure a distance of action, an efficient bio-distribution and a constant protection of cargos from the external environment.

When administered in the systemic circulation, large particles are recognised by the reticuloendothelial system and expelled after several weeks, while very small nanomaterials have short-term retention and are excreted after hours or days. It is though noteworthy that nanomaterials dimension is not the only factor influencing the fastness of clearance from human body. Also, their surface charge [7] impact the protein adsorption on the nanomaterials surface, which can determine an efficient cellular uptake but also the recognition from macrophages and immune system cells, which leads to nanomaterials expulsion. Since positively charged nanomaterials can interact electrostatically with the negatively charged surface of cellular membranes, their uptake *in vitro* is higher than neutral of negatively charged analogues. On the other hand, negative nanomaterials exhibit higher blood half-life in vivo than positive ones which, on the contrary, are cleared faster and can cause complications as haemolysis. This phenomenon is caused by the fact that positive nanoparticles are more easily affected by non-specific serum protein absorption on their surface, such as immunoglobulins or albumin. This coating results in changes in their hydrodynamic size and surface charge, and indices a faster recognition of these nanomaterials by the mononuclear phagocyte system (MPS) for the subsequent clearance through the liver and spleen.

Taking nanoparticles as case study, to decrease undesired coating on their surface, one of the most used strategy is to cover them with poly-ethylene glycol (PEG) [8] which drastically increases the blood half-life of nanomaterials.

Perrault et al. systematically studied blood half-life in vivo of PEGylated Gold nanoparticles. They synthesised Au nanoparticles with hydrodynamic diameter in the 20-100 nm range, coated with PEG chains of different lengths on their surface. The study showed that longer half-life could be reached for smaller nanoparticles and longer PEG chains, with an improvement of the half-life of 12 times for 17 nm nanoparticles covered with 10 KDa PEG compared to those having the same hydrodynamic radius but covered with 2 KDa PEG [9].

Moreover, the great versatility of nanomaterials is the result of the possibility to chemically modify their surface *via* a number of methods. Indeed, with well-known and easy to perform techniques of bioconjugation polypeptides, antibody, oligonucleotides, growth factor or even small molecules such as folate have been linked to nanomaterials [10]. These techniques allow to tune nanomaterials blood half-life and efficacy, but they also permit the creation of materials suitable for active targeting and thus providing high sensitivity and specificity in vivo.

As a matter of fact, active targeting is another strategy to selectively accumulate nanomaterials in ill tissues and it is based on an active interaction between receptors on cells surfaces on tissues and a nanomaterial. To achieve this, two features are crucial: the first one is the overexpression of targeted receptors on ill cells compared to healthy tissues cells and the second one is the specificity of the targeting agents used.

In this case, the already cited technique of bioconjugation is used to define the possibility to link active biomolecules to nanomaterials for targeting purposes and this can be achieved via several strategies, that is chemical conjugation of molecules to nanomaterials, by exploiting electrostatic interactions or by exploiting other non-covalent interactions. An example of the last strategy is the well-known interaction between biotin and avidin. Avidin is a globular glycoprotein composed of four subunits able to interact with biotin [11]. Despite biotin-avidin system is not assembled by a covalent bond, once this interaction is formed (under the right conditions of pH, ionic strength and temperature) it is highly specific ($K_a = 10^{15}\ M^{-1}$) and it is resistant to high temperatures. Because of the extremely specificity of this interaction, nanomaterials functionalised with avidin (or streptavidin) are widely used for a number of applications for active targeting *in vivo* but also for sensing purposes, as the microparticles-based sensing devices for glucose detection developed by Kondo [12].

1.2 Biosensors

Biosensors are analytical devices that convert a biological response into a measurable signal. Firstly developed in the Sixties by the pioneers Clark and Lyons [13], nowadays biosensors are widely used in several fields, as food industry and medicine. Features for an efficient biosensor are good stability, good sensitivity in the desired concentration range, high selectivity for the analyte in the working conditions, and low limits of detection (LOD).

A typical biosensor is usually made of an assembly of a biological recognition element, which can interact with the analyte of interest and a transducer that converts the biochemical interaction into a measurable signal.

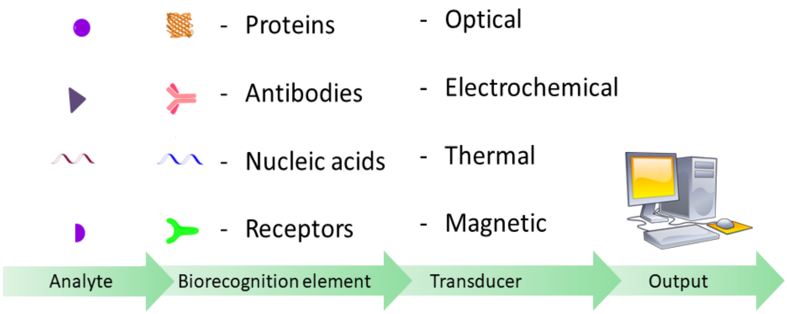

Figure 1: General scheme of a sensor. Readapted image from [14].

Biosensors can thus be divided according to the type of signal that is measured or taking into account the kind of biochemical process/biomolecules involved in the recognition part.

For example, amongst the plethora of biosensors we can name optical, magnetic, electrochemical or thermal biosensors, but for the purpose of this thesis we will focus on optical biosensors.

1.2.1 Optical biosensors

An optical biosensor is a device containing a sensing element connected with an optical transducer and it is able to generate a signal which is related to the concentration of the target analyte. Optical biosensors are probably the most common developed type of sensors, thanks to their great advantages as the high specificity, sensitivity and cost effectiveness combined to the possibility to perform direct and fast detection of analytes in several fields.

Optical sensors can work in a label-free or label mediated manner. The signal in label-free biosensors is generated by the interaction between the analyte and the transducer, as in SPR (Surface Plasmon Resonance)[15], ellipsometric biosensors, optical fibres and so on.

In contrast, the label mediated biosensors are based on a recognition event between the analyte and the labelling element and then the signal is generated by colorimetric or luminescent methods.

Focusing on label-based optical biosensors, for an optimal design of the device, it is equally important to define the right recognition element and a suitable method of transduction of the bio-recognition event. While the types of recognition elements will be discussed in the next section (nanomaterials for biosensing applications), here we will present the most common mechanisms employed in optical biosensors.

As aforementioned, the optical properties that can be exploited are photo-luminescence (both fluorescence and phosphorescence), (electro)chemi-luminescence, thermo-luminescence, absorbance, and reflection. So far, the most common optical biosensors are the fluorescence-based ones, which exploit the evaluation of fluorescence-related optical properties like emission intensity, lifetime, anisotropy, quenching efficiency through energy, electron, or proton transfer processes,, the formation of emitting excimers or exciplexes.

The advantages of the fluorescence-based biosensors rely on their sensitivity, cost effectiveness, simplicity and versatility.

Since the detection is measured through the variation of properties of a fluorophore upon local interactions with the analyte itself in the environment of detection, parameters that must be taken into account during the design of optical biosensors are the chemical and photochemical stability (as the susceptibility to photo-bleaching) of the probe in the environment, its pH dependency, self-quenching at high concentrations, self-absorption effects due to small stokes-shift of some organic dyes.

The dyes used during this work are mainly organic dyes and transition metal complexes.

Organic dyes are usually composed of functional groups with and extended conjugated π-system. By tuning the extension of the π-system, organic compounds absorbing photons in the ultraviolet, the visible and near infra-red range of the electromagnetic spectrum can be synthesised. The absorption of radiation leads to a variation in the electronic configuration of the dye and to an increase of its energy, to populate one of the excited states, according to selection rules [16]. New excited species quickly relaxes on the lower excited state having the same spin multiplicity (internal conversion) and it then decays to the fundamental state either via a radiative path, thus generating fluorescence or via a non-radiative one, releasing heat during the process.

Transition metal complexes are based on a transition metal coordinating organic ligands. The photochemical properties of these structures are based on three different types of excited states: d-d excited states involving the excitation of electrons on d orbitals of the metal (MC = metal centred); excited states obtained by the promotion of an electron from filled to unfilled orbitals on the ligands (LC = ligand centred); charge transfer excited states characterised by the shift of electron density from the metal to the ligand (MLCT = metal to ligand charge transfer) or from ligand to metal (LMCT). Given these premises, the emission properties of metal complexes can be easily tuned by synthesising different ligands. For the d^6 metals, as we are going to see in chapter 5, because of spin-orbit coupling, the singlet excited state easily goes through intersystem crossing and thus it converts to lowest energy triplet , which decays to the ground state exhibiting a phosphorescence emission, associated with long lifetimes (usually in the range of sub microseconds). Moreover, due to the large stokes-shift, metal complexes hardly suffer from self-absorption and self-quenching, but on the other side they are usually subjected to oxygen quenching due to their aforementioned long lifetimes.[17]

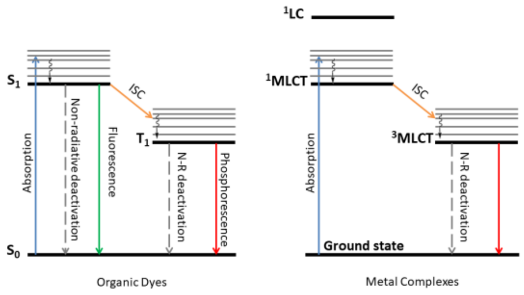

Figure 2: Comparison of Jablonski diagrams of organic dyes (left) and d^6 metal complexes (right).

So far, there is a wide literature both on organic dyes and on metal complexes as optical probes, due to the different properties that can be exploited. In the first case, the intense fluorescence emission and colour tunability; in the second case, the long living excited states generating phosphorescence.

On the other side, every new probe must be analysed in terms of stability in the environment of application and this is especially true for bioimaging probes. Hydrophobicity must be evaluated, but also histological tests and measurement of IC50 (half maximal inhibitory concentration) needs to be performed to obtain a functional probe. Despite all these parameters can be tuned by changing the functional groups of organic dyes or the ligands in metal complexes, sometimes coupling these optical probes with nanomaterials can also be a winning strategy [18].

1.3 Nanomaterials for bio-sensing applications

In particular, nanomaterials have been furnishing key instruments for easy engineering and fine-tuning unprecedent biosensing configurations based on recognition phenomena occurring at the nanoscale.

As already stated in section 1.1, nanomaterials are characterised by several properties which have been exploited to create more performing biosensors in terms of affinity of the signalling part and amplification of signal, since the dimensions of nanomaterials are comparable with the size of biomolecules.

In fact, nanomaterials can be used to fabricate nanowires, nanoparticles, micro cantilever, carbon nanotubes, which are able to amplify the signal thanks to their new optical, magnetic or electrical properties compared to sensors of the previous generation.

Furthermore, using nanomaterials can also improve the efficiency of the binding event in the signalling part of the device and this can be obtained by exploiting the natural affinity of some natural nanomaterials as enzyme-substrate, antibody-antigen, complementary DNA strands.

Having said that the recognition element can be any type of biological system, it must be taken into account that the choice of this part will strongly influence the device durability, sensitivity and application.

For example, several microbes have been used as sensing element instead of proteins or antibodies due to the easiness of production via cell culture, stability and ability to adapt to the targeted substrate. Despite these advantages, their major drawback is the lack of selectivity, due to their non-specific metabolism. This is the reason why new generation microbial sensors are those selectively engineered or those obtained in selective cell culture conditions able to induce the amplification of microbes having a specific metabolic pathway [19]. Amongst the several possible biorecognition elements, we will discuss DNA-based biosensors:

1.3.1 DNA: a target and a probe

1.3.1.1 Structure and properties

Deoxyribonucleic acid (DNA) belongs to the class of nucleic acid macromolecules which is present in all living cells and it is involved in the storage, encoding and expression of genetic information.

As firstly published in 1953 [20], DNA is a polymer constituted of two antiparallel polynucleotide strands. Each nucleotide is composed of a five-carbon sugar (2-deoxyribose) binding one or more phosphate groups and a nitrogen-containing base.

The nitrogen bases are divided into two classes, which differ from each other for their dimensions:

- Purines are constituted by a five-atom and a six-atom rings fused together and, in the case of DNA, they are Guanine (G) and Adenine (A);
- Pyrimidines consist of a six-atom ring and in DNA they are cytosine (C) and Thymine (T).

Each strand of DNA is thus composed of a sequence of nucleotides held together via a phosphodiester linkage between the 3’ and 5’ carbons of two consecutive sugars.

The 3D structure of the DNA arises instead from the hydrogen bounds between two strands. The way in which two strands of DNA are linked together relies on the pairing of a purine base with a pyrimidine on the basis of the number of hydrogen bonds they can form; i.e. adenine can bind thymine via 2 hydrogen bonds and guanine can bind cytosine via 3 hydrogen bonds.

DNA thus results in being an amphiphilic double helix composed of hydrophobic nitrogen-bases and hydrophilic phosphate sugar backbone, exposed to the aqueous environment of cells.

The structure as firstly described by Watson and Crick is known as B-DNA, a right-handed double helix composed by 10 nucleotides per turn lying perpendicular to the helix axes, with a 34 Å helix pitch. This form has a major groove of 10.7 Å and a minor one of 8.5 Å. This structure is stable in relatively humid conditions.

This is not the only polymorph of DNA today known. Below the most common polymorphs are described.

A-DNA is a right-handed helix with 11 nucleotides per turn tilted respect to the helix axes and it is favoured upon dehydration and low electrostatic repulsion.

C-DNA, right-handed helix with an average 9.3 residues per turn and it was first observed in Lithium salt of calf thymus DNA.

D-DNA, right-handed helix with an average 8 residues per turn and it is found in sodium salts of poly[d(A-T)]-poly[d(A-T)]as well as poly[d(A-A-T)]-poly[d(A-T-T)] sequences.

E-DNA, right-handed double helix with 15 residues per turn and a tilted angle of 48° from the helix axes.

All these double helix conformations are stabilized under different conditions of humidity, pH, temperature and cations concentration, and they possess different electrostatic potential, steric effect and hydration.

Z-DNA is instead a left-handed double helix consisting of sequences of cytosine and guanine, found at high salt concentration. It has 6 nucleotides per turn and a characteristic *zig-zag* backbone due to the alternate syn/anti conformations of the glycosyl bond.

Moreover, higher degree DNA structures have also been identified.

It’s noteworthy to mention the H-DNA, an intramolecular triple helix structure, stabilized by low pH values. In this condition, the pyrimidine-rich strand partially fold back parallel to its complementary strand creating a region of double helix (Watson-Crick pairing) and a so called Hoogsteen pairing.

i-motif DNA are second DNA structure stabilised upon acidic pH conditions for C-rich sequences. The hemi protonated C-CH$^+$ stabilized upon acidic pH conditions leads to two parallel DNA stretches to be held together. For this conformation to occur, four C-rich strands are thus needed and a pH ranging between 3 and 7.

G-DNA are a family of quadruplexes found in G-rich sequences, forming Hoogsteen type hydrogen bonds pairs among guanynes.

Many other polymorph have been described in a number of papers and reviews [21], [22].

1.3.1.2. Hybrid DNA

While studying the mechanisms whereby DNA could transfer the genetic information to other molecular species, in 1960 A. Rich succeeded to create for the first time a hybrid double helix, by annealing a synthetic DNA strand and a synthetic RNA strand [23].

Nowadays is well known that RNA:DNA hybrids are involved in DNA replication, regulation of gene expression and cell-specific processes.

RNA:DNA hybrids are in fact formed in living organisms during intermediate steps for the formation of double strands DNA or RNA. These transient intermediate (usually short sequences of 18-22 base pairs) are then removed at the end of the replication steps by RNase H, an enzyme belonging to the nuclease family which specifically degrade the RNA fraction in hybrids [24].

In the same way, one of the steps of RNA genesis is the formation of coupled RNA strand with a DNA template. The normal process brings to the separation of the two strands and the covering of the RNA strand by RNA biogenesis factors in order to prevent further interactions with DNA template. Nonetheless, some circumstances may lead to the formation of the so called R-loop structures, three-stranded nucleic acid structure, composed of a DNA:RNA hybrid and the associated non-template single-stranded DNA. R-loop prevents DNA methylation thus stimulating gene expression [25].

On the other side, the creation and accumulation of hybrids out of their natural context can lead to a DNA damage. Although the mechanism through hybrids damage DNA is still poorly understood, it seems that they can interfere with DNA replication and double strand DNA breaks (DSB) repair.

Increasing literature shows a relationship between RNA:DNA hybrid accumulation and human diseases. An example is the Senataxin helicase (SETX): this is an enzyme with hybrid-resolving activity by translocating RNA or DNA strand in hybrids. The prevalent R-loops accumulation in GC rich termination sites is involved in an efficient transcription termination and SETX is the gene that codify the enzyme Helicase Senataxin that later disassemble R-loop hybrid to allow the release of newly generated RNA.

Mutations in SETX can lead both to loss or gain of the enzyme activity and both the mutations lead to an impairment of R-loop homeostasis, linked to human diseases.

In particular, is now well studied the implication of SETX dysfunction in neurodegenerative disorders. Is seems indeed that a Senataxin loss of function is associated with Ataxia with oculomotor apraxia type 2 (AOA2), while SETX gain of function is linked to Amyotrophic later sclerosis type 4 (ALS4) [26]. In the first case, the SETX enzyme loss of function lead to an inefficient R-loops removal, which seems to be the cause of DNA damage and transcription defects found in fibroblast from AOA2 patients. In the second case, although studies are still ongoing, it seems that in cells from ALS4 patients a missense mutation L389S in Senataxin is found: an overexpression of the muted protein results in an extreme efficiency in R-loop dismantle at GC rich promoters of some genes, with a consequent damage in R-loop homeostasis.

Senataxin is also involved in the cellular response to RNA viruses, as HIV-1 or influenza A. it has been proved that SETX-silenced cells show a hyper-activation of immune response, bringing to an excessive inflammation state.

Moreover, some forms of cancer cells show the SETX gene mutated. Also, BRCA1 and BRCA2 are tumour suppressor factors, regulating the BRCA pathway: they prevent R-loop accumulation and mediate the recruitment of Senataxin to R-loop. R-loop removal by SETX-BRCA1 prevents DNA damage and it is one of the evidences that R-loop are involved in oncological progression [26].

In conclusion, the transient formation of RNA:DNA hybrid seems to be physiological for DSB repair. On the other hand, the formation of hybrid out of their place or the impairment of R-loop homeostasis reveals to be potentially harmful for human. Thus, hybrid and R-loop quantification methods can be very important for early detection of diseases.

1.3.1.3. DNA-based BIOSENSORS

The importance of the detection of DNA is so well established that several biosensors have been designed to develop sensing devices to detect DNA at ever lower concentrations.

It is equally known that sensing applications can benefit from the application of nanomaterials. Combining these two concepts, an emerging idea have been developed in the last decades, that is the recognition that DNA is a nanomaterial itself, able to self-assemble into several nanostructures. That’s why DNA is recently found to be very useful for the reorganization of materials, for the carriage of information and for sensing applications.

DNA is indeed widely used as biological recognition element in a type of DNA-based biosensors, which exploit the very selective interaction of a single strand DNA with its complementary strand, due to the formation of H-bonds.

Amongst the plethora of sensing devices involving DNA as detection part [27], a widespread tool are the molecular beacons (MBs): they are engineered single stranded nucleic acid probes composed of three parts: stem, a loop, and a quencher-fluorophore pair. Several devices based on molecular beacons have been developed and they are ideally based on at least 4-5 bases in the stem part and 15 in the loop part, having fluorophores or fluorophore/quencher respectively at the 5’ and 3’ ends.

The nucleotides on the loop region are complementary to the target ssDNA strand (they are formerly the detection element), so that when the target is present in solution, the hybridization between the two strands drives the changing of conformation of the MB, with a subsequent switch on of the fluorophore. The same strategy can be used coupling the MB ends with a pair of fluorophores acting respectively as donor-acceptor, in order to register a decrease in FRET (Forster Resonance Energy Transfer) efficiency.

Molecular beacons became versatile tools for real-time monitoring of hybridization of genetically-modified organisms [28], single nucleotide polymorphism and DNA mutations [29], and even for molecules not containing DNA sequences, as proteins and small molecules [30].

1.4 Hyaluronic acid

Hyaluronic acid is a polysaccharide polymer whose repetitive unit is a disaccharide composed of N-acetyl-D-glucosamine and D-glucuronic acid, linked by β(1-3) and β(1-4) glycosidic bonds. Hyaluronic acid (HA) is naturally available in cartilage and mammalian connective tissues. Moreover, in extracellular matrixes as synovial and rheumatoid fluids, HA acts as booster of their rheological properties.

Hyaluronan molecular weight can range from less than 10 to 10^4 KDa. Its high mass is responsible for the steric hinderance of hyaluronan networks, which causes the polymer ability to slow down the diffusion of solvents and molecules into the network itself. *In vivo* Hyaluronan regulates the transport of molecules through intercellular spaces, also acting as diffusion barrier.

Moreover, is well known that HA can interact with proteins and also with some neutral saccharides, as reported for the first time by Fraser *et al.* in 1972 [31].

The discovery of Hyaluronan interaction with cells membranes dates back to the Seventies as well. Hyaluronic acid interacts mostly with the transmembrane receptor cluster determinant 44 (CD44) and receptor for hyaluronate-mediated motility (RHAMM). In particular, for the CD44 receptors, the interactions involved include hydrophobic interactions between N-acetyl group and tyrosine and isoleucine groups, hydrogen bonds between HA carboxylate group and tyrosine and arginine of CD44, hydrogen bonding between C-6 hydroxyl group of HA and tyrosine, and between vicinal diols of HA and guanidine groups of arginine in CD44 [32].

With this knowledge, hyaluronic acid has been used into several applications, as in the synthesis of Hyaluronic acid based nanoparticles for therapeutic and sensing purposes [33], [34].

1.4.1 Hyaluronic acid interaction with nanomaterials

Hyaluronic acid have been recently proved to interact with the soft shell of silica nanoparticles [35].

Indeed, an efficient derivatization of hyaluronic acid with RITC (rhodamine isothyiocianate) was obtained exploiting the nucleophilic attack by the methyl-hydroxyl group of the polysaccharide to the reactive isothiocyanate groups. Despite the reaction was conducted in organic solvent, after a dialysis purification step, a non-turbid water solution of hyaluronic acid conjugated with rhodamine (HA@RB) was obtained.

When HA@RB is mixed with PLURONIC silica nanoparticles (PluSNPs) the photophysics of RB dyes in the HA@RB nanogels displays important variations, with a remarkable change of the absorption spectrum and the increase of fluorescence intensity.

Doping the PluSNPs with diethylamino coumarine dye (DEAC) according to a well-known protocol, luminescent nanoparticles were obtained (PluSNPs@DEAC) in order to monitor the energy transfer from PluSNPs to HA, where DEAC act as donor and RB as acceptor.

In both the cases, HA was proven to interact with nanoparticles: more specifically, the changes in the photophysical properties of rhodamine in the nanogel are due to a progressive disentanglement of the hyaluronic acid, which interacts with the PLURONIC surface of nanoparticles, thus offering a less polar environment to the rhodamine dyes.

The ability of hyaluronic acid to interact with cells and biological systems brought to the production of extensive literature on hyaluronic acid used as probe. This knowledge and the results just shown open up an ideal large amount of new application of hyaluronic acid-based probes In our laboratory, are currently under study the interactions between HA and nanomaterials of environmental and biological interest. Indeed, promising results have been achieving using HA@RB as a probe to detect micro-plastics and to obtain information on their dimensions in aqueous samples. Moreover, an interaction between hyaluronic acid and protein aggregates have been observed, allowing to monitor the kinetic of aggregation. Interestingly, the combined system PluSNPs and HA can not only detect the formation of protein aggregates but it can also actively interfere with the shape and dimensions of the latter.

These applications of hyaluronic acid derivatives thus highlight the versatility of this nanomaterial and they therefore piqued our interest toward the exploration of new luminescent hyaluronic acid derivatives to be used as chemosensor.

As part of chemosensor HA is therefore acting as sensing part of the device; the aim of large part of this work was then to investigate an efficient way to derivatize HA with a proper signalling part.

Since optical transduction is an easy and low cost approach, several dyes were investigated. Both organic dyes and metal complexes were investigated and used to functionalize HA.

The work presented in part B and C of this thesis lies on these proved interactions and it is focused on the synthesis of several functionalised HA nanogels for sensing purposes.

For an easier organization, the chapters 3 4 5 will focus on the functionalization of HA with a different dye. For each sample, a photophysical characterization will be provided and the HA@dye interaction with nanomaterials will be investigated.

1.5 References

[1] 'The European Commission Tries to Define Nanomaterials', *Ann. Occup. Hyg.*, Jan. 2011, doi: 10.1093/annhyg/meq092.

[2] S. H. Nile, V. Baskar, D. Selvaraj, A. Nile, J. Xiao, and G. Kai, 'Nanotechnologies in Food Science: Applications, Recent Trends, and Future Perspectives', *Nano-Micro Lett.*, vol. 12, no. 1, pp. 1–34, Jan. 2020, doi: 10.1007/s40820-020-0383-9.

[3] X. Y. Wong, A. Sena-Torralba, R. Álvarez-Diduk, K. Muthoosamy, and A. Merkoçi, 'Nanomaterials for Nanotheranostics: Tuning Their Properties According to Disease Needs', *ACS Nano*, vol. 14, no. 3, pp. 2585–2627, Mar. 2020, doi: 10.1021/acsnano.9b08133.

[4] L. Wang and W. Tan, 'Multicolor FRET Silica Nanoparticles by Single Wavelength Excitation', *Nano Lett.*, vol. 6, no. 1, pp. 84–88, Jan. 2006, doi: 10.1021/nl052105b.

[5] B. St, 'Marina A. Dobrovolskaia* and Scott E. McNeil', *Nat. Nanotechnol.*, vol. 2, p. 10, 2007.

[6] H. Kobayashi, R. Watanabe, and P. L. Choyke, 'Improving Conventional Enhanced Permeability and Retention (EPR) Effects; What Is the Appropriate Target?', *Theranostics*, vol. 4, no. 1, p. 81, 2014, doi: 10.7150/thno.7193.

[7] Y. He, J. Qin, S. Wu, H. Yang, H. Wen, and Y. Wang, 'Cancer cell–nanomaterial interface: role of geometry and surface charge of nanocomposites in the capture efficiency and cell viability', *Biomater. Sci.*, vol. 7, no. 7, pp. 2759–2768, 2019, doi: 10.1039/C9BM00037B.

[8] A. E. Nel *et al.*, 'Understanding biophysicochemical interactions at the nano–bio interface', *Nat. Mater.*, vol. 8, no. 7, pp. 543–557, Jul. 2009, doi: 10.1038/nmat2442.

[9] S. D. Perrault, C. Walkey, T. Jennings, H. C. Fischer, and W. C. W. Chan, 'Mediating Tumor Targeting Efficiency of Nanoparticles Through Design', *Nano Lett.*, vol. 9, no. 5, pp. 1909–1915, May 2009, doi: 10.1021/nl900031y.

[10] H. Jin *et al.*, 'Folate-Chitosan Nanoparticles Loaded with Ursolic Acid Confer Anti-Breast Cancer Activities in vitro and in vivo', *Sci. Rep.*, vol. 6, no. 1, p. 30782, Nov. 2016, doi: 10.1038/srep30782.

[11] 'N. Green, «Avidin,» Adv. Protein Chem. , vol. 29, pp. 85-133, 1975.'

[12] T. Matsumoto, T. Tanaka, and A. Kondo, 'Sortase A-Catalyzed Site-Specific Coimmobilization on Microparticles via Streptavidin', *Langmuir*, vol. 28, no. 7, pp. 3553–3557, Feb. 2012, doi: 10.1021/la2047933.

[13] 'Clark, L. C.; Lyons, C. Electrode systems for continuous monitoring in cardiovascular surgery. Annals of the New York Academy of Sciences 1962, 102(1), 29–&.'

[14] P. Damborský, J. Švitel, and J. Katrlík, 'Optical biosensors', *Essays Biochem.*, vol. 60, no. 1, pp. 91–100, Jun. 2016, doi: 10.1042/EBC20150010.

[15] P. Falkowski, Z. Lukaszewski, and E. Gorodkiewicz, 'Potential of surface plasmon resonance biosensors in cancer detection', Journal of Pharmaceutical and Biomedical Analysis, vol. 194, p. 113802, Feb. 2021, doi: 10.1016/j.jpba.2020.113802.

[16] K. R. A. S. Sandanayake and I. O. Sutherland, 'Organic dyes for optical sensors', *Sens. Actuators B Chem.*, vol. 11, no. 1–3, pp. 331–340, Mar. 1993, doi: 10.1016/0925-4005(93)85272-C.

[17] R. Zhang and J. Yuan, 'Responsive Metal Complex Probes for Time-Gated Luminescence Biosensing and Imaging', *Acc. Chem. Res.*, vol. 53, no. 7, pp. 1316–1329, Jul. 2020, doi: 10.1021/acs.accounts.0c00172.

[18] D. Svechkarev and A. M. Mohs, 'Organic Fluorescent Dye-based Nanomaterials: Advances in the Rational Design for Imaging and Sensing Applications', *Curr. Med. Chem.*, vol. 26, no. 21, pp. 4042–4064, Sep. 2019, doi: 10.2174/0929867325666180226111716.

[19] M. R. Charbonneau, V. M. Isabella, N. Li, and C. B. Kurtz, 'Developing a new class of engineered live bacterial therapeutics to treat human diseases', *Nat. Commun.*, vol. 11, no. 1, Art. no. 1, Apr. 2020, doi: 10.1038/s41467-020-15508-1.

[20] F. C. J.D. Watson, «Molecular structure of nucleic acid,» *Nature,* pp. 737-738, 1953.

[21] M. T. Record, S. J. Mazur, P. Melancon, J. H. Roe, S. L. Shaner, and L. Unger, ‘Double Helical DNA: Conformations, Physical Properties, and Interactions with Ligands’, *Annu. Rev. Biochem.*, vol. 50, no. 1, pp. 997–1024, Jun. 1981, doi: 10.1146/annurev.bi.50.070181.005025.

[22] D. Svozil, J. Kalina, M. Omelka, and B. Schneider, ‘DNA conformations and their sequence preferences’, *Nucleic Acids Res.*, vol. 36, no. 11, pp. 3690–3706, Jun. 2008, doi: 10.1093/nar/gkn260.

[23] M. Thomas, R. L. White, and R. W. Davis, ‘Hybridization of RNA to double-stranded DNA: formation of R-loops’, *Proc. Natl. Acad. Sci.*, vol. 73, no. 7, pp. 2294–2298, Jul. 1976, doi: 10.1073/pnas.73.7.2294.

[24] S. M. Cerritelli and R. J. Crouch, ‘Ribonuclease H: the enzymes in eukaryotes: Ribonucleases H of eukaryotes’, *FEBS J.*, vol. 276, no. 6, pp. 1494–1505, Mar. 2009, doi: 10.1111/j.1742-4658.2009.06908.x.

[25] C. Grunseich *et al.*, ‘Senataxin Mutation Reveals How R-Loops Promote Transcription by Blocking DNA Methylation at Gene Promoters’, *Mol. Cell*, vol. 69, no. 3, pp. 426-437.e7, Feb. 2018, doi: 10.1016/j.molcel.2017.12.030.

[26] ‘DNA/RNA Helicase Gene Mutations in a Form of Juvenile Amyotrophic Lateral Sclerosis (ALS4)’, *Am. J. Hum. Genet.*, vol. 74, no. 6, pp. 1128–1135, Jun. 2004, doi: 10.1086/421054.

[27] S. Ranallo, A. Porchetta, and F. Ricci, ‘DNA-Based Scaffolds for Sensing Applications’, *Anal. Chem.*, vol. 91, no. 1, pp. 44–59, Jan. 2019, doi: 10.1021/acs.analchem.8b05009.

[28] N. Dave and J. Liu, ‘Fast Molecular Beacon Hybridization in Organic Solvents with Improved Target Specificity’, *J. Phys. Chem. B*, vol. 114, no. 47, pp. 15694–15699, Dec. 2010, doi: 10.1021/jp106754k.

[29] M. Varona and J. L. Anderson, ‘Visual Detection of Single-Nucleotide Polymorphisms Using Molecular Beacon Loop-Mediated Isothermal Amplification with Centrifuge-Free DNA Extraction’, *Anal. Chem.*, vol. 91, no. 11, pp. 6991–6995, Jun. 2019, doi: 10.1021/acs.analchem.9b01762.

[30] A. Bertucci, J.Guo, N. Oppmann, A.Glab, F. Ricci, F. Caruso and F. Cavalier, ' Probing transcription factor binding activity and downstream gene silencing in living cells with a DNA nanoswitch', Nanoscale, 2018, 10, 2134

[31] J. R. Fraser, W. K. Foo, and J. S. Maritz, ‘Viscous interactions of hyaluronic acid with some proteins and neutral saccharides.’, *Ann. Rheum. Dis.*, vol. 31, no. 6, pp. 513–520, Nov. 1972, doi: 10.1136/ard.31.6.513.

[32] S. Banerji *et al.*, ‘Structures of the Cd44–hyaluronan complex provide insight into a fundamental carbohydrate-protein interaction’, *Nat. Struct. Mol. Biol.*, vol. 14, no. 3, pp. 234–239, Mar. 2007, doi: 10.1038/nsmb1201.

[33] K. Y. Choi *et al.*, ‘Self-assembled hyaluronic acid nanoparticles for active tumor targeting’, *Biomaterials*, vol. 31, no. 1, pp. 106–114, Jan. 2010, doi: 10.1016/j.biomaterials.2009.09.030.

[34] K. Y. Choi *et al.*, ‘Self-assembled hyaluronic acid nanoparticles as a potential drug carrier for cancer therapy: synthesis, characterization, and in vivo biodistribution’, *J. Mater. Chem.*, vol. 19, no. 24, p. 4102, 2009, doi: 10.1039/b900456d.

[35] F. Palomba *et al.*, ‘Specific, Surface-Driven, and High-Affinity Interactions of Fluorescent Hyaluronan with PEGylated Nanomaterials’, *ACS Appl. Mater. Interfaces*, vol. 12, no. 6, pp. 6806–6813, Feb. 2020, doi: 10.1021/acsami.9b17974.

PART A

DNA as a probe in biological environment

Chapter 2 –

DNA-based probe for NF-κB protein detection in living cells

2.1 introduction

NF- κB is a master transcription factor able to activate the expressions of some target genes related to stress response upon the interaction with a consensus DNA sequence.

NF-κB is a family of protein purified in 1986 by D. Baltimore, who also discovered their specific binding with DNA sequence 5’-GGGACTTTCC-3’ found in the enhancer of the immunoglobulin κ light chain gene in mature antibody-producing B cells [1].

This family of proteins is present in cytoplasm in its inactive form, non-covalently associated with IκB inhibitor. Upon several stimuli, the IκB kinase (IKK) promotes the inhibitor proteolysis, thus generating the NF-κB active form which accumulates in the nuclei. The combined action of IκB, NF-κB and IKK constitutes the NF-κB signalling module [2].

The NF-κB family is composed of five different polypeptides encoded by the human genome, having in common a region of amminoacids (known as Rel homology region or shortly RHR) and they are divided into two classes. Class I NF-κB proteins are p50 and p52; class II is constituted of p65 (also known as RelA, RelB, c-Rel).

The five RHR region of these polypeptides can form homo- or heterodimers, spaced by a sequence of 10 amino acids and in this configuration they form the NF-κB active form, able to bind the consensus DNA sequence.

Transcription factors (TF) are proved to be involved in gene regulatory leading to several disorders, inflammatory processes and cancer progression [3], that's why their detection could boost our knowledge of TF in healthy or ill cells, becoming a useful tool for diagnostics.

Thus, as the DNA consensus sequence recognized by NF-κB protein is known, a nanodevice exploiting this interaction can be used as detecting tool for NF-κB dimers *in vivo*.

Indeed, as stated in the introduction chapter (section 1.3.1), it is now well established that DNA can be considered not only as a target to detect, but also as a probe able to exploit bio-recognition thanks to its high specific interactions.

In this chapter. a synthetic DNA hairpin is used to detect the presence of NF-kB protein in solution and in living cells. Hairpin DNA probes (HDPs) are versatile tools in the field of bio-sensing both in homogeneous systems [4] and in solid state devices [5].

HDPs are single strand DNA assuming a stem-loop structure because of the presence of regions at the ends complementary to each other. In aqueous sensing systems hairpins are functionalised with two dyes (acting as donor-acceptor) or with a couple fluorophore-quencher able to interact only when in close proximity; thus, since the analyte concentration triggers different conformation of the hairpins, it correlates with the difference in signal observed (presence of energy transfer or quenching efficiency).

In this chapter we used a triplex-containing hairpin (Figure 2.1) designed by the research group at University of Melbourne that is constituted by a single stranded DNA with a 10 bases sequence (NF-κB consensus sequence), a 4 length bases loop, 10 bases complementary to the first sequence and a nine bases long tail having the last 4 bases complementary with the first 4 bases of the strand. Two thymine are conjugated with two commercial dyes QUASAR570 (T6) and QUASAR670 (T33). The hairpin can thus ideally switch between two conformations: state 1 (binding/Low-FRET- state) and state 2 (High-FRET state).

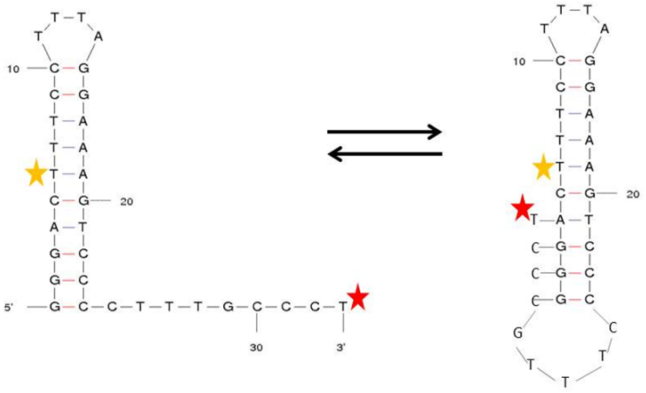

State 1

State 2

Figure 2.1 The equilibrium of Low-FRET double helix and a High-FRET giving triplex

2.2 Materials and methods

HPLC-purified oligonucleotide DNA sequences of Triplex-hairpinNF-κB, 5’-GGGACT(Quasar570)TTCCTTTAGGAAAGTCCCCTTTGCCCT(Quasar670)-3’ (the binding domain is underlined, the tail is double underlined) was supplied by Biosearch Technologies (Novato, CA, USA). Human recombinant NF-κB p50 was purchased from Cayman Chemical (Ann Arbor, MI, USA). Lipofectamine® RNAiMAX transfection reagent, DNase I, DNase I buffer, and 100× Halt™ protease inhibitor cocktail were obtained from Life Thermo Fischer Scientific (Waltham, MA, USA). PC3 human prostate epithelial cancer cell (CRL-1435) were purchased from ATCC®. Dulbecco’s phosphate-buffered saline (D-PBS) and bovine serum albumin (BSA) were supplied by Sigma-Aldrich (St Louis, MO, USA). Opti-MEM reduced serum medium and was obtained from Life Technologies (Scoresby, Australia). Trypsin and Dulbecco’s Modified Eagle’s medium (DMEM) were purchased from

Lonza (Allendale, USA). Fetal bovine serum (FBS) was supplied by Bovogen (Keilor East, Australia). All chemicals were used without further purification.

Fluorescent measurements

Steady-state fluorescence emission spectra were acquired on a Horiba FL-322 Fluorolog-3 spectrofluorometer equipped with a 450 W Xenon arc lamp as excitation source. The excitation wavelength λ_{ex} was set to 520 nm (exc. slit = 5 nm) and the range of acquisition was set from $\lambda = 550$ nm to $\lambda = 720$ nm (em. slit = 5 nm). A fluorescence quartz cuvette with a volume of 200 µL was used. All measurements were carried out at 25 °C or 37 °C. The solutions were annealed at 95°C for 5 minutes and let cool down to room temperature for 1 hour before the measurements. The concentration of the hairpin-triplex was 5 nM for all the experiments. Fluorescence emission spectra of hairpin-Triplex relevant to the binding curve for NF-κB were obtained by incubating for 2 minutes the probe with progressive concentrations of stock NF-κB p50/p50 dimer in the range of 0.1–500 nM.

Cell culture

Human prostate cancer PC3 cells were cultured in Dulbecco's Modified Eagle Medium (Lonza, Basel, Switzerland) supplemented with 10% fetal bovine serum (FBS) at 37 °C and in 5% CO2. After reaching 80–90% confluency, cells were detached using an enzyme-free dissociation buffer (Gibco, Thermo Fisher) and re-seeded in the relevant culture dish.

DNA nanoswitch transfection and confocal laser scanning microscopy performed on live cells

After seeding 40000 cells per well in a labtek 8 well chambers, using DMEM medium, we changed the medium to OPTI-MEM and we transfected the hairpin-triplex using lipofectamine as per the transfection protocol provided by the supplier. After 2 hours of incubation at 37 °C and 5% CO_2 , we washed 3 times with PBS and replaced the medium with DMEM medium. We incubated the cells again and we then fixed them with paraformaldehyde (PFA) 40% at different times within 24 hours. We analysed different samples, so that the final concentration of the probes was ranging from 5 to 50 nM.

For live cells experiments, 40,000 PC3 cells per well were plated on 8 well Nunc™ Lab-Tek™ II chambered coverglass (Life Technologies, Scoresby, Australia) in DMEM medium supplemented with 10% FBS and allowed to adhere for 24 hours. The cells were washed with PBS 1X prior the replacement of the DMEM with OPTI-MEM medium. The samples were treated with solutions of hairpin-triplex at the final concentration of 10 nM plus lipofectamine RNAiMAX. After 2 hours of incubation, the cells were washed three times with PBS 1X and the medium replaced. After two additional hours, DMEM medium was replaced by Leibovitz's medium supplemented with 10% of FBS and the samples were analysed using a Nikon A1R laser scanning microscope, at the excitation wavelength of 546 nm and 640 nm.

2.3 Results and discussion

Hairpin-triplex pH stability

Triplex structures can form in a parallel or antiparallel way. Indeed, pyrimidine-rich oligomers bind double-strand DNA in a parallel orientation, thus forming T-AT or C^+-GC Hoogsteen pairing. On the other hand, purine-rich oligonucleotides recognise dsDNA in an antiparallel orientation, leading to the couple A-AT or G-GC (Reverse Hoogsteen pairing). Since the triplex formation implies the assembly of three polyanion strands, causing an increased negative charge density, the stability of triplexes is improved by the presence of positive charges, as acidic pH, cations in solution, polyamines or other ligands. Also, the strand lengths and sequences can affect duplex and triplex stabilities. In fact, at low pH a Hoogsteen pairing C^+-GC are more stable than T-AT, because of the protonation of the N_3 position of cytosine. [6]
In 2013 Back et al. demonstrated that the charge of ions and their radius influence in different ways the stabilities of poly(T)-poly(A)poly(T) triplexes. In fact, they found out that divalent cations and especially Mg^{2+} stabilize both Watson-Creek and Hoogsteen pairing, at micromolar concentration, in a more efficient way compared to the millimolar concentration required for monovalent ions. In this study they

exploited melting temperature measurements to evaluate triplex and duplex stabilities, starting from the general observation that a T_{m1} at lower values is found for triplex and $T_{m2} > T_{m1}$ is related to duplex melting process.

Interestingly, using 1 mM Mg^{2+} in a triplex solution also containing 1 mM Na^{+} led to measure T_{m1} and T_{m2} at very similar temperature values (around 74 °C and 78 °C) [7].

For these reason, fluorescence measurements on the hairpin-triplex probe were carried out at 25 °C in PBS buffers (137 nM NaCl, 10 nM $MgCl_2$) at different pH, from 4 to 8.

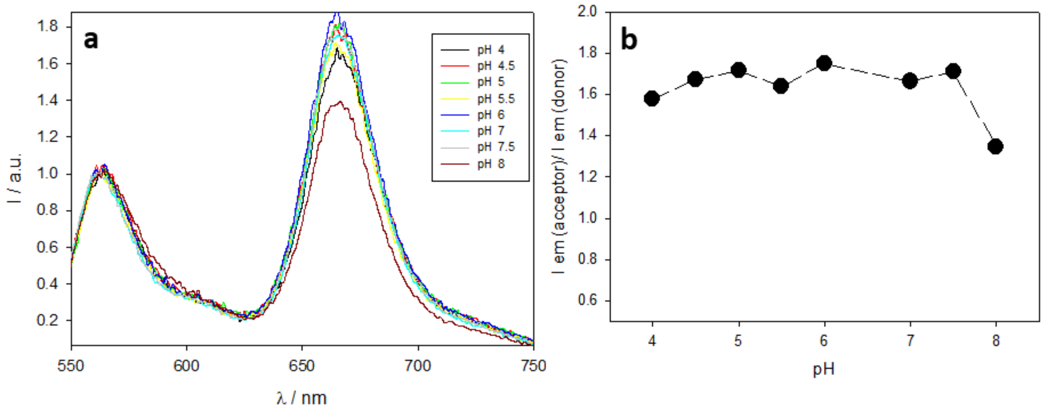

Figure 2.2: emission spectra of hairpin-triplex in PBS 1X + 10 mM $MgCl_2$ at 25 °C at pH from 4 to 8. λ_{exc} = 520 nm. Spectra normalised on the donor peak are shown (a); trends od Acceptor/Donor emission intensities ratio versus pH (b).

Fluorescence spectra shown in figure 2.2 demonstrate that in these ionic strength conditions a FRET phenomenon always occurs and that the probe is stable over a wide range of pH. This is probably due to the fact that the triplex is intramolecular, thus a proximity factor always promotes the formation of the short triple strand by Hoogsteen pairing.

Only at alkali pH (pH = 8) a lower A/D ratio is measured, indicating that a different conformation takes place.

Melting measurements were conducted to evaluate the stability of the probe over different pH. Fluorescence spectra of the hairpin-triplex in the suitable pH PBS buffer implemented with 10 mM $MgCl_2$ were registered at increasing temperature (from 20°C to 84°C, ΔT=2°C, λ_{exc} =520 nm, slit =5).

According to the literature, at high concentration of Na^+ and Mg^{2+}, both the duplex and the triplex result so highly stable that melting measurements failed to give us any result. This leads to the conclusion that the stability of the probe seems to be promising in an environment where positive ion concentration is in the mM range (and up to hundreds of mM for ion as K^+), like the cellular one.

Nonetheless, melting plots have been obtained after 1:100 dilution of the PBS + $MgCl_2$. In the graph in figure 2.3 the ratio of emission intensities of acceptor/donor versus temperature are reported.

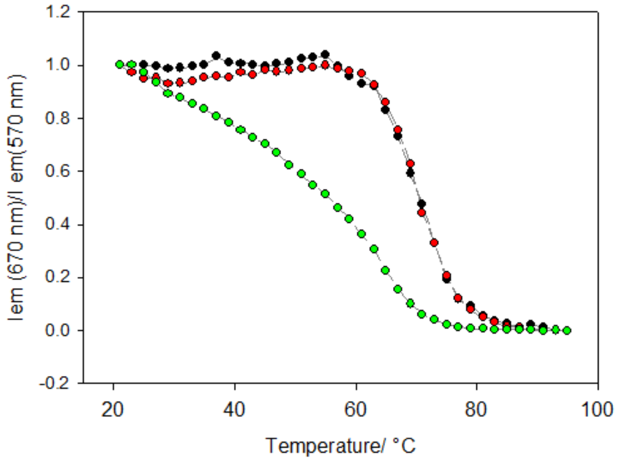

pH	T_m
4	70 °C
6	70 °C
8	57 °C

Figure 2.3 melting plot of hairpin-triplex at pH 4 (black dots), 6 (red dots) and 8 (green dots) in PBS implemented with 10 mM $MgCl_2$ diluted 1:100. Data are normalised in the range 0-1. (left); table of the melting temperatures obtained (right).

Through this technique we are able to evaluate the effect of the temperature on the probe by estimating the decrease of energy transfer as the temperature increases. As a matter of fact, we can see only one melting transition, and this is probably due to the fact that the ion concentration – 1.37 mM for Na^+ and 100 µM for Mg^{2+} – are values high enough, according to the literature, to see just one average value of melting temperature [8]. Both at very and slightly acidic pH values, a melting temperature of 70 °C is obtained, at the flex point of the sigmoidal curve obtained. At alkali pH a strong decrease of the T_m can be detected.

Stability test over DNAse action were conducted at 37°C. The stability of the probe over times at this temperature is demonstrated by the control sample within 250 minutes after the starting point. On the other hand, adding an excess of DNAse (10 μL of the commercial stock solution) induces a complete probe denaturation within 15 minutes.

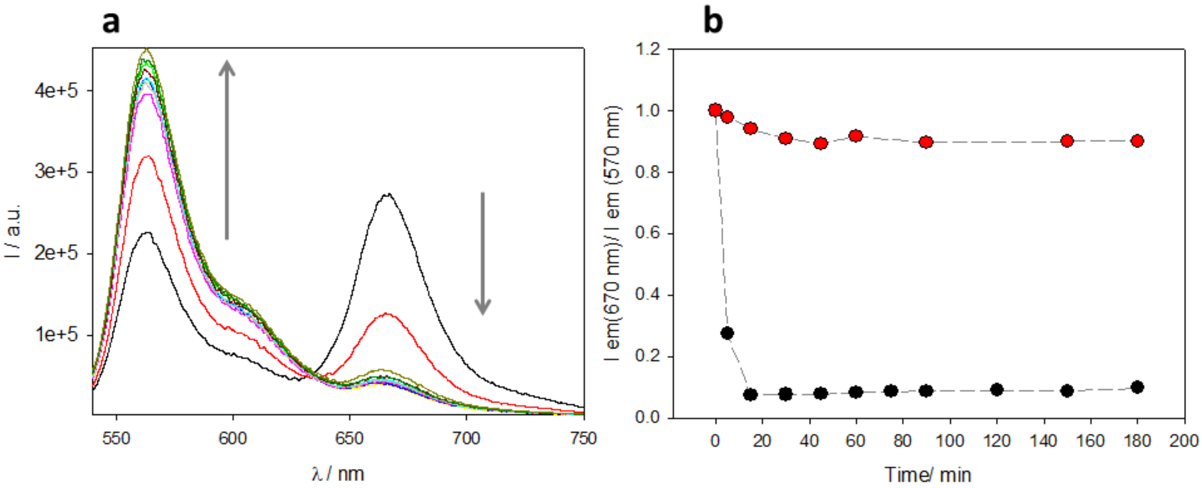

Figure 2. 4 Emission spectra of 5 nM hairpin-triplex over time during DNAse degradation (a); graph of A/D ratio vs time at 37°C in PBS pH 7.4, with DNAse (red) and without (black) (b).

In Table 2.1 the A/D ratios over time for the two samples are reported. Moreover, the FRET efficiency at 37°C is calculated, using the following formula

$$FRET\ [\%] = \frac{I_{max} - I_{DA}}{I_{max}} \times\ 100\ \% \qquad \text{eq. 2.1}$$

Where I_{max} is the intensity emission of the donor at the end of the DNAse digestion and I_{DA} is the intensity of the donor for each point.

Table 2.1 acceptor/donor ratios for the probe in PBS pH 7.4 + 10 mM $MgCl_2$ with and without DNAse and FRET% for the sample with DNAse.

Time (minutes)	A/D Intensity emission of control	A/D Intensity emission during DNAse	FRET% after DNAse
0	1.33	1.35	54
5	1.30	0.37	17
15	1.25	0.10	3
30	1.21	0.10	9
45	1.19	0.10	8
60	1.22	0.11	13
90	1.20	0.11	10

150	1.28	0.12	2
180	1.33	0.13	0

Using this strategy, an initial FRET of 54% (see eq. 2.1) is demonstrated to take place, due to the presence of a triplex conformation. Moreover, for the free strand in solution the signal of the donor emission is doubled after complete DNAse action while the acceptor emission becomes 1/5th of the initial value. It is noteworthy that even after the action of enzyme, a signal from the acceptor can still be detected upon its sensitised emission. Because of the random action of DNAse, it seems there is a small fraction of segments still bound to each other, which keep the donor and acceptor in close proximity. Nonetheless, the ratio between A/D is 10 times lower. Since we demonstrated that at physiological conditions the triplex conformation takes place, we performed a fluorescence titration of the hairpin-triplex probe with increasing concentration of the NF-kB dimer p50-p50. Three independent measurements were conducted.

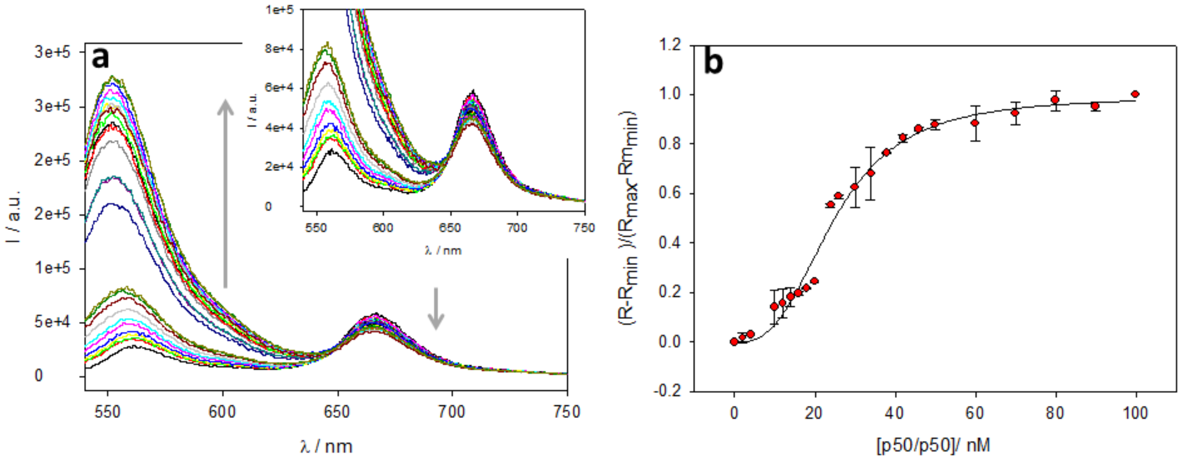

Figure 2.5: titration of 5 mM DNA probe with p50 dimer from 0 to 100 nM in PBS pH 7.4, insert: zoom in I_{em} in the range 0-100000 (a); quotient of donor/acceptor intensity emissions (R) (λ_{em} = 570 nm) normalised in the 0-1 range during titration (b).

The binding of the probe with the dimer leads to a progressive increase in the emission of the donor (around 8 times the initial emission), while the sensitized emission of the acceptor is subjected to a 1.3-fold decrease. In Figures 5b the fitting of the donor emission intensities vs p50 dimer concentration is shown. The best fitting was obtained through Hill model equation.

The Hill equation relates ligand concentration to the formation of ligand-receptor complexes for reversible and saturable equilibria and it can be derived from the mass action at equilibrium:

$$nL + R \rightleftarrows L_nR \qquad \text{Eq. 2.2}$$

Thus

$$[L_nR] = [R_0]\frac{[L]^n}{[L]^n + K_d^n} \qquad \text{Eq. 2.3}$$

Where L is the ligand, present at variable concentration, R the receptor, R_0 is the total concentration of the receptor, (supposing $[R_0] << [L]$ with the result of free ligands ≈ total ligands concentration), LR is the complex ligand-receptor. K_d is the ligand concentration at which half of the receptor is bound to the ligand and it is a measure of the affinity of the ligand to the receptor, since the smaller the value, the greater the affinity is. n is referred to as Hill coefficient it is an adimensional parameter reflecting the extension of cooperativity.

This lead to find the binding constant equal to 25±1 nM, using the Hill model with 3 parameters.

$$\mathrm{y} = \frac{y_{max}\mathrm{x}^{\mathrm{b}}}{\mathrm{x}^{\mathrm{b}} + \mathrm{K}^{\mathrm{b}}}$$

with y_{max} = 0.99

A factor b > 1 (2.85 in this experiment) indicates that a cooperative process takes place. It’s noteworthy that the curve obtained does not fit the usual ligand binding curve for one ligand-site receptor, although the receptor has one ligand-binding site (that is the NF-κB consensus sequence).

Having proved the time stability of the probe in the same condition of the experiment performed with p50/p50, the increasing of the donor emission signal and the decrease of the acceptor emission can be read as a proof of the interaction between the hairpin-triplex and the dimer.

Since the FRET in the hairpin-triplex arises from the Hoogsteen pairing of four base pair sequence, two forms (from now on called H-FRET for High FRET and L-FRET for Low FRET) are in equilibrium in physiological condition. The progressive interaction between the hairpin-triplex and the p50/p50 shifts the equilibrium toward the L-FRET state, having the consensus sequence more accessible to the protein.

STUDY ON CELLS

Analysis on live cells after transfection with the NF-κB-switch

Studies on live cells were conducted after the results on test tube showed in the previous section. NF-κB is supposed to be in in the cytosol in an inactive form, which goes into the nucleus in its activated state upon environmental stimuli. In PC3 cells the NF-κB is constitutively activated both in the nucleus and in the cytoplasm due to upregulation. Cells were transfected with NF-κB hairpin-triplex using lipofectamin as carrier, in order to form a positively charged lipophilic complex able to easily cross the cellular membrane.

After 2 hours of incubation of the cells with 10 nM of the NF-κB probe, the medium was replaced with fresh one in order to avoid the possible increase of fluorescence signals due to longer exposure time for different samples.

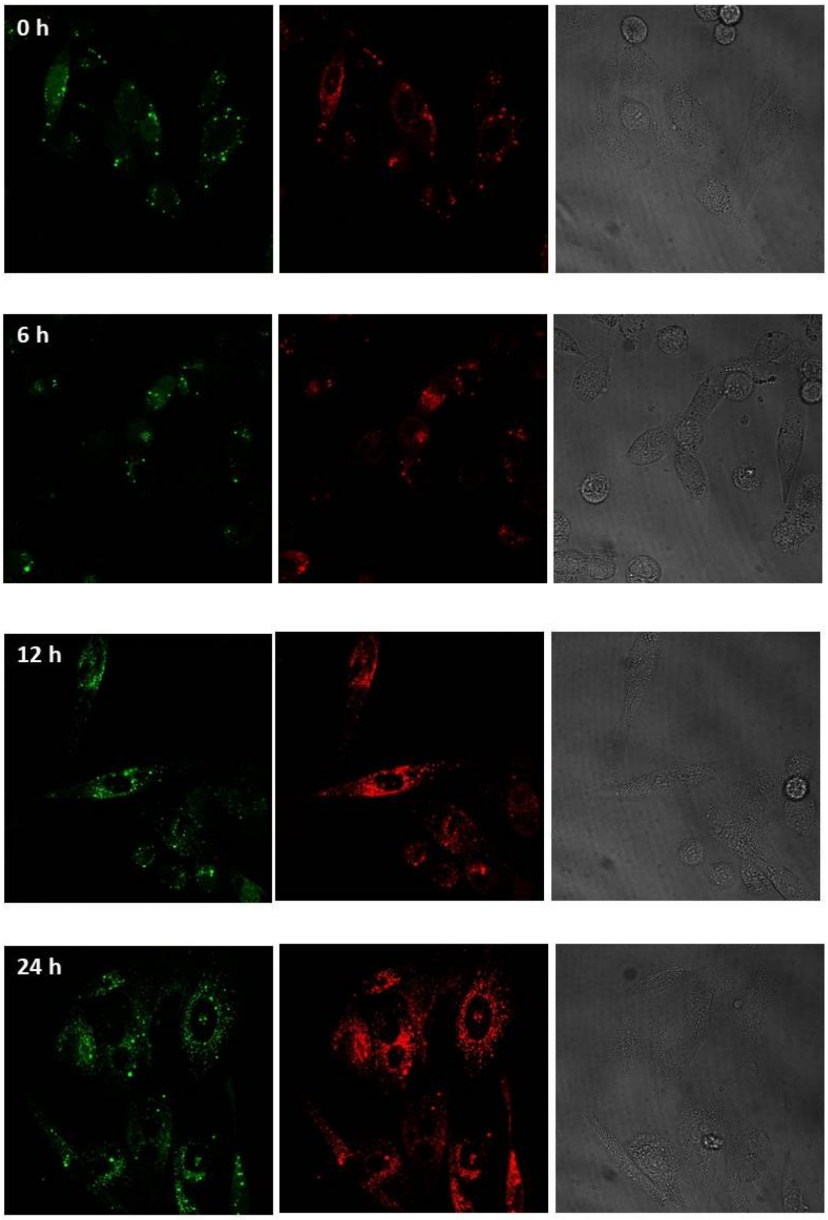

Figure 2.6 Confocal images 10 nM after 0, 6, 12, 24 hours since the end of the 2 hours transfection protocol. Excitation of the donor, excitation of the acceptor, bright field.

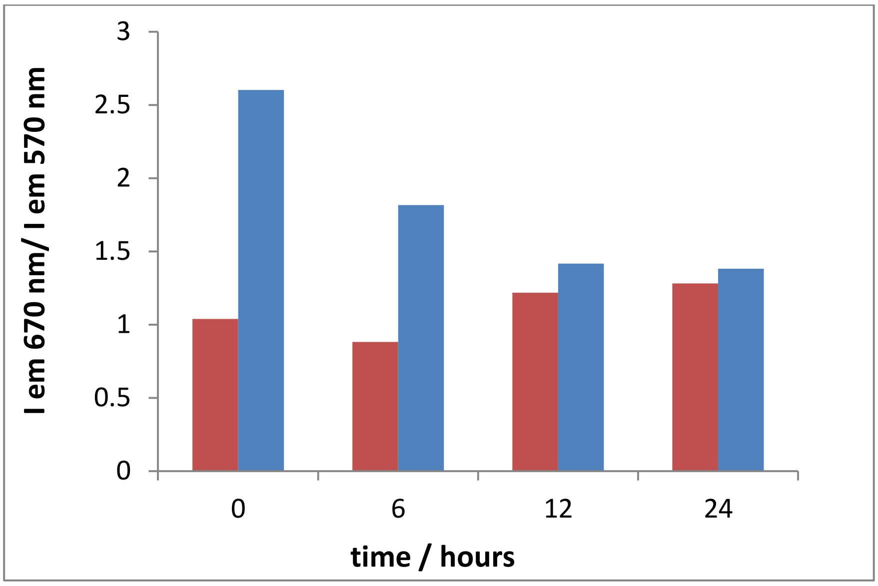

Figure 2.7: ratio of acceptor emission/donor emission in live cells over time for nuclear signal (red bars) and cytosolic signal (blue bars) in live PC3 cells. Laser exc = 561 nm.

Upon excitation of the donor, the ratio of the emission intensities of acceptor/donor was monitored over time. Each time, at least 30 cells were analysed. The average resulting signal in the cytosol after 2 hours of transfection is 2.6, consistent with a triplex conformation. Probably at the very first stage of the transfection it is still present a population of probe complexed with lipofectamine, thus constrained in a structure even more compact than the one normally measured in solution. Within 24 hours a progressive decrease of the ratio in cytoplasm up to 1.3 is observed. This value is consistent with the one measured in solution, where an equilibrium between L-FRET and H-FRET is observable. This result indicates that within the first 12 hours the probe can bind the active NF-κB protein in the cytosol.

Focusing on the signal coming from the nuclei, a lower ratio A/D is observed since the first stages and the value remains around 1 during all the time of the experiment.

It is interesting to note that after the first 6 hours a strongly decrease in the amount of fluorescent nuclei is observed (from 91% after 2h to 5% after 24 hours). The transient signal from the nuclei is consistent with what found in literature for other similar DNA-based probes [7]. It seems indeed that after NF-κB is quickly delivered to the nucleus, the binding of the protein to its target genes promotes the transcription of IκB protein, which shuttles back the NF-κB to cytosol, thus explaining the transient fluorescent signal of the probe in the nuclei.

On the other hand, in the nucleus the measured average ratio is higher compared to cytosol and a 20% increase is detected in the first 6 hours. After this point, a signal as high as in the cytosol is detected. It worthy to note that the percentage of fluorescent nuclei is progressively decreasing.

The colocalization of the two dyes was calculated using the EzColocalization plug in on ImageJ software, thus drawing ROI on both fluorescent nuclei and cytosols.

The perfect colocalization is identified by the Pearson correlation coefficients (PCC) value +1, while 0 means a non colocalization and a -1 identifies an anti-colocalization.

In all the cases a colocalization is seen (PCC > 0.5) as shown in the table below.

Table 4: Pearson correlation coefficients (PCC) for the hairpin triplex probe both in nucleus and cytosol.

Time (h)	**PCC**	
	Nucleus	**Cytosol**
0	0.68	0.56
6	0.47	0.68
12	0.67	0.75
24	0.86	0.81

The co-localization results prove that the signal detected in the nuclei arises from the simultaneous presence of both dyes. Thus, despite one could argue that the decrease of fluorescence in the nuclei could be due to DNAses degrading the DNA-hairpin triplex and its subsequent elimination from the nucleus, the co-localization over all the time points suggests that the fluorophores in the nuclei and in the cytosol are always somehow bound together, thus the results corroborates our hypothesis of the recognition of NF-κB by the probe and the delivery of the entire adduct back to the cytoplasm.

2.4 Conclusions

In conclusion in this chapter an oligonucleotide sequence was specifically designed to bind NF-κB protein thanks to a consensus sequence. Despite double helix hairpins have already been studied as probe due to the selectivity of the recognition of DNA sequences, very little literature was produced exploiting hairpin-triplexes as probe for protein detection. Furthermore, the exploitation of FRET signal can give information on different conformation of the probe and it can thus be related to binding states between the probe and the NF-κB.

From the results obtained in solution, it seems that the probe is stable under different pH conditions and its behaviour in PBS implemented with 10 mM of $MgCl_2$ is an equilibrium between a H-FRET and L-FRET conformation.

Even so, a titration with NF-κB in solution at physiological conditions revealed a binding ability of the probe. Indeed, a strong decrease of the acceptor/donor ratio can be observed upon increasing concentration of NF-κB. A quantitative analysis was however complicated to perform, since the initial conformation is already an equilibrium between two states.

Even so, at least qualitative analysis on the fate of the probe once transfected *via* lipofectamine can be done. Therefore, prostate cancer cells (PC3) were transfected with the triplex-haipin probe. Overall, we demonstrated that the probe is efficiently delivered in the cytosol and in the nucleus after 2 hours of incubation and it can recognize NF-κB protein in both the cells compartments. Indeed, a decrease of A/D signal is detected within 6 hours in cytosol, where the protein results constitutively active due to upregulation in cancer cells. The rate of binding in the nucleus seems faster, since the signal obtained in this part of the cells remained constant over all the time of the experiments. Interestingly, the signal from the nuclei was transient, in fact after 12 hours almost no cells showed fluorescence from the nuclei, but only from the cytosol. This fate can be due to the cascade event of the interaction between NF-κB and genes in nucleus which promote the production of IκB protein, able to recognize NF-κB protein and deliver it back to the cytoplasm.

In conclusion, due to the short tail of the hairpin able to pair in a Hoogsteen pairing (triplex region) the probe does not show a no-FRET state but an energy transfer signal can always be detected in bound and unbound states, because of the proximity of the fluorophores in both the conformations. Furthermore, despite from the melting plot measurements the probe resulted very stable in PBS, the amount of energy transfer detected in solution is lower than the maximum amount detected in cell environment. Thus, it seems that, at least in cuvette, the equilibrium between the L-FRET and H-FRET (triplex) is not definitely shifted toward the triplex conformation, making it difficult to obtain quantitative result in solution.

Nonetheless, extending the sequence of the Hoogsteen-pairing bases of the probe could be a good way to improve the energy transfer efficiency in solution. This study demonstrated that the hairpin-triplex probe used is a promising alternative to the most known studied double helix DNA hairpins, able to monitor the fate of NF-κB protein in live cells for at least 24 hours.

2.5 References

[1] R. Sen and D. Baltimore, ‘Inducibility of K lmmunoglobulin Enhancer-Binding Protein NFKB by a Posttranslational Mechanism’, p. 8.

[2] T. Huxford and G. Ghosh, ‘A Structural Guide to Proteins of the NF- B Signaling Module’, *Cold Spring Harbor Perspectives in Biology*, vol. 1, no. 3, pp. a000075–a000075, Sep. 2009, doi: 10.1101/cshperspect.a000075.

[3] S. J. Furney, D. G. Higgins, C. A. Ouzounis, and N. López-Bigas, ‘Structural and functional properties of genes involved in human cancer’, *BMC Genomics*, vol. 7, no. 1, p. 3, Dec. 2006, doi: 10.1186/1471-2164-7-3.

[4] J. Huang, J. Wu, and Z. Li, ‘Biosensing using hairpin DNA probes’, *Reviews in Analytical Chemistry*, vol. 34, no. 1–2, pp. 1–27, Jan. 2015, doi: 10.1515/revac-2015-0010.

[5] A. A. Lubin and K. W. Plaxco, ‘Folding-Based Electrochemical Biosensors: The Case for Responsive Nucleic Acid Architectures’, *Acc. Chem. Res.*, vol. 43, no. 4, pp. 496–505, Apr. 2010, doi: 10.1021/ar900165x.

[6] E. N. Nikolova, G. B. Goh, C. L. Brooks, and H. M. Al-Hashimi, ‘Characterizing the Protonation State of Cytosine in Transient G·C Hoogsteen Base Pairs in Duplex DNA’, *J. Am. Chem. Soc.*, vol. 135, no. 18, pp. 6766–6769, May 2013, doi: 10.1021/ja400994e.

[7] A. Beck, V. Vijayanathan, T. Thomas, and T. J. Thomas, ‘Ionic microenvironmental effects on triplex DNA stabilization: Cationic counterion effects on poly(dT)·poly(dA)·poly(dT)’, *Biochimie*, vol. 95, no. 6, pp. 1310–1318, Jun. 2013, doi: 10.1016/j.biochi.2013.02.012.

[8] A. Glab *et al.*, ‘Dissecting the intracellular signalling and fate of a DNA nanosensor by super-resolution and quantitative microscopy’, *Nanoscale*, vol. 12, no. 28, pp. 15402–15413, 2020, doi: 10.1039/D0NR03087B.

PART B

Hyaluronic acid derivatization with luminescent moieties

Chapter 3 - Derivatization of HA with dansyl chloride

3.1 Introduction

Dansyl (5-dimethylaminonaphthalene-1-sulfonyl chloride) is an organic molecule widely used in fluorescence-based probes due to its high quantum yield, its anti-interference ability for its large stokes shift of more than 200 nm and its ability to respond to different surrounding environment by exhibiting wavelength shifts according to the polarity of the solvent.

This phenomenon is known as solvatochromism [1] and it is the ability of some molecules to change their spectroscopic properties upon changes in the environment. Solvatochromic effects are non-trivial and they are based on the different interactions of the molecule in its ground and the excited state – that are thus differently stabilized – with the solvent, mainly depending on its dielectric constant and hydrogen bonding capacity. The absorption and luminescence bands of the solvatochromic dyes can thus largely depend on the nature of th esolvent [2].

For this reason, although the absorption of the dansyl is in the near UV (λ^{A}_{max} = 330 nm), this dye has been used in several applications, such as the detection of metals in cells or for the detection of aminoacids [2], [3]. Because of its properties, we have derivatized HA with dansyl molecules in order to obtain a natural polymer-based probe presenting the photochemical advantages of dansyl; the results are presented in thischapter.

3.2 Materials and methods

5-dimethylaminonaphthalene-1-sulfonyl chloride, Pluronic F-127, acetic acid 1M, Sodium Chloride (NaCl>99,), Tetraethyl orthosilicate (TEOS, 99.9%), Trimethylsilyl chloride (TMSCl 99%), dimethylformamide (DMF 99.8%), N-(3-Dimethylaminopropyl)-N′-ethylcarbodiimide hydrochloride (EDC·HCl), N-Hydroxysulfosuccinimide sodium salt (sulfo-NHS), trimethylamine (TEA), ethylendiamin (EDA) were purchased from Sigma Aldrich., Rhodamine isothiocyanate (RITC). Hyaluronic acid cosmetic grade was purchased from Stanfordchem, California, US.

Cellulose tube was purchased from Sigma, mol wt. Cut-off > 12 KDa, avg. 33 mm diameter. RC Durapore filters (0.45 micron pores dimension) were purchased from Millipore.

3.2.1 functionalization of hyaluronic acid with dansyl chloride

1 mL of EDA (14.9 mmol, 40 eq.) was placed into a round bottomed flask under magnetic stirring. Dansyl chloride (100 mg, 0.370 mmol, 1 eq.) was dissolved in 6 mL of DCM and let it drop into the EDA solution at 0°C. Afterwards, the mixture was kept under magnetic stirring for 1h at RT and extracted with 10 mL of HCl 0.1 M. The aqueous phase was brought to pH = 9 with NaOH and extracted with DCM (2x20 mL). The organic phase was dried over $MgSO_4$ and filtered. The solvent was removed under reduced pressure and the product **1** was obtained with a final yield of 91%.

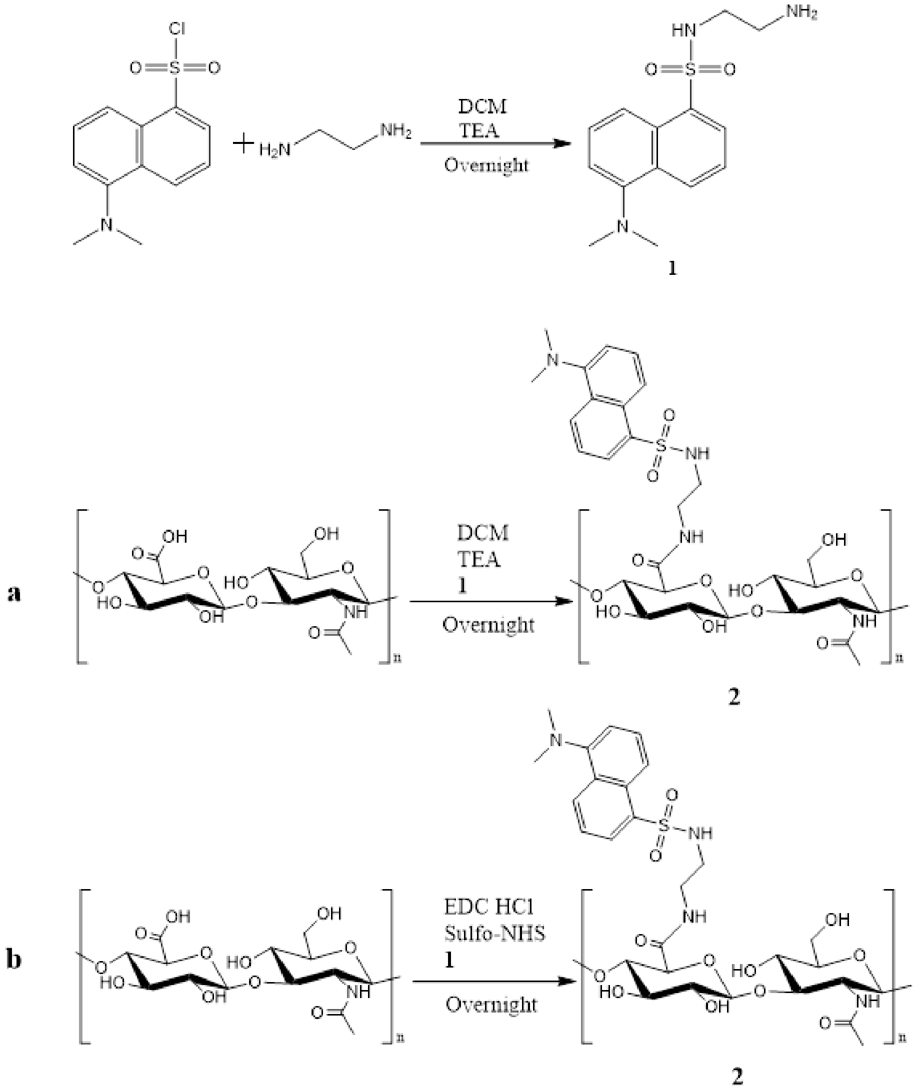

Scheme 3.1: steps of functionalization reaction of dansyl chloride with hyaluronic acid in DMSO (a) or aqueous buffer (b).

Mechanism a: 30 mg of HA were suspended in 3 mL of DMSO in a 20 mL glass vial. Sulfo-NHS (17 mg, 78 µmol, 5 eq.), EDC (15 mg, 78 µmol, 5eq.), TEA (21.7 µL, 0.156 mmol, 1 eq.) and dansyl-EDA (**1**) (18 µmol, 1 eq.) were added to the HA suspension. The mixture was kept under magnetic stirring at room temperature overnight. The product was purified by dialysis against Milli-Q water for 48 h, the dialyzed solution was diluted to a total volume of 10 mL with Milli-Q water and then purified again through liquid extraction with EtOAc.

Mechanism b: 30 mg of HA were inserted in 20 mL glass scintillation vial and dissolved in 3 mL of Triton X-100 solution in borate buffer pH= 9. Sulfo-NHS (17 mg, 0.078 mmol, 5 eq.), EDC (15 mg, 0.078 mmol, 5eq.), TEA (21.7 µL, 0.156

mmol, 1 eq.) and **1** (0.052 mmol, 3 eq.) were added to the HA solution. The molar excess has been calculated in order to obtain a functionalization degree of 30% compared to the monomers present in the HA chain. The mixture was kept under magnetic stirring at room temperature for one night. The product was purified by dialysis against Milli-Q water for 48h, the dialyzed solution was diluted to a total volume of 10 mL with Milli-Q water.

3.2.2 synthesis of PluSNPs

Synthesis of PluSNPs was performed according to the procedure already published in literature [4].

200 mg of PLURONIC F-127, 38 mg of NaCl were solubilized in 3.1 mL ofacetic acid 1M. after a complete solubilisation, 360 µL of TEOS were added to the mixture at RT. The reaction was carried out under magnetic stirring for 2 hours and then 20 µL of TMSCl were added. After 20 hours, PluSNPs were purified *via* dialysis versus MilliQ water for three days. The sample was diluted to 10 mL of MilliQ water, obtaining a 20 µM solution.

3. 3 Results and discussion

3.3.1 Synthesis and characterization of hyaluronic acid with dansyl chloride

The first step of the synthesis of hyaluronic acid conjugated with dansyl (from now on HA@Dansyl) was the functionalization of dansyl chloride with a diamine linker. By dropping dansyl into the EDA solution we were able to have a local concentration of amine higher than that of dansyl, thus avoiding the presence of non-reacted dansyl and also the formation of the dimer dansyl-EDA-dansyl. Liquid extraction with HCl 0.1 M allowed to separate the dimer (soluble in organic solvent) from the non-reacted EDA (water soluble) and Dansyl-EDA, soluble in aqueous media upon protonation. After bringing the aqueous fraction to pH = 9, a second extraction with DCM was performed, to collect the deprotonated Dansyl-EDA in the organic fraction.

The second step of the reaction was performed *via* EDC and sulfo-NHS ,a couple of activating agents very used in amidation reactions [5].

EDC reacts with carboxylic acids to form a *o*-acylisourea intermediate in equilibrium with its hydrolysed form. In presence of Sulfo-NHS, the intermediate forms an ester having a good leaving group, but which is also stable enough to allow the reaction between hyaluronic acid and dansyl-EDA.

Since the main problem of this synthetic strategy is the hydrolysis of EDC in aqueous environment, carrying out the reactions in a polar organic solvent (reaction **a** in the scheme 1) or in buffer (**b**) under acidic pH during this step were both efficient methods able to slow down the EDC hydrolysis rate.

Beyond this issue, it must be taken into account that hyaluronic acid and sulfo-NHS in case **a** cannot be efficiently solubilised in organic solvents and for this reason they were suspended in DMSO under vigorous stirring, while EDC was fully solubilised in the organic medium.

On the other hand, considering the mechanism b, although HA and the activating agents are completely soluble in aqueous media, organic dyes as dansyl are not, therefore the use of the non-ionic surfactant Triton-X 100 helped to increase the solvation of the dansyl.

The purification step *via* dialysis was necessary in order to exchange the DMSO with water (in case **a**) and to expel small molecules, i.e. EDC, sulfo-NHS and unbound dansyl-EDA, able to cross the 12 KDa membrane. Moreover, to ensure a complete removal of unreacted dansyl-EDA, a further purification step *via* extraction with EtOAc was performed.

3.3.2 Photophysical characterisation of HA@Dansyl

The spectra of a solution of known concentration of dansyl in methanol and water were recorded (figure 3.1)

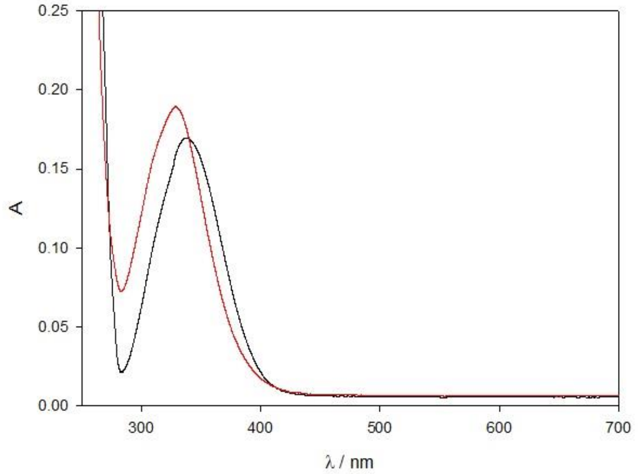

Figure 3.1 Absorption spectra of Dansyl-EDA 43.8 μM in MeOH (black) and water (red).

The dansyl-EDA shows a maximum peak at 340 nm in methanol (black line) while in water a 10 nm bathochromic shift occurs (red line). As well-known from literature, interaction between solute molecules and solvent can alter molecular geometries, electronic distribution and thus they affect spectroscopic properties. Indeed, properties of the solvent such as hydrogen bonding capability or dielectric constant differently stabilize both ground and excited states of solutes, therefore resulting in changes in shape, position and molar absorption coefficient of their absorption spectra. This phenomenon is known as solvatochromism and dansyl-EDA molecules are greatly subjected to this process because of the presence of dimethyl amino group (electron pair acceptor) able to interact with hydrogen bond donor solvents and because of the presence of sulfonamido group (electron pair donor) can interact with hydrogen bond acceptor solvents. Dansyl is therefore widely used as probe for its ability to detect differences in the surrounding environment.

The molar extinction coefficient ε at the wavelength of maximum absorption were determined to be 4310 $M^{-1}cm^{-1}$ in water.

We recorded the absorption and emission spectra of HA@Dansyl samples synthesised via a and b (figures 3.2 and 3.3), in order to calculate the doping degree for each reaction and the fluorescence quantum yield of the systems according to the following equations.

$$[Dansyl] = \frac{A}{b \times \varepsilon_c} \qquad \text{Eq. 3.1}$$

$$DD(\%) = \frac{[Dansyl]}{[RU]} \times 100 \qquad \text{Eq. 3.2}$$

$$\Phi = \Phi_r \frac{I\, A_r\, n^2}{I_r A\, n_r^2} \qquad \text{Eq. 3.3}$$

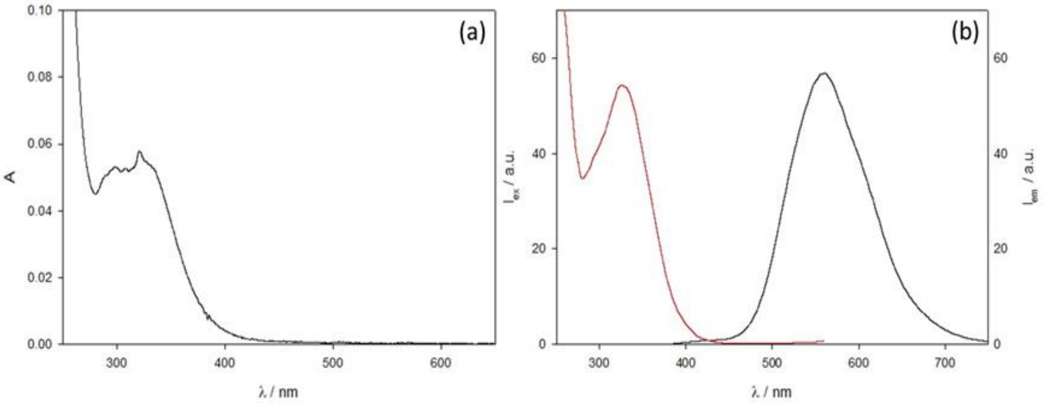

Figure 3.3. a) absorption, b) emission (black line, λ_{ex} = 340 nm) and excitation (red line, λ_{em} = 580 nm) spectra of HA-Dansyl derivative synthetized in buffer solution.

In this case, fluorescein in NaOH 0.1 M (Φ_r = 0.92) was used as a reference in equation 3.3. The quantum yield and the functionalization rate values are reported in Table 3.1.

Table 3.1: doping degree, number of dyes per filament and fluorescence quantum yield for HA@Dansyl synthesised in DMSO and buffer.

Samples	**DoF (%)**	**N° dyes/filament**	***Φ***
HA@Dansyl (DMSO)	2.5	20	-
HA@Dansyl (buffer solution)	6.0	50	0.04

Both systems present an absorption peak at 330 nm, consistent with the peak observed for dansyl derivative in water. Nonetheless, the synthesis carried out in DMSO presents a lower doping degree compared to the one carried out in aqueous media. This can due to the high hydrophilicity of the HA scaffold, that resulted in a more opened conformation in buffer compared to DMSO, with the carboxylic acid groups being more accessible to the dansyl-EDA. For the HA@Dansyl synthesised in aqueous medium, the wavelength of the peak of the fluorescence band, the excited state lifetime and the quantum yield are comparable to those reported for the dansyl-EDA in water. Therefore, this proves that, since the HA conformation in water is mainly unfolded, the major fraction of dansyl molecules is experiencing aqueous environment, while only a small fraction is in the hydrophobic pockets of HA. In these areas the dye has a higher fluorescence emission than the one of the dansyl in pure water, leading to a quantum yield of $\Phi = 0.04$ at 560 nm, only slightly higher to the value tabulated for a dansyl reference compound in water solution ($\Phi = 0.03$) [6].

3.3.3 Interactions with nanomaterials

Due to the high degree of functionalization (DoF,) we investigated the interaction between 6% doped HA@Dansyl derivative with nanomaterials. As reference nanomaterials we used Pluronic silica nanoparticles (PluSNPs) due to the ease of their synthesis and because their properties, as dimensions, surface charge and homogeneity in solution, are well known and extremely reproducible.

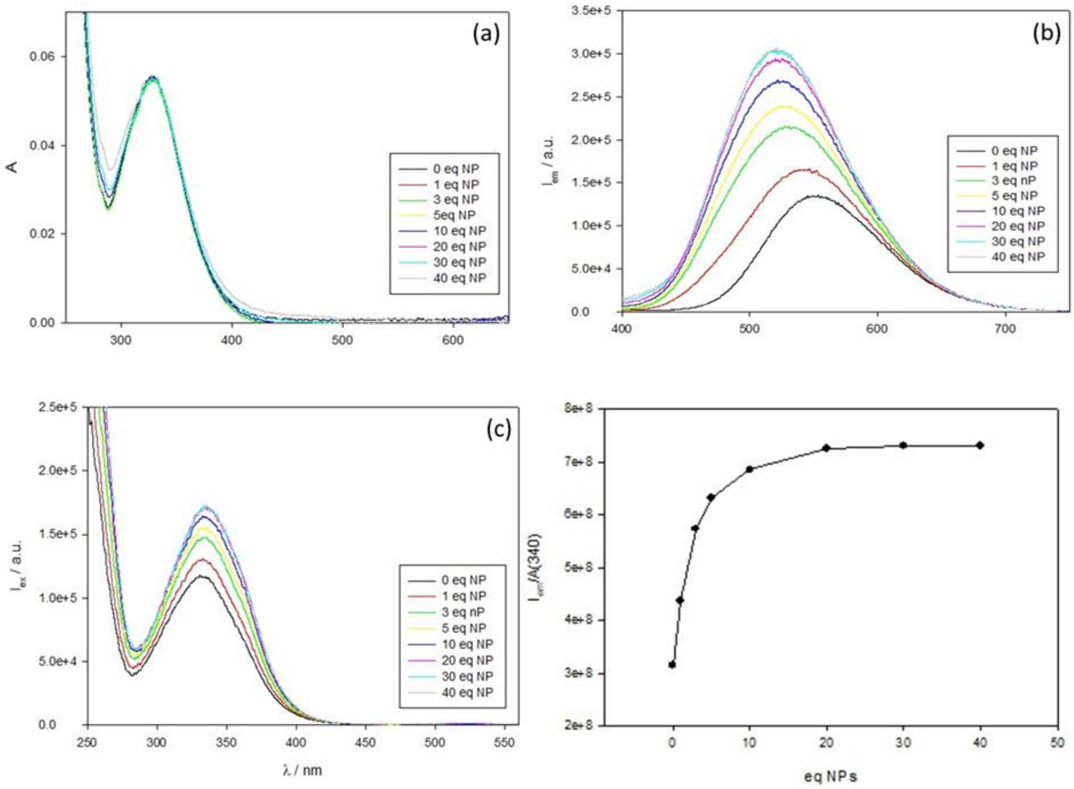

Figure 3.4. absorption (a), emission (λ_{ex} = 350 nm) (b) and excitation (λ_{em} = 580 nm) spectra (c) of HA-Dansyl upon addition of increasing amount of PluSNPs; Trend of the relative emission intensity compared to the NP molar excess (d)

Figure 3.4 shows that, despite no changes in absorption are registered upon the addition of increasing amount of PluSNPs, an increase of the emission intensity during the titration is observed. With a 30-fold molar excess of NPs respect to HA filaments, fluorescence emission increases of about 140%; beyond this value a plateau is reached, indicating that all the hyaluronic acid filaments have already been interacting with PluSNPs.

The emission spectra show also a blue shift of the emission maxima of approximately 40 nm from the maximum registered for HA@Dansyl derivative in absence of NPs.

These results can be explained considering that, as already discussed above, HA derivatives in water assume a random coil conformation, which leads the dansyl dyes to be mostly exposed to a polar environment. Subsequently, upon addition of PluSNPs, characterized by PLURONIC arms around the silica core, HA interacts with them by surrounding PluSNPs and thus forming a layer of polymer around the

PEG shell of silica nanoparticles, in agreement with previously obtained results. The more PluSNPs are added, the more HA is led toward the expansion of its natural coil conformation and during this process the dansyl molecules interact with the shell of PluSNPs. This interaction brings dansyl in a less polar environment than water, characterized by a higher energy fluorescence band, a longer excited state lifetime and a higher quantum yield. A plateau in the fluorescence is then reached upon the addition of about 30-fold molar excess of nanoparticles. This trend is represented in Figure 3.4 d, which shows the emission intensity (normalized on Dansyl absorbance) as function of the NP molar excess. Moreover, the emission peak not only increases its intensity but it also shows a blue shift of 40 nm from the maximum registered for HA-Dansyl derivative in absence of NPs. It’s well known that dansyl is a solvatochromic dye, which fluorescence exhibit a dependence on solvent polarity. Going into details, the lowest excited state S_1 is a non-charge transfer state and S_2 is a TICT state (Twisted Intramolecular Charge Transfer) and they are very close in energy to each other. On the other hand, the dipole moment of S_2 state is higher than that of S_1 state. Therefore, polar solvents stabilize S_2 more than S1 and this may cause a level inversion of dansyl two lowest excited states, having S_2 at a lower energy than S_1. Therefore, in polar solvents the emission would take place from the charge transfer S_2 state. Conversely, going toward a less polar solvent, the extent of the interaction between the S_2 state and the aqueous solution decreases. For this reason theS_2 state is poorly stabilized and its energy increases, bringing back the S_2 slightly above S_1. Since the energy gap between S_2 and the ground state S_0 increases,. a blue shift of the fluorescence emission takes place [7].

Therefore, since the PEGylated shell of PluSNPs represents a less polar environment than aqueous media, the interaction between the NPs and the HA@dansyl causes the dansyl molecules to be trapped into the PEG arms and thus the fluorescence emission is shifted towards shorter wavelengths. The interactions between the NPs and HA system are also confirmed by fluorescence lifetime and anisotropy measurements. The results are reported in Table 3.2.

Table 3.2. Fluorescence lifetimes and anisotropy values for HA-Dansyl derivative with NPs.

	τ / ns (λ_{em}= 580 nm)	**B**	**$\chi 2$**	**Anisotropy**
0 eq. NPs	τ_1= 2.95	B_1= 939	0.690	<0.05
1 eq. NPs	τ_1= 2.88 τ_2= 16.86	B_1= 985 B_2= 69	1.051	0.08
10 eq. NPs	τ_1= 2.96 τ_2= 17.96	B_1= 826 B_2= 179	1.088	0.08
40 eq. NPs	τ_1= 3.22 τ_2= 16.81	B_1= 704 B_2= 279	1.099	0.12
80 eq. NPs	τ_1= 3.35 τ_2= 16.11	B_1= 649 B_2= 341	1.066	0.17

In absence of NPs in solution, HA system fluorescence decay is fitted by a mono-exponential fitting, even if χ^2 a non-optimal value. The excited state lifetime is about 3 ns, according to the tabulated value of the reference compound [6], [2]. Upon addition of PluSNPs the decay is best fitted by a bi-exponential curve, with a shorter component already observed and a longer one of about 17 ns. Moreover, the population of the shorter excited state (B_1) decreases while the population (B_2) of the longer lifetime excited state progressively becomes higher, as shown in Tab 3.2.

In the table the values of anisotropy are also reported. The fact that the anisotropy of dansyl when only bound to HA is extremely low is a proof of the mobility of the HA@dansyl in water solution. Indeed, the dansyl maintain the ability to partially rotate and it can be efficiently depolarized, generating a low anisotropy value. Upon addition of PluSNPs, as HA@dansyl starts to interact with the shell of nanoparticles, the dansyl molecules are stuck between HA and the PEG arms, resulting in a limited motion and higher values of emission anisotropy.

3.4 Conclusions

In this chapter we efficiently derivatized hyaluronic acid with dansyl moiety. Two synthetic procedures were carried out in different solvents and it resulted that the one conducted in aqueous media gave the most efficient conjugation. The sample of HA@dansyl obtained was photochemically characterized and finally its interaction with PluSNPs was investigated. The interaction between HA and the shell of nanoparticles led the dansyl molecules to stay very close to the nanoparticles surface. As expected, due to dansyl solvatochromic properties, the more PluSNPs were added the more the fluorescence peak of dansyl increased and the more it resulted blue shifted.

Therefore, we proved that HA@dansyl is a promising probe for the evaluation of the polarity of the surrounding environment. Furthermore, since the sensing ability of dansyl toward small molecules and molecules of biological interest is already known, the efficient coupling of this dye with a hydrophilic and biocompatible scaffold as HA is could improve dansyl further application as a probe in biological environment.

3.5 References

[1] A. Marini, A. Muñoz-Losa, A. Biancardi, and B. Mennucci, ‘What is Solvatochromism?’, *J. Phys. Chem. B*, vol. 114, no. 51, pp. 17128–17135, Dec. 2010, doi: 10.1021/jp1097487.

[2] L. Prodi *et al.*, ‘Dansylated polyamines as fluorescent sensors for metal ions: Photophysical properties and stability of copper(II) complexes in solution’, *Helvetica Chimica Acta*, vol. 84, no. 3, pp. 690–706, 2001, doi: 10.1002/1522-2675(20010321)84:3<690::AID-HLCA690>3.0.CO;2-L.

[3] B. E. Leonard and N. N. Osborne, ‘The Use of Dansyl-Chloride for the Detection of Amino Acids and Serotonin in Nervous Tissue’, in *Research Methods in Neurochemistry*, N. Marks and R. Rodnight, Eds. Boston, MA: Springer US, 1975, pp. 443–462.

[4] E. Rampazzo *et al.*, ‘Pluronic-Silica (PluS) Nanoparticles Doped with Multiple Dyes Featuring Complete Energy Transfer’, *J. Phys. Chem. C*, vol. 118, no. 17, pp. 9261–9267, May 2014, doi: 10.1021/jp501345f.

[5] G. T. Hermanson, ‘Zero-Length Crosslinkers’, in *Bioconjugate Techniques*, Elsevier, 2013, pp. 259–273.

[6] M. Montalti *et al.*, ‘Langmuir 2006, 22, 5877-5881.pdf’, no. 3, pp. 5877–5881, 2016.

[7] J. R. Lakowicz, Ed., ‘Solvent and Environmental Effects’, in *Principles of Fluorescence Spectroscopy*, Boston, MA: Springer US, 2006, pp. 205–235.

Chapter 4 - Derivatization of HA with pyrene

4.1 Introduction

In this chapter will be discussed the functionalization of HA with two pyrenes derivatives, namely 1-aminopyrene (PA) and 1-pyrenemethilamine hydrochloride (PMA).

Pyrene is an aromatic molecule absorbing light in the near UV and emitting in the blue part of visible region. Its peculiarity is the formation of excimers having a characteristic red shifted emission band. Indeed, while the emission band of the monomer is structured, with 3 peaks maxima at 375, 396 and 417 nm, when excimers are formed, a broad band centered around 480 nm can be observed.

Exploiting this feature, pyrene has been used in literature as a probe for different processes and analytes, e.g., for micelle formation or ion detection [1], [2].

Therefore, by anchoring pyrene molecules to an extended structure as hyaluronic acid, could give interesting information on its conformation in different environments.

4.2 Materials and methods

- 1-aminopyrene (PA) and 1-pyrenemethilamine hydrochloride (PMA), Pluronic F-127, acetic acid 1M, Sodium Chloride (NaCl>99,), Tetraethyl orthosilicate (TEOS, 99.9%), Trimethylsilyl chloride (TMSCl 99%), dimethylformamide (DMF 99.8%), N-(3-Dimethylaminopropyl)-N′-ethylcarbodiimide hydrochloride (EDC·HCl), N-Hydroxysulfosuccinimide sodium salt (sulfo-NHS), trimethylamine (TEA), ethylendiamin (EDA) were purchased from Sigma Aldrich., Rhodamine isothiocyanate (RITC. Rhodamine B-Si(OEt)3, were previously synthesised in our lab. Hyaluronic acid 400 KDa cosmetic grade were purchased from Stanfordchem, California, US.

Cellulose tube was purchased from Sigma, mol wt. Cut-off > 12 KDa, avg. 33 mm diameter. RC Durapore filters (0.45 micron pores dimension) were purchased from Millipore.

4.2.2 Functionalization of hyaluronic acid with 1-aminopyrene

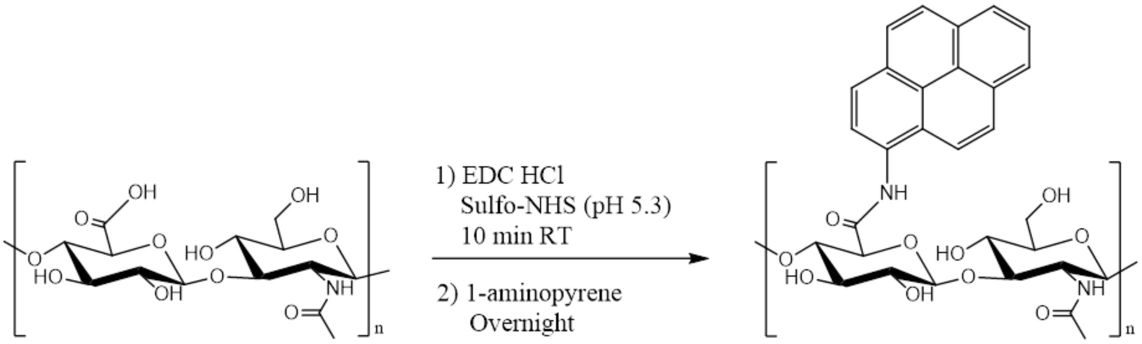

Scheme 4.1 reaction scheme of hyaluronic acid with 1-aminopyrene in aqueous buffer.

10 mg of HA were inserted in 20 mL glass scintillation vial and dissolved in 10 mL of phosphate buffer pH= 5.3. Sulfo-NHS (250 μL of a 0.1 M solution, 0.026 mmol, 5 eq.) and EDC (250 μL of a 0.1 M solution, 0.026 mmol, 5 eq.) were added to HA solution. After 10 minutes, 1-aminopyrene (1.09 mg, 0.005 mmol, 1 eq.), previously suspended in 2 mL of 10 mM Triton X-100 solution in borate buffer pH= 9, was added and the pH of HA solution was adjusted with NaOH 1 M until it became slightly basic (above pH= 7). The molar excess has been calculated in order to obtain a functionalization degree of 10% compared to the monomers present in the HA chain. The mixture was kept under magnetic stirring at room temperature for one

night. The product was purified *via* dialysis with Milli-Q water/DMF against Milli-Q water (48 hours) and then by ultrafiltration, (cut-off of 10 kDa).

4.2.3 Functionalization of hyaluronic acid with methyl-aminopyrene

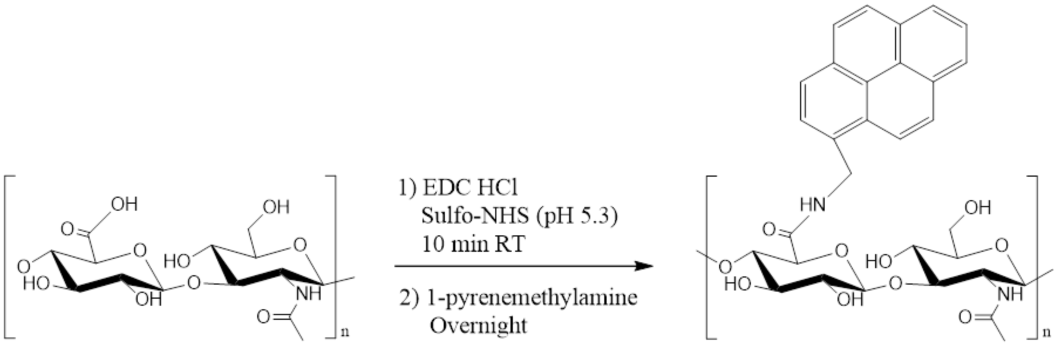

Scheme 4.2: reaction scheme of hyaluronic acid with 1-aminopyrene in aqueous buffer.

10 mg of HA were inserted in 20 mL glass scintillation vial and dissolved in 10 mL of phosphate buffer pH= 5.3. Sulfo-NHS (250 µL of a 0.1 M solution, 0.06 mmol, 5 eq.) and EDC (250 µL of a 0.1 M solution, 0.026 mmol, 5 eq.) were added to HA solution. The acid environment slows down EDC hydrolysis. After 10 minutes, 1-pyrenemethylamine (1.34 mg, 0.005 mmol, 1 eq.), previously suspended in 2 mL of 10 mM Triton X-100 solution in borate buffer pH= 9, was added to HA solution and the pH was adjusted with NaOH 1 M until it became slightly basic (above pH= 7). The molar excess has been calculated in order to obtain a functionalization degree of 10% compared to the monomeric units present in the HA chain. The mixture was kept under magnetic stirring at room temperature for one night. The product was purified first by dialysis for 48h, Milli-Q water/DMF against Milli-Q water and then by ultrafiltration, (cut-off of 10 kDa). The dialyzed solution was diluted to a total volume of 10 mL with Milli-Q water.

4.3 Results and discussion

4.3.1- Synthesis and characterization of hyaluronic acid with aminopyrene

The functionalization of HA with 1-aminopyrene (HA@PA) and 1-pyrenemethylamine (HA@PMA), showed in Scheme 4.1 and 4.2, has been carried in both cases in buffer-Triton X-100 solution. In the first step of the reactions, HA has been solubilized in a phosphate buffer with a pH = 5.3 and then the coupling agents have been added. The slightly acid environment slows down o-acylisourea intermediate hydrolysis and promotes the formation of the stable ester intermediate. In the second step, a basic solution of borate buffer containing the dye has been added to the reaction mixture and the pH has been adjusted above 7. The slightly basic environment is necessary to deprotonate the amine group on the dye.

The purification of the samples involved several steps. At first, a small quantity of DMF has been added to both the reaction mixtures and a neutral dialysis has been performed. The addition of DMF improved the unbound dye solubilisation and it facilitated its removal from the dialysis bag.

Eventually, in order to concentrate and provide a further purification step, the product solutions have been ultrafiltrate with a 10 kDa membrane.

4.3.2 - Photophysical characterisation of HA@PA and HA@PMA

Since the absorbance signal was covered by the scattering, it has not been possible to determinate the actual doping degree and the quantum yield of HA@PA, which however presents well-defined emission and excitation spectra, that are represented in Figure 4.1. The low observed absorbance however indicates that the derivatization obtained in these conditions is limited (< 1%)

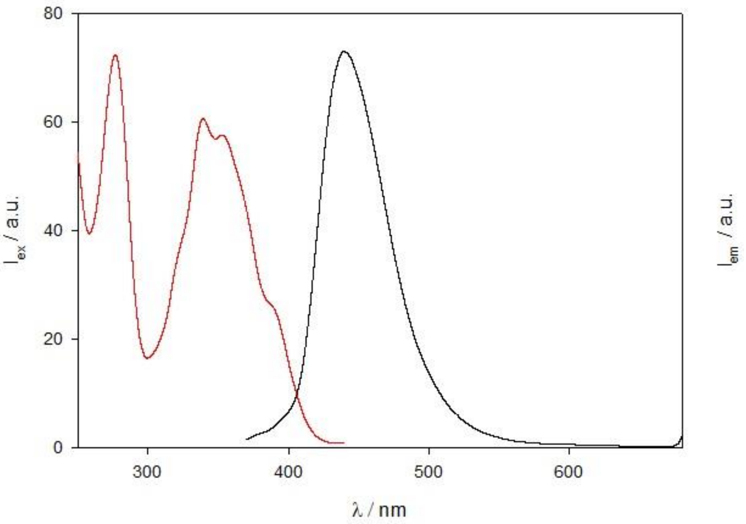

Figure 4.1. Emission (black line, λ_{ex} = 350 nm) and excitation (red line, λ_{em} = 460 nm) spectra of HA-PA derivative.

The HA@PMA absorption spectrum (4.2) and the tabulated molar extinction coefficient [3] for pyrene have been used to an indirect determination of the doping degree. The fluorescence quantum yield of the system was calculated using quinine sulphate in H_2SO_4 0.5 M as reference compound with known quantum yield (Φ_r = 0.55). The results are reported in Table 4.2.

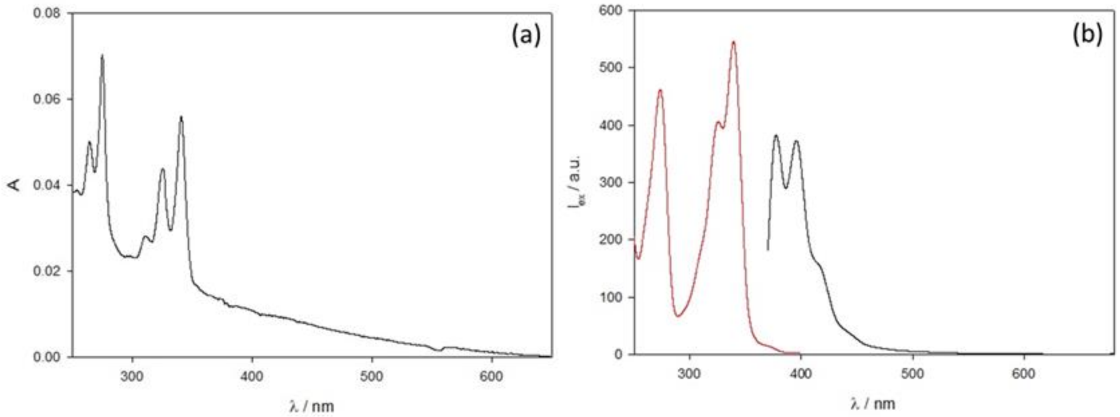

Figure 4.2. a) absorption, b) emission (black line, λ_{ex} = 350 nm) and excitation (red line, λ_{em} = 420 nm) spectra of HA-PMA derivative.

Table 4.2: DoF, number of dyes per HA filament and quantum yield value for HA-PMA derivative.

	DoF (%)	N° dyes/filament	Φ
HA-PMA	1.0	8	0.2

HA-PMA presents a high brightness and fluorescence signal as suggested by a 20% quantum yield value.

4.3.3 – interaction of HA@PA and nanomaterials

Despite it was not possible to determine the degree of functionalization (DoF) of HA@PA, due to the high scattering of the solution, since a strong visible fluorescence signal was observed, it was possible to investigate the interaction between HA@PA and nanomaterials.

In figure 4.3 a and b the emission and excitation spectra upon increasing amount of PluSNPs are shown. Approximately a 25% increase in the emission signal is observed up to the addition of 5 molar excess of PluSNPs versus filament of hyaluronic acid. Moreover, a 20 nm blue shift is also observed during the titration, and also from 5 eq of PluSNPs on, a low intensity peak at 380 nm starts to be observed.

The proper definition of excimer as firstly given by Birk is a dimer which is associated in an electronic excited state and which is dissociative in its ground state [4]. In order to have the formation of excimers, the light should be absorbed locally by one pyrene unit, that can emit as monomer (λ_{max} = 375 nm); however, if upon a diffusive process the excited pyrene encounters a ground state pyrene an excimer is formed and its emission is greatly red shifted to a λ_{max} = 480 nm [4].

There are also cases when excimer-like emissions are observed, even though there are no evidence of an actual separation of the pyrene molecules during the excitation. Therefore, to discriminate the two phenomena, the former case is usually referred to as dynamic excimer and the latter as static excimers.

It’s known from literature that the amide linkage by which the PA is bound to HA does not alter the typical pyrene emissions [5], [6], thus the quite intense peak at λ_{max} = 450 nm is observed in this system was associated to the pyrene excimer emission. Furthermore, since the pyrenes are bound to HA it is not likely that diffusion processes are occurring, thus the most probable situation is that the observed emission could be due to the formation of “static excimers” or pre-formed dimers in their ground state.

Thus, three trends during the titration with PluSNPs are observed simultaneously: i) a blue shift; ii) an increase in the major emission peak; iii) the formation of a second peak at 375 nm.

The three processes considered all together indicates that Pyrene is preferentially bound to some regions of HA, where it can form static excimers, characterized by a higher quantum yield than the monomer peaks, that are thus hidden. Upon interaction between HA@PA and PluSNPs, the HA surrounds the PLURONIC shell and pyrene molecules experience a more rigid and hydrophobic environment, which leads to an increase of emission and to a blue shift, respectively. Indeed, as reported in literature, the excimers of pyrene exhibit a solvatochromic effect [7]. Furthermore, after 5 molar excess of PluSNPs, the conformation of hyaluronic acid is so unfolded that a monomer related peak starts to appear.

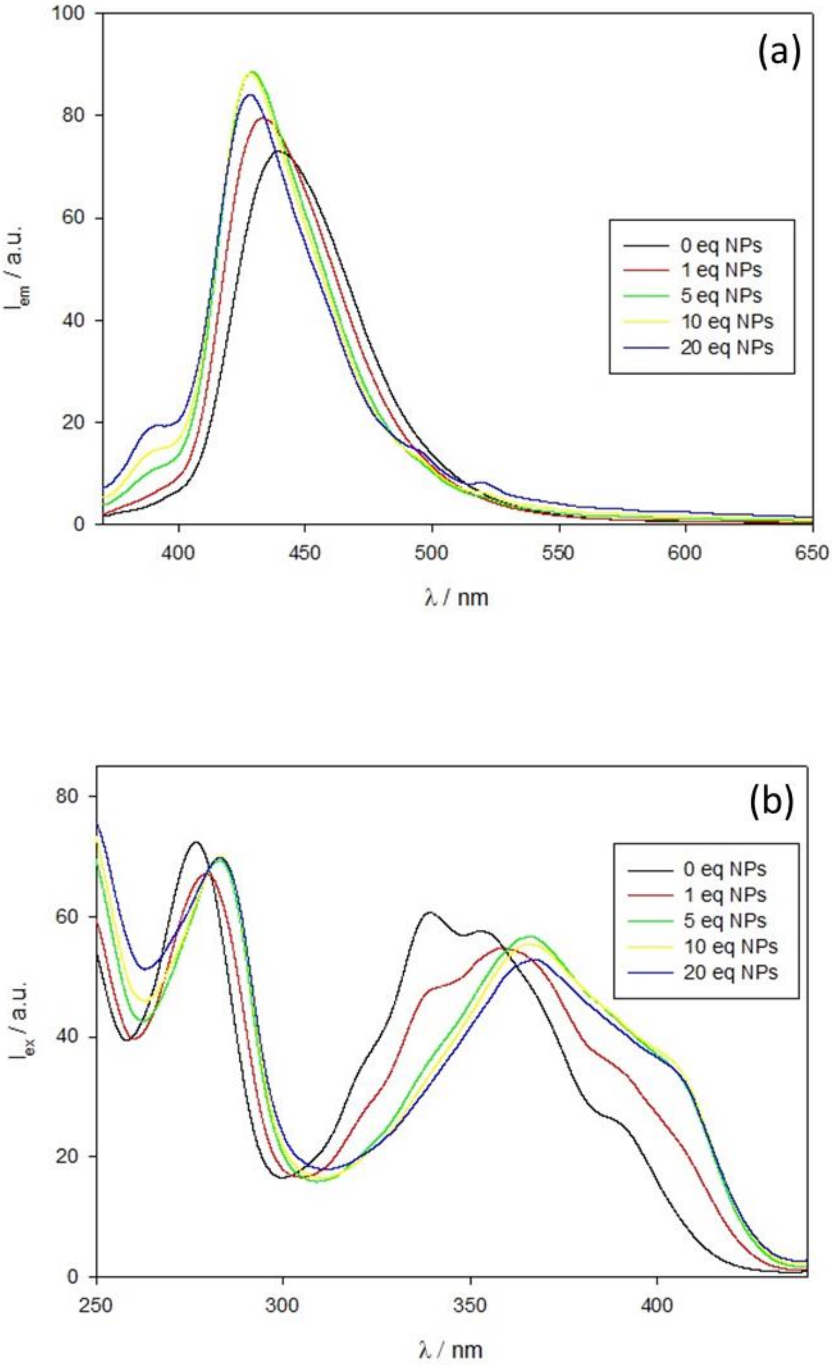

Figure 4.3. a) emission (λ_{ex} = 350 nm) and b) excitation (λ_{em} = 460 nm) spectra of HA@PA upon the addition of increasing amount of NPs.

Surprisingly, the excitation spectra performed during the titration do not follow the same trend of the emission spectra. Nonetheless, a change in the shape upon addition of PluSNPs, toward a broader excitation band is observed and this clearly indicates that the pyrene is experiencing a progressive different environment.

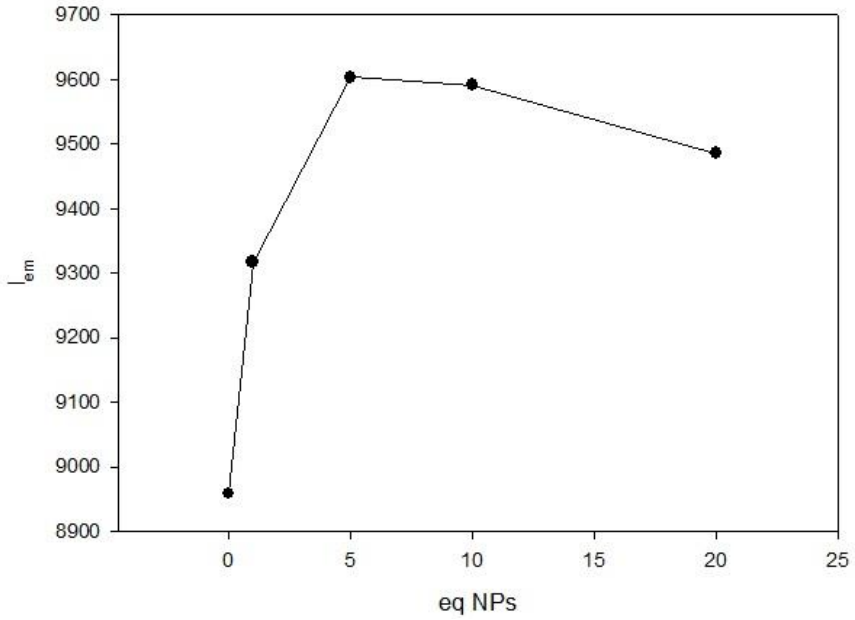

Figure 4.4. Trend of emission intensity compared to the NP molar excess.

Another confirmation of the actual interactions between HA@PA and PluSNPs is provided by the fluorescence lifetime trend during the NPs titration and the emission anisotropy values. The results are reported in Table 4.2

Table 4.2. Fluorescence lifetimes values for HA-PA derivative with NPs.

	τ / ns (λ_{em} = 425 nm)	χ^2	Anisotropy
0 eq.	5.97	0.991	<0.05
1 eq.	6.03	0.988	0.09
5 eq.	6.08	0.994	0.10
10 eq.	6.29	0.996	0.17
20 eq.	6.35	0.993	0.17

The fluorescence decay fits with a mono-exponential function, as suggested by the χ^2 value. In absence of PluSNPs in solution, HA@PA exhibits a short lifetime of only 6 ns and a low anisotropy value. By adding nanoparticles to the solutions, the fluorescence lifetime and anisotropy values slowly start to increase, according to the growth in rigidity of the system and to the limited motion of dye molecules.

4.3.4 – interaction of HA@PMA and nanomaterials

In Figure 4.5 absorption, emission and excitation spectra of the HA@PMA upon titration with nanoparticles are reported. The absorbance at the excitation wavelength (λ_{ex} = 350 nm) is not influenced by the PluSNPs amount in solution, and it remains constant during the titrations. On the other hand, at shorter wavelengths the absorbance values increase while the NPs concentration rises, due to a greater scattering phenomenon generated by the HA + PluNPs solution. Through the emission spectra it is possible to observe how the HA@PMA derivative increases its fluorescence signal of approximately 17% after the addition of PluSNPs of 20-fold molar excess. Beyond this value, the relative fluorescence emission reaches a plateau as shown from the trend in Figure 4.6.

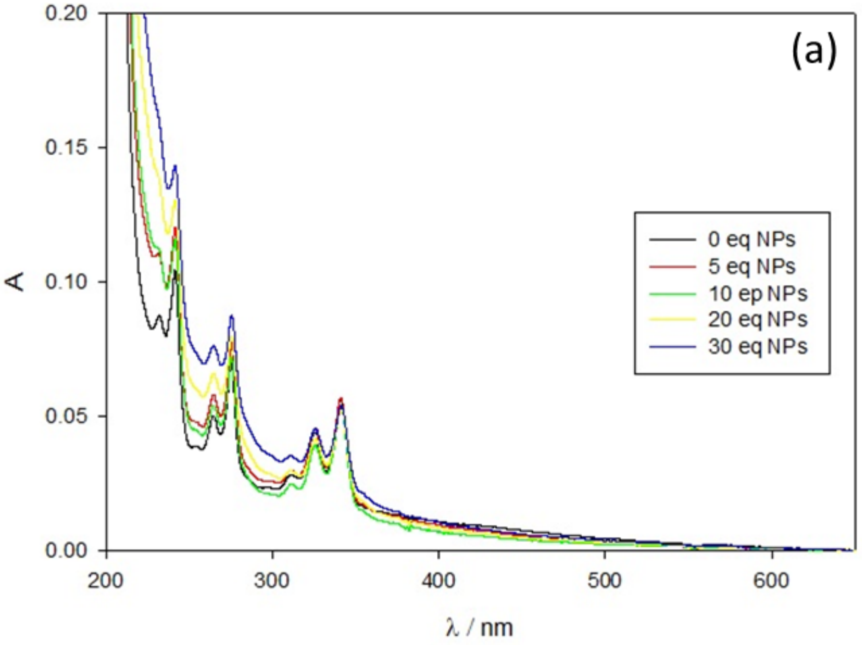

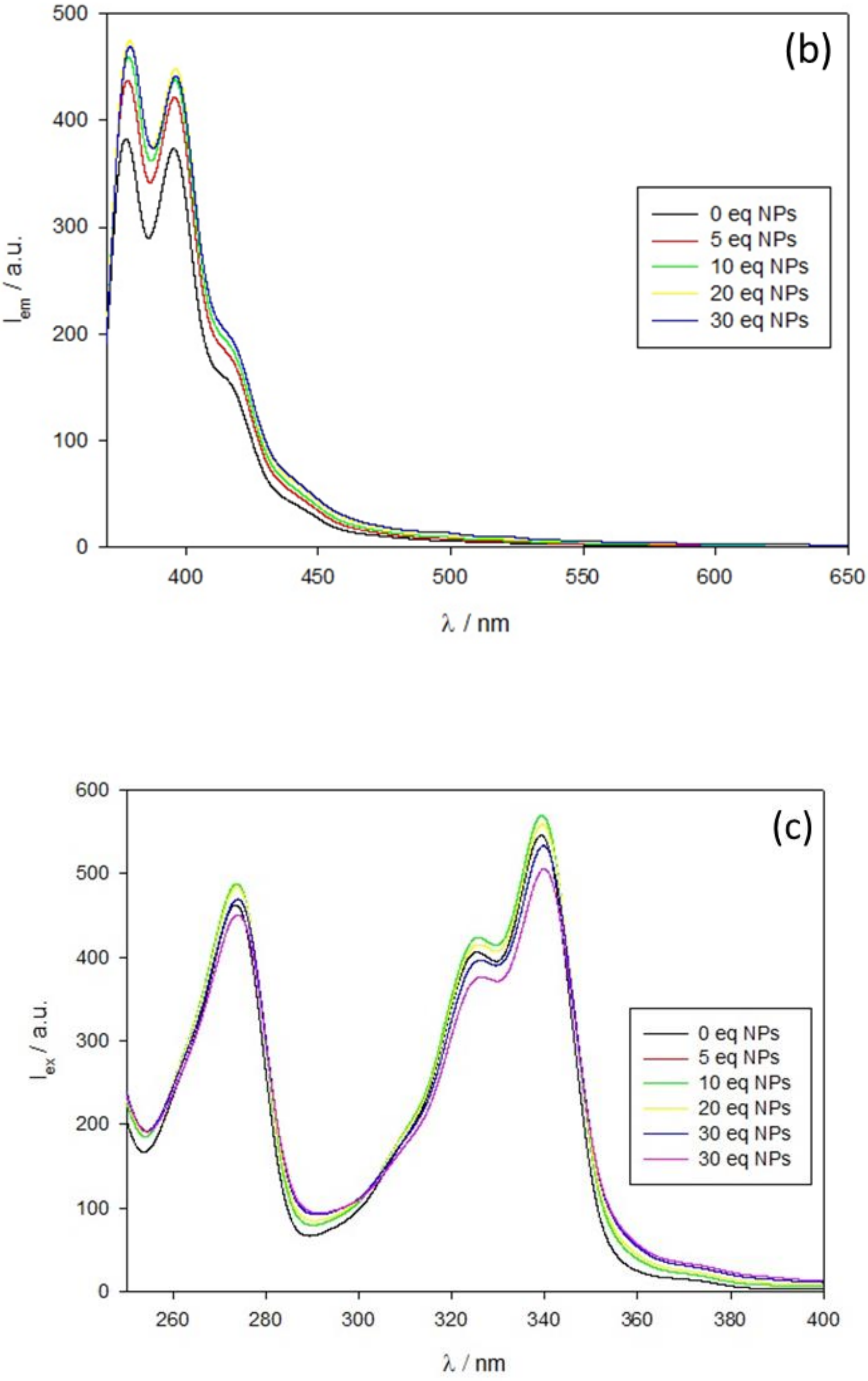

Figure 4.5. a) absorption, b) emission (λ_{ex} = 350 nm) and c) excitation (λ_{em} = 420 nm) spectra of HA-PMA following the addition of increasing amount of NPs.

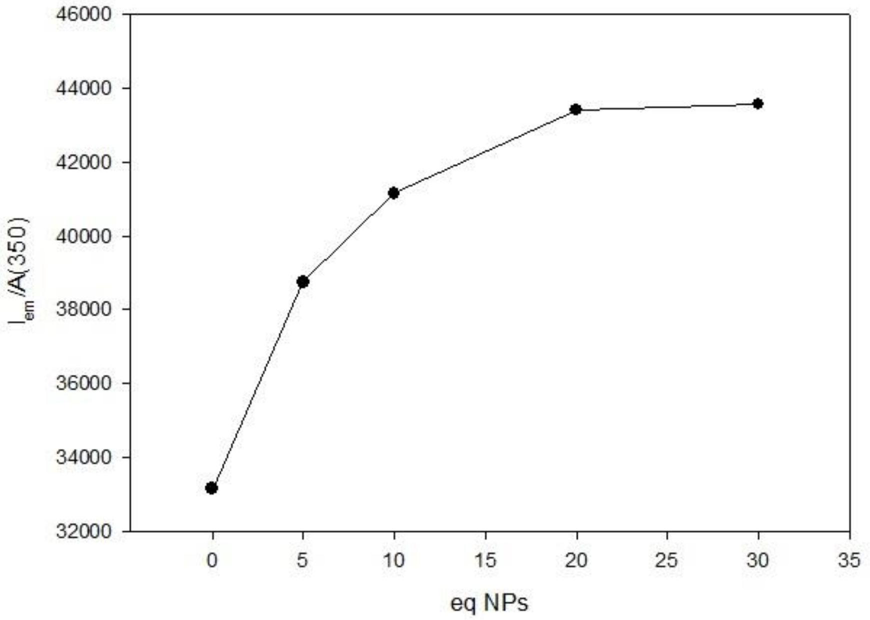

Figure 4.6. Trend of relative emission intensity compared to the NP molar excess.

Moreover, the emission observed is the typical emission structured band of the pyrene, with basically no excimer emission detectable. Thus, no changes in shape were observed during the titration, but only a slight increase in the intensity of emission, due to the rigid conformation offered by the area between HA and PluSNPs.

Fluorescence lifetimes reported in Tab 4.3 were fitted with a bi-exponential decay. Even in the absence of nanoparticles in solution, the HA@PMA is characterized by the presence of two different lifetimes. The fluorescence lifetime of 19 ns can be attributed to be the fraction quenched by O_2 dissolved in solution; the longer component (125 ns) can be otherwise attributed to a fraction of molecules confined into the hydrophobic pockets of the HA and thus shielded from the diffusion of O_2.

Analysing the pre-exponential coefficient B indicating the relative population for each lifetime, it can be noticed that in absence of the PluSNPs the pre-exponential coefficient relative to the longer lifetime is 3 times the quenched population. Upon titration, both the short and the long lifetime PMA show a slight increase in their lifetimes, indicating that an interaction with a more rigid environment of PluSNPs is occurring. Also, despite the increase of both the values, the relative population of the unquenched molecules decreases, in accordance with the progressive unfolding of HA triggered by the interaction with nanoparticles.

Table 4.3. Fluorescence lifetimes for HA@PMA derivative with PluSNPs.

	τ / ns (λ_{em}= 420 nm)	B	χ^2
0 eq. NPs	τ_1 = 18.75 τ_2 = 124.83	B_1 = 219 B_2 = 709	0.952
1 eq. NPs	τ_1 = 24.82 τ_2 = 134.82	B_1 = 240 B_2 = 636	0.976
5 eq. NPs	τ_1 = 24.81 τ_2 = 150.35	B_1 = 263 B_2 = 573	0.987
10 eq. NPs	τ_1 = 34.56 τ_2 = 164.96	B_1 = 258 B_2 = 472	0.977
20 eq. NPs	τ_1 = 26.61 τ_2 = 168.68	B_1 = 276 B_2 = 430	0.981

4.4 Conclusions

In this chapter the derivatization of hyaluronic acid with pyrene derivatives was performed. Two moieties were chosen: aminopyrene and 1-methylaminopyrene. The amino functional group allowed to perform the congjugation *via* a simple reaction in water, exploiting EDC and sulfo-NHS agents that activated the carboxyl acid group of HA toward the formation of amide linkage.

The DoF of PA was too low to be determined, while a better functionalization was obtained in the case of PMA, probably because the latter has a one carbon long spacer that improves its reactivity lowering steric effects. Furthermore, the direct conjugation of the amino group to the π-system lowers the nucleophilicity of the nitrogen, while in the PMA, the –methyl spacer allows to overcome this issue.

Both the systems HA@PA and HA@PMA were characterized and their interaction with PluSNPs nanomaterials was investigated. Interestingly, despite the low DoF, theHA@PA system shows a variation of intensity of emission of the static excimer and monomeric forms.

On the other hand, the HA@PMA functionalization never shows the formation of excimers, but instead a very intense emission of monomer. Upon titration with nanomaterials its luminescence is subjected to a slight increase and also to a variation of the two lifetimes (related to a population quenched by the diffusion of oxygen and another one protected into the hydrophobic pockets of HA).

4.5 References

[1] S. K. Ghosh, A. Pal, S. Kundu, M. Mandal, S. Nath, and T. Pal, ‘Emission Behavior of 1-Methylaminopyrene in Aqueous Solution of Anionic Surfactants’, *Langmuir*, vol. 20, no. 13, pp. 5209–5213, Jun. 2004, doi: 10.1021/la035536n.

[2] E. J. Jun, H. N. Won, J. S. Kim, K.-H. Lee, and J. Yoon, ‘Unique blue shift due to the formation of static pyrene excimer: highly selective fluorescent chemosensor for Cu2+’, *Tetrahedron Letters*, vol. 47, no. 27, pp. 4577–4580, Jul. 2006, doi: 10.1016/j.tetlet.2006.04.143.

[3] H. Siu and J. Duhamel, ‘Molar Absorption Coefficient of Pyrene Aggregates in Water’, pp. 15301–15312, 2008.

[4] J. B. Birks, ‘Excimers’, *Rep. Prog. Phys.*, vol. 38, pp. 903–974, 1983.

[5] F. M. Winnik, ‘Photophysics of preassociated pyrenes in aqueous polymer solutions and in other organized media’, *Chem. Rev.*, vol. 93, no. 2, pp. 587–614, Mar. 1993, doi: 10.1021/cr00018a001.

[6] K. Kalyanasundaram and J. K. Thomas, ‘Solvent-dependent fluorescence of pyrene-3-carboxaldehyde and its applications in the estimation of polarity at micelle-water interfaces’, *J. Phys. Chem.*, vol. 81, no. 23, pp. 2176–2180, Nov. 1977, doi: 10.1021/j100538a008.

Chapter 5 - Derivatization of HA with ruthenium complexes

5.1 Introduction

Ruthenium polypyridyl complexes, such as $[Ru(bpy)_3]^{2+}$ and its derivatives are compounds widely investigated and commonly used in several fields, such as artificial photosynthesis [1], energy conversion [2], photovoltaic cells, and luminescent reporters. Also they have been exploited for their newly proved antitumor activity [3].

In these complexes, ruthenium(II) is bound to three bidentate ligands due to its d^6 low-spin valence.

Upon excitation, and because of spin-orbit coupling, a ^{3}MLCT charge transfer state is populated. This electronic state suffers from oxygen quenching but, its radiative decay to the ground state, being a phosphorescence phenomenon, occurs in the submicrosecond range also in aerated solutions.

Due to the interesting features of Ruthenium polypyridyl complexes, we used two of them, - cis-$[Ru(bpy)_2(L)]Cl_2$ and $[Ru(bpy)(L)(DPPZ)](PF_6)_2$ to derivatize hyaluronic acid and to investigate its interaction with nanomaterials.

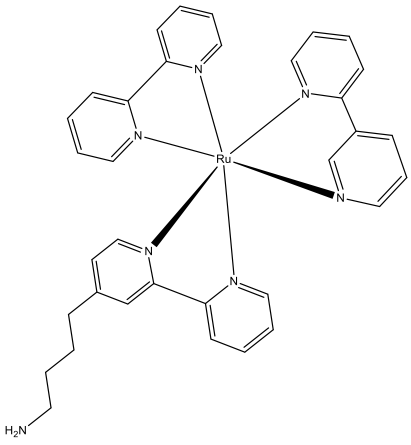

$[Ru(bpy)_2(L)]^{2+}$

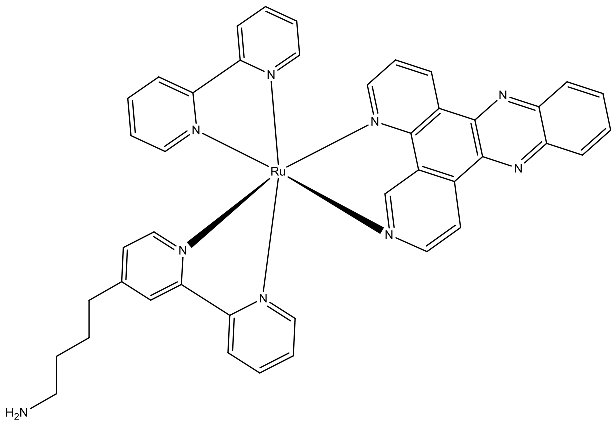

$[Ru(bpy)(L)(DPPZ)]^{2+}$

5.2 Materials and methods

Cis-$[Ru(bpy)_2(L)]Cl_2$ and $[Ru(bpy)(L)(DPPZ)](PF_6)_2$ were previously synthesised. N-(3-Dimethylaminopropyl)-N′-ethylcarbodiimide hydrochloride (EDC·HCl), N-Hydroxysulfosuccinimide sodium salt (sulfo-NHS), trimethylamine (TEA), ethylendiamin (EDA), Deoxyribonucleic acid sodium salt from salmon testes were purchased from Sigma Aldrich., Hyaluronic acid 300 KDa cosmetic grade were purchased from Stanfordchem, California, US.

Cellulose tube was purchased from Sigma, mol wt. Cut-off > 12 KDa, avg. 33 mm diameter. RC Durapore filters (0.45 micron pores dimension) were purchased from Millipore.

Hybrid DNA sequence was provided by the microbiology research group of Prof. M. Bonafè at Ospedale S. Orsola, Bologna.

DNA strand = 5'-GAC GAC ATG GAG AAA ATC TGG CAC CAC ACC TTC TAC AAT GAG CTG-3'

RNA sequence = 5'-CAG CUC AUU GUA GAA GGU GUG GUG CCAGAU UUU CUC CAU GUC GUC-3'

5.2.1 Functionalization of hyaluronic acid with cis-$[Ru(bpy)_2(L)]Cl_2$ or $[Ru(bpy)(L)(DPPZ)](PF_6)_2$

L= 4-(4’-methyl-[2,2’-bipyridin]-4-yl)butan-1-amine
bpy = 2,2’-bipyridine
DPPZ = dipyrido[3,2-a:2’,3’-c]phenazin

10 mg of HA were dissolved in 2 mL of phosphate buffer pH= 5.3. Sulfo-NHS (5 mg, 0.026 mmol, 5 eq.) and EDC (2.5 mg, 0.013 mmol, 2.5 eq.) each dissolved in 100 µL of phosphate buffer were added to HA solution. The acid environment slows down EDC hydrolysis. After 10 minutes, the dye molecule (3.78 mg, 0.005 mmol, 1 eq.), previously dissolved in 500 µL of a stock solution was added to HA solution and the pH was adjusted with NaOH 1 M until it became slightly basic (above pH= 7.5). 5 mM Stock solution of cis-$[Ru(bpy)_2(L)]Cl_2$ was PBS pH 7.4, while the stock solution of $[Ru(bpy)_2(DPPZ)](PF_6)_2$ was DMF. After 20 minutes, other 2.5 eq. of EDC have been added. The molar excess has been calculated in order to obtain a functionalization degree of 10% compared to the monomers present in the HA chain. The mixture was kept under magnetic stirring at room temperature for one night. The product was purified by dialysis against Milli-Q water for 48 h. The dialyzed solution was diluted to a total volume of 10 mL with Milli-Q water.

5.3 Results and discussion

5.3.1 Synthesis and characterization of HA@Ru derivatives

The functionalization of HA with the Ruthenium complexes is a two-step reaction. In order to slow down the hydrolysis of o-acylisourea intermediate, the first step was conducted in aqueous medium at slightly acidic pH (pH = 5.3). On the other hand, the proper amount of dye was introduced in the reaction mixture from a stock solution in a proper solvent, that is PBA at pH 7.4 for the cis-$[Ru(bpy)_2(L)]Cl_2$ or

DMF for $[Ru(bpy)(L)(DPPZ)](PF_6)_2$. Indeed, the DPPZ ligand is soluble in organic solvents and its solubilisation in a water miscible solvent improved the efficiency of the reaction.

The pH has been eventually adjusted above 7 with NaOH 1M in order to guarantee the deprotonation of the primary amine group of the dye molecule. In fact, unlike the other employed dyes, cis-$[Ru(bpy)_2(L)]Cl_2$ is soluble in water and for this reason the use of the surfactant was not necessary. Moreover, exploiting the high solubility of the dye in water, the purification step has been carried out by neutral dialysis against Milli-Q water.

5.3.2 Photochemical characterization

From the absorption spectra of $[Ru(bpy)_2(L)]Cl_2$ (Figure 5.1) the molar extinction coefficient (ε) of the complex was estimated. The calculated ε at $\lambda_{Ru(bpy)}$ = 453 nm, that is the wavelength of the maximum absorption of the MLCT band, is $\varepsilon_{Ru(bpy)}$ = 9930 $(M\ cm)^{-1}$.

A $[Ru(bpy)_3]^{2+}$ solution in water (Φ_r= 0.028 in aerated solution) has been used as reference compound to calculate the quantum yield of the HA derivative

The results are reported in Table 3. Figure 5.2 shows the absorption, emission and excitation spectra of the HA@$[Ru(bpy)_2(L)]Cl_2$ derivative.

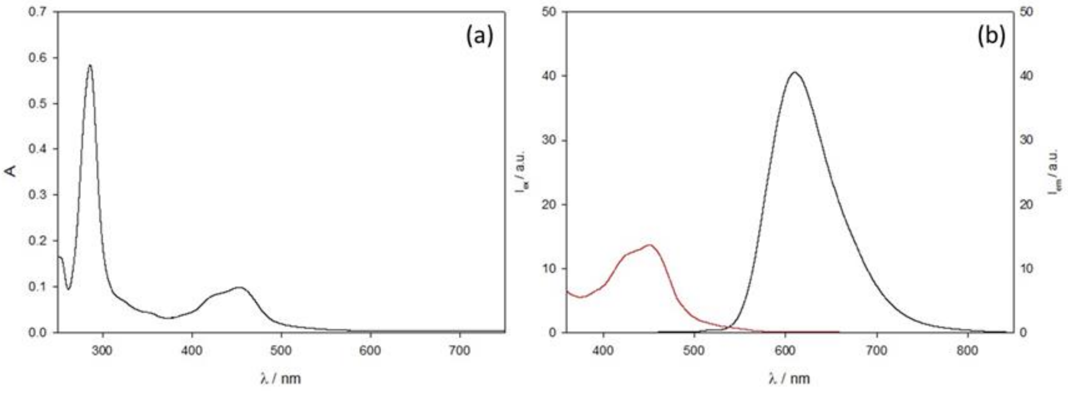

Figure 5.1. a) absorption, b) emission (black line, λ_{ex} = 440 nm) and excitation (red line, λ_{em} = 680 nm) spectra of $[Ru(bpy)_2(L)]Cl_2$.

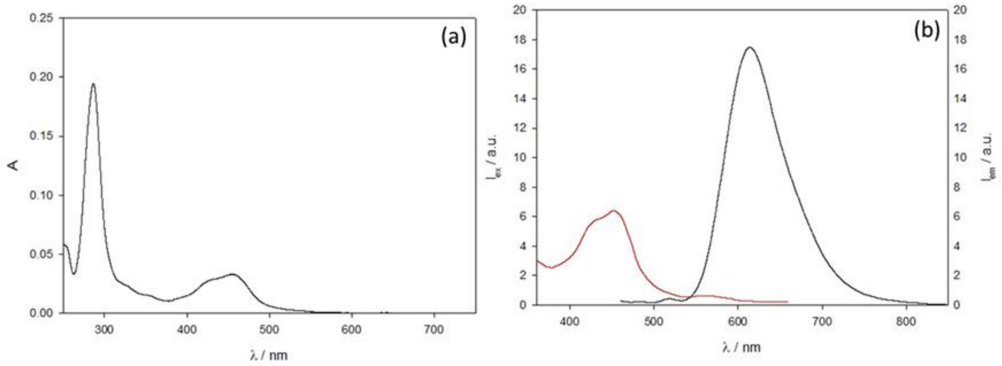

Figure 5.2. a) absorption, b) emission (black line, λ_{ex} = 440 nm) and excitation (red line, λ_{em} = 680 nm) spectra of HA-$[Ru(bpy)_2(L)]Cl_2$.

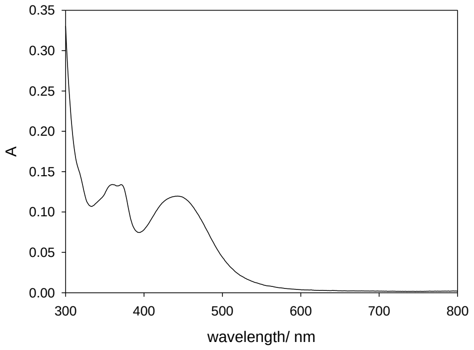

Figure5.3 absorption spectra of HA@$[Ru(bpy)(L)(DPPZ)](PF_6)$.

The wavelength of the maximum absorption of $[Ru(bpy)(L)(DPPZ)](PF_6)$ is 440 nm. From the spectrum of $[Ru(bpy)(L)(DPPZ)](PF_6)$ we obtained $\varepsilon_{440\ nm}$ =6900 $(M\ cm)^{-1}$. From this value we calculated the DoF of HA@Ru(DPPZ) as 6%.

Importantly, the DPPZ ligand quenches the fluorescence of the complex in water, thus also the HA derivative results completely quenched in aqueous media.

Table 5.1 Functionalization rate, number of dyes per HA filament and quantum yield value for HA@Ru derivatives.

	DoF (%)	**N° dyes/filament**	***Φ***
HA@Ru(Bpy)	8.0	64	0.03
H@Ru(DPPZ)	6.0	49	-

5.3.3 Interactions among HA-[Ru(bpy)$_2$(L)]Cl$_2$ and PluSNPs

Unlike the HA derivatives with organic dyes studied in the previous chapters, the titration of HA@Ru(bpy) with PluSNPs didn't show any evidence of the interaction between the two, as it can be seen from absorption, excitation and emission spectra in figure 5.3 and from lifetime measurements reported in Tab 5.2.

The photophysical data acquired during the titration of the HA-[Ru(bpy)$_2$(L)]Cl$_2$ derivative with nanoparticles did not provided any evidence of the interaction between the two systems. In fact, as shown from the absorption, emission and excitation spectra reported in Figure 5.4, no changes in photophysical properties of the fluorescent HA@Ru(bpy) have been recorded following the addition of an increasing amount of NPs. The ruthenium compound used has an excellent solubility in water solutions, thus, even in the absence of nanoparticles, it results quite bright. Even fluorescence lifetimes, reported in Table 10 show no significant changes during the titration.

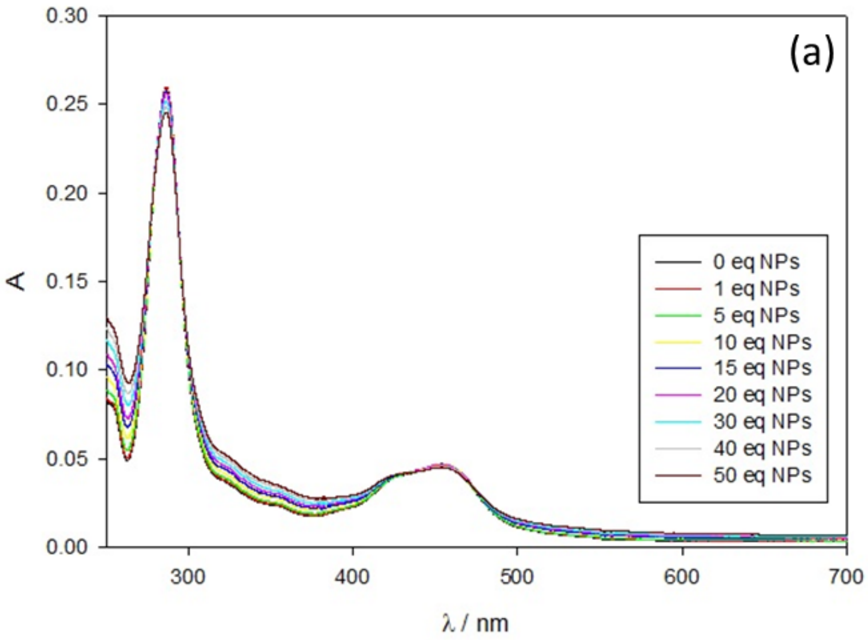

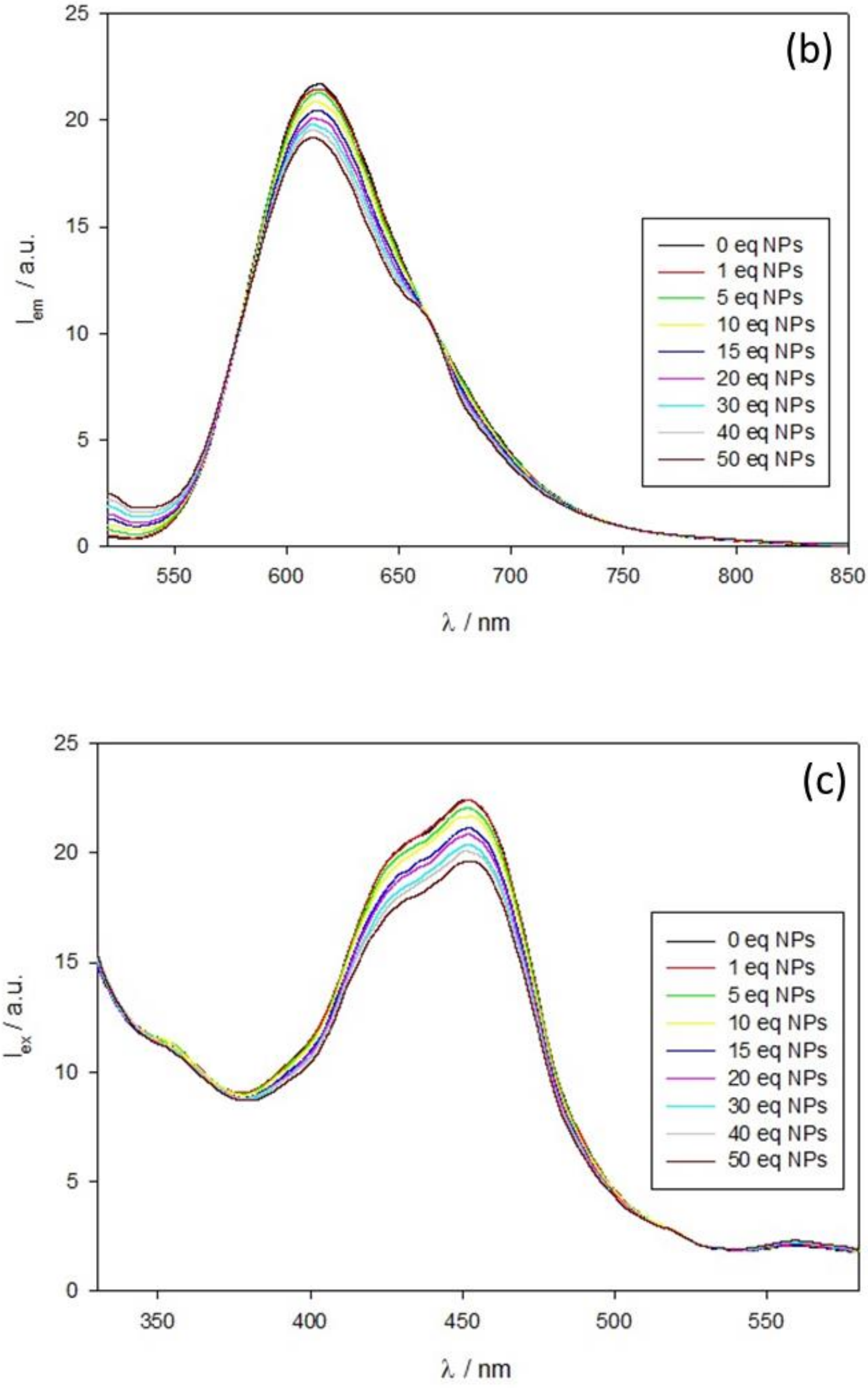

Figure 5.4. a) absorption, b) emission (λ_{ex} = 440 nm) and c) excitation (λ_{em} = 620 nm) spectra of HA-[Ru(bpy)$_2$(L)]Cl$_2$ following the addition of increasing amount of NPs.

Table 5.2. Fluorescence lifetimes for HA@Ru(bpy) derivative with NPs.

	τ / ns (λ_{em} = 620 nm)	χ^2
0 eq. NPs	378.8	0.912
1 eq. NPs	377.6	0.918
5 eq. NPs	377.8	1.000
10 eq. NPs	379.3	0.927
15 eq. NPs	374.9	0.932
20 eq. NPs	378.8	0.900
30 eq. NPs	366.6	0.885
40 eq. NPs	374.3	0.869
50 eq. NPs	371.9	0.934

In order to obtain some information about the interaction of HA with the PEGylated shell of the NPs, DLS measurements in PBS solution have been performed upon addition of PluSNPs. With this technique, it is possible to follow the changes in the population distribution of the derivatized polymer after the addition of the nanoparticles in solution. The size distributions recorded at different amounts of NPs are shown in Figure5.5, while in Table 5.3 the size of the distribution's picks and PDI values are reported.

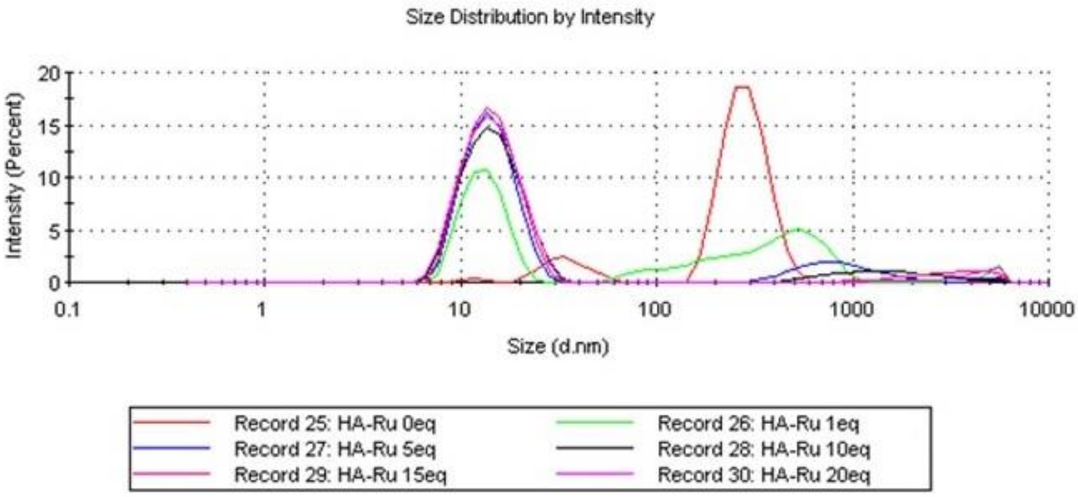

Figure 5.5. DLS diameter distributions at different amounts of NPs.

Table 5.3. Diameter distributions and PDI values.

	Size Peak 1 (d.nm)	**Size Peak 2 (d.nm)**	**PDI**
0 eq. NPs	35.17	288.0	0.637
1 eq. NPs	13.32	404.5	0.627
5 eq. NPs	14.38	916.7	0.315
10 eq. NPs	14.90	-	0.315
15 eq. NPs	14.68	-	0.236
20 eq. NPs	14.77	-	0.235

As shown from the figure and table above, PBS solutions of hyaluronic acid are characterized by the presence of two different populations, a bigger one with higher intensity and a smaller one, much less intense. It is however noteworthy to say that objects with bigger dimensions result amplified in the DLS technique, whose intensity is proportional to d^6 (d is the diameter of the nanostructure, see appendix A.7), and thus a quantitative analysis can be done only considering this dependence. Moreover, the analysis of the trend of polydispersity index (PDI) value can give additional information on the interactions between HA and PluSNPs.

By adding nanoparticles in solution, the two distributions change both in intensity and position. The bigger one decreases in intensity and moves to higher value of hydrodynamic diameters. On the other hand, the smaller distribution increases in intensity and shifts towards the PluSNPs hydrodynamic diameter value. Starting from 10-fold molar excess of PluSNPs, the bigger distribution disappears while the smaller one stabilizes around a diameter value of approximately 15 nm. Increasing the NP concentration, the sample decreases in PDI. This indicates that, despite no photophysical variation are observed upon the addition of PluSNPs, an interaction between HA and nanoparticles is occurring anyway. Thus, as previously seen for other HA derivatives, it seems that the bigger aggregates of HA disaggregate as the polymer starts to interact with the soft shell of silica nanoparticles. Indeed, the smaller size distribution arising from the interfacing of the two systems, shows a diameter very similar to that observed for PluSNPs in buffer solution.

5.3.4 Interactions between HA@[Ru(bpy)$_2$(L)]Cl$_2$ and salmon sperm DNA

After having proved that HA@Ru(bpy) can interact with reference nanomaterials (PluSNPs) through life time and dynamic light scattering measurements, we investigated the ability of HA@Ru(bpy) to detect DNA in solution. Indeed, fluorescent reporters for DNA based on metal complexes have already been studied due to the extremely biological interest of this nanomaterial.

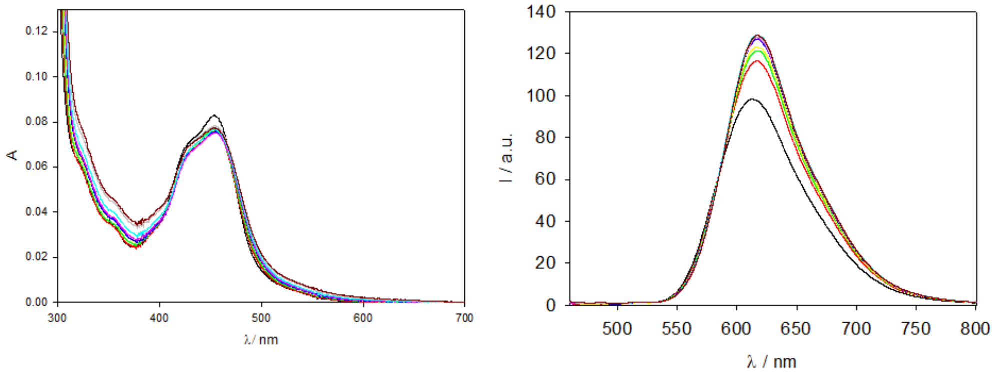

Figure 5.6: absorption (a) and emission (b) spectra of HA@[Ru(bpy)$_2$(L)]Cl$_2$ upon increasing concentration of salmon sperm DNA. [Ru] = 10 µM; [HA]$_{filament}$ = 0.2 µM

As shown by absorption and emission spectra reported in figure 5.6 b, an increase in the emission intensity accompanied by a small red-shift was recorded.

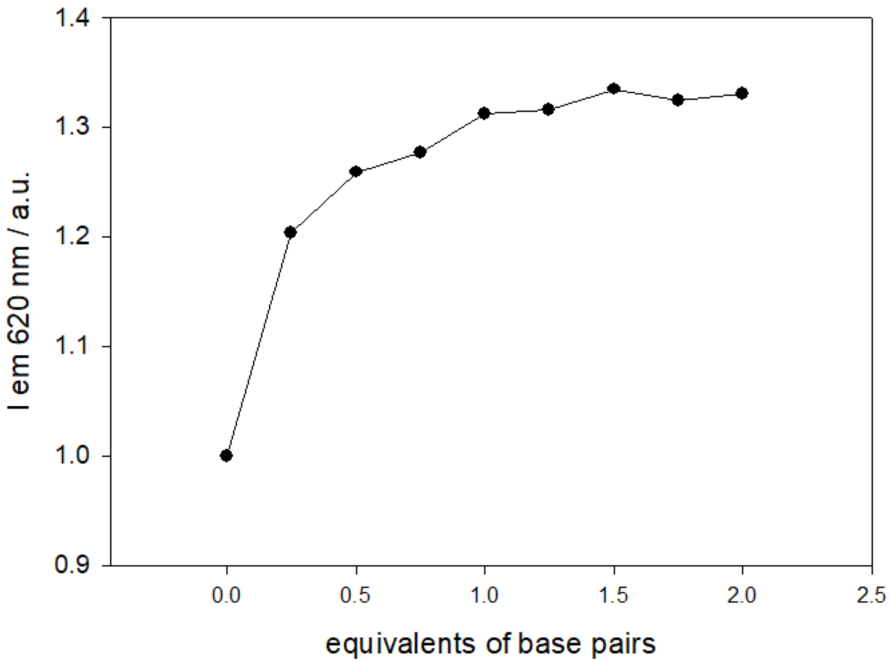

Figure 5.7trend of HA@[Ru(bpy)$_2$(L)]Cl$_2$ upon increasing concentration of salmon sperm DNA (λ_{exc} = 440 nm, λ_{em} = 620 nm).

Upon the addition of 1 equivalent of base pairs versus the ruthenium complex concentration, the emission undergoes a 30% fold increase.

Tab 5.4: lifetimes of HA@[Ru(bpy)2(L)] upon addition of DNA

bp DNA equivalents	***Life time(ns)***	***B***	χ^2
0 eq DNA	338		1.00
0.5 eq DNA	283 603	(B_1=412) (B_2=555)	0.91
1 eq DNA	250 607	(B_1=324) (B_2=631)	0.98
1.5 eq DNA	263 635	(B_1=327) (B_2=630)	0.95
2 eq DNA	241 630	(B_1=284) (B_2=690)	0.99

Simultaneously, also lifetime decay increased. Indeed, with no DNA in solution the decay was fitted properly by a mono-exponential lifetime that is the one expected for $Ru(bpy)_3^{2+}$ in water; when DNA is added to the HA@Ru(bpy) a bi-exponential lifetime decay is observed with the population of the longer lifetime increasing compared to the population of the shorter lifetime decreasing. This proves that the interaction between DNA and HA is protecting Ruthenium complex from the oxygen quenching. All these data clearly indicates that an interaction is occurring with a high affinity, in contrast to what observed for $Ru(bpy)_3^{2+}$ alone, whose properties are not altered by the presence of DNA.

5.3.5 Interactions between HA-[Ru(bpy) (L)(DPPZ)]$(PF_6)_2$ and salmon sperm DNA

As explained in the introduction of this chapter, DPPZ is a well-known ligand able to intercalate into the DNA double helices. Ruthenium complexes having DPPZ as ligand have already been investigated [4] and an increase on its luminescence, which is normally quenched in aqueous media, was recorded.

Relying on the literature data and on a good degree of functionalization (DoF) of the HA derivative, we performed titrations on HA@Ru(DPPZ) with commercial salmon sperm DNA. Absorption and emission spectra are reported in figure 5.8

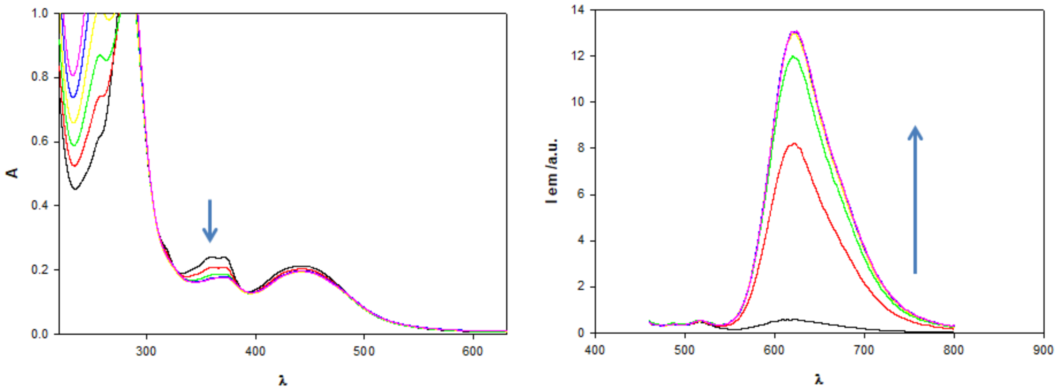

Figure 5.8: absorption (a) and emission (b) spectra of HA@[Ru(bpy) (L)(DPPZ)]$(PF_6)_2$ upon increasing concentration of salmon sperm DNA. [Ru] = 30 μM; $[HA]_{filament}$ = 0.6 μM

Despite only a slight variation in absorbance was observed, a huge increase in the emission of HA@[Ru(bpy)(L)(DPPZ)]$(PF_6)_2$ was recorded. The trend is reported below (figure 5.9). the equivalents are considered in terms of DNA base pair versus concentration of Ruthenium complex.

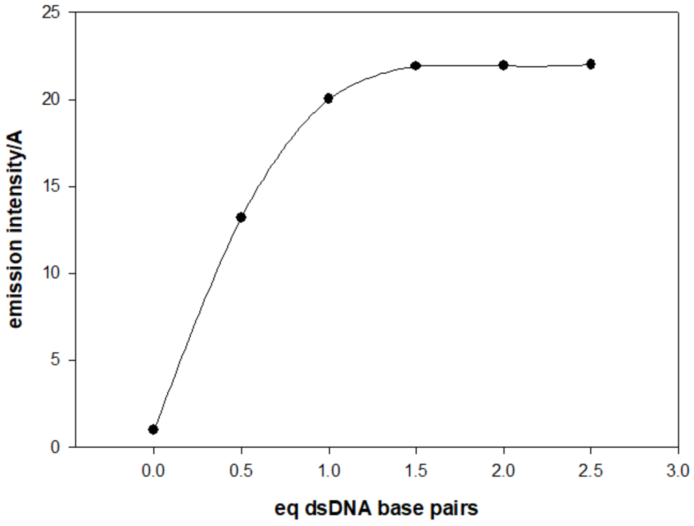

Figure 5.9: trend of the emission intensity of HA@[Ru(bpy) (L)(DPPZ)]$(PF_6)_2$ normalized and upon increasing concentration of salmon sperm DNA (λexc = 440 nm, λem = 620 nm).

Upon an addition of 30 μM of DNA base pairs (or 15 nM of $DNA_{filament}$) approximately a 20-fold increase in the emission is recorded.

This indicates that the affinity of DPPZ over DNA is high even when it is bound to the hyaluronic acid. Even in this system, as already stated before, its luminescence in water is completely quenched; on the other hand, upon interaction with DNA, the quenching operated by the interaction with the solvent is overcame by the DNA environment protecting the metal complex.

5.3.6 Interactions between HA-[Ru(bpy) (L)(DPPZ)]$(PF_6)_2$ and Hybrid DNA

The same titration was performed using hybrid DNA instead of salmon sperm DNA. Also in this case, an increase in the ruthenium complex emission is observed. Nonetheless, as shown in figure 5.11, upon the addition of 1 equivalent of hybrid base pairs, only a 6-fold increase is reached.

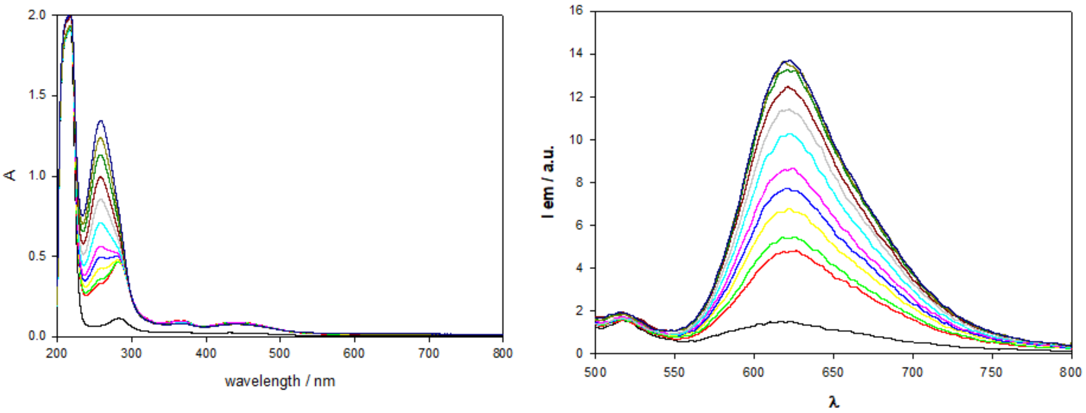

Figure 5.10: absorption (a) and emission (b) spectra of HA@[Ru(bpy)(L)(DPPZ)]$(PF_6)_2$ upon increasing concentration of Hybrid DNA. [Ru] = 10 µM; $[HA]_{filament}$ = 0.2 µM

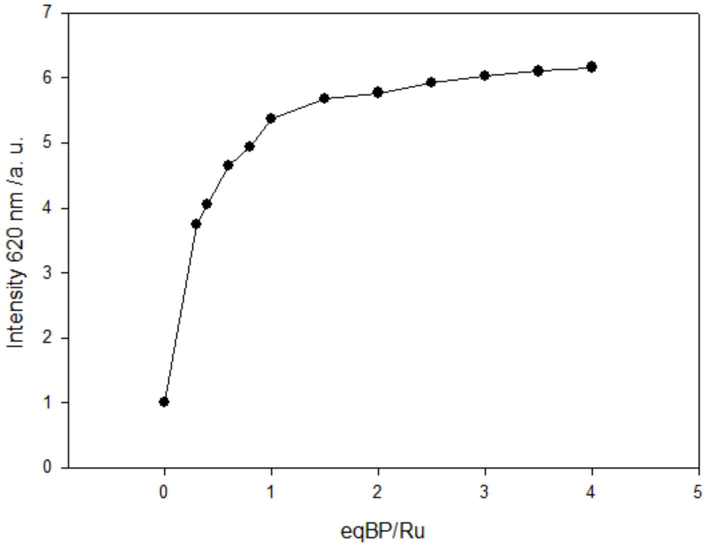

Figure 5.11: trend of the emission intensity of HA@[Ru(bpy)(L)(DPPZ)]$(PF_6)_2$ upon increasing concentration of salmon sperm DNA (λexc = 440 nm, λem = 620 nm).

It is worthy to note that the salmon sperm DNA is a 2000 base pair sequence long DNA, while hybrid DNA here used is only 45 base pairs long. The better result obtained for the titration with salmon sperm can thus be due to the fact that longer DNA sequence interacts with HA derivative more favourably than a much shorter sequence as the hybrid one.

5.4 Conclusions

In this chapter we efficiently synthesised new derivatives of HA with ruthenium bipyridine complexes. The first one is highly soluble in water and it maintains its properties also when bound to hyaluronic acid, with a degree of functionalization of 8%. We then investigated HA@Ru(bpy) interactions with nanomaterials: as already done for other HA derivatives, PluSNPs were firstly used as reference nanomaterials. Despite the photophysical properties of HA@Ru(bpy) did not change upon addition of nanoparticles (nor the luminescence intensity or the lifetime), an interaction between HA@Ru(bpy) and PluSNPs can still be detected by dynamic light scattering analysis. Upon increasing the concentration of the nanomaterials, the bigger size peak related to HA fold in solution decreases and it is progressively visible only a peak having the same dimensions of PluSNPs in buffer solution.

Moreover, the interaction between HA@Ru(bpy) and double strand DNA were studied. Interestingly a slight increase in the luminescence intensity of the complex was detected upon addition of DNA and also lifetime decay increased. Indeed, a bi exponential life time decay is observed when DNA is added to the HA@Ru(bpy); the population related to the longer lifetime increased, while a concomitant decrease of the population having the shorter lifetime decreased. This indicates that the interaction between DNA and HA is protecting Ruthenium complex from the oxygen quenching.

The second complex studied has a DPPZ ligand, which drastically decreases the complex solubility in aqueous media and also its luminescence is completely quenched in this environment.

On the other hand, the DPPZ is a known intercalator for DNA, so we investigated the HA@Ru(DPPZ) interaction with two different DNA: a salmon sperm double strand DNA (dsDNA) having a sequence of 2000 base pairs and ha hybrid DNA having a sequence of 45 base pairs.

It turned out that the HA@Ru(DPPZ) is sensitive both toward a dsDNA and toward a hybrid DNA since its luminescence increases in both cases. On the other hand, adding one equivalent of base pairs (bp) versus Ruthenium causes a 20-fold increase in the case of dsDNA and only a 6 fold increase for the hybrid DNA. This difference could be explained considering that when a 300 KDa HA is interacting with DNA of different length. The salmon sperm dsDNA is a 2000 base pair sequence while the hybrid is only a 45 base pair long sequence. Thus, since the equivalents of base pairs are compared, this means that in the titration with dsDNA less filaments are added compared to the hybrid DNA and probably the addition of a lower concentration of DNA filaments ensure a more favourable interaction with HA.

5.5 References

[1] M. Sykora, K. A. Maxwell, J. M. DeSimone, and T. J. Meyer, ‘Mimicking the antenna-electron transfer properties of photosynthesis’, *Proceedings of the National Academy of Sciences*, vol. 97, no. 14, pp. 7687–7691, Jul. 2000, doi: 10.1073/pnas.97.14.7687.

[2] P. Wang, S. M. Zakeeruddin, J. E. Moser, M. K. Nazeeruddin, T. Sekiguchi, and M. Grätzel, ‘A stable quasi-solid-state dye-sensitized solar cell with an amphiphilic ruthenium sensitizer and polymer gel electrolyte’, *Nature Mater*, vol. 2, no. 6, pp. 402–407, Jun. 2003, doi: 10.1038/nmat904.

[3] A. Rilak Simović, R. Masnikosa, I. Bratsos, and E. Alessio, ‘Chemistry and reactivity of ruthenium(II) complexes: DNA/protein binding mode and anticancer activity are related to the complex structure’, *Coordination Chemistry Reviews*, vol. 398, p. 113011, Nov. 2019, doi: 10.1016/j.ccr.2019.07.008.

[4] F. Jia, S. Wang, Y. Man, P. Kumar, and B. Liu, ‘Recent Developments in the Interactions of Classic Intercalated Ruthenium Compounds: [Ru(bpy)2dppz]2+ and [Ru(phen)2dppz]2+ with a DNA Molecule’, *Molecules*, vol. 24, no. 4, p. 769, Feb. 2019, doi: 10.3390/molecules24040769.

PART C

Sensors for the detection of emerging pollutants

Chapter 6 – Supramolecular systems for BPA detection

6.1 Introduction

Emerging Pollutants (EP) represent a heterogeneous class of contaminants found in surface, ground or drinking water. During the last decades several newly discovered pollutants were found in water at concentration between ng/L and several µg/L, thus generating an increasing concern about them [1].

Emerging pollutants cover different families of natural or anthropogenic substances, such as pesticides, antibiotics, anti-inflammatory drugs, personal care products, plastics, mostly derived from industrial wastewater, domestic effluents or agriculture waste

The great concern about emerging pollutants arises from their proved hazardous effects on environmental, human and wildlife health.

For example, a huge amount of EPs are constituted by pharmaceutical and personal care products (PPCPs), rapidly degraded and dissipated in the environment but characterised by a pseudo-persistence in water. As a consequence, bioaccumulation in aquatic animals leads to some harmful effects on them, as reported by Gunarsson et al [2], who found enlargement of fish livers upon chronic exposure to estrogenic contaminants in water.

Amongst the heterogeneous and growing classes of emerging pollutants, the interest toward Bisphenol A (BPA) has recently begun to arise. It is indeed widely used as plasticizer in the production of polycarbonates, epoxy resins and paper for several applications including packaging materials, food contact materials, or toys [3], [4]. Due to its widespread presence in human manufacturing products, it has been intensively introduced into the environment in the last years, leading to a chronic exposure of humans and animals. This prolonged exposure has proved to be harmful due to BPA endocrine disruptor properties [5]. Moreover, BPA is supposed to affect the development of cancer, cardiovascular and hepatic diseases.

Despite several systems involving the use of metal nanoparticles or molecular imprinted polymers are already under investigation as suitable probes for BPA detection [6], [7], very few examples of supramolecular approaches are available in literature.

This chapter will thus focus on two probes for BPA detection: the former is based on the formation of a supramolecular structure based on a metal complex designed in order to bind the target; the second one is instead based on the modulation of a previously studied interaction between dye doped silica nanoparticles and hyaluronic acid.

6.2 BPA detection through metal complex

6.2.1 Experimental section

$[Ru(phen)_2L_a]Cl_2 \cdot 6HCl$ was obtained from the group of Prof. Andrea Bencini at University of Florence and BPA was purchased from Sigma Aldrich.

Coordination of $[Ru(phen)_2L_a]Cl_2 \cdot 6HCl$ with Zn(II) ions.

Four equivalents of a $Zn(NO_3)_2$ solution in MilliQ water were slowly added to $[Ru(phen)_2L_a]Cl_2 \cdot 6HCl$ water solution using a syringe pump system. The pH of the final solution was adjusted to 7.4 and the solution was kept under magnetic stirring over night before further measurements.

Photophysical measurements

Absorption spectra were recorded using a double beam spectrophotometer UV/Vis Perkin Elmer Lambda-45 in the 300-800 nm range. The registration of the emission and excitation spectra was performer using a spectrofluorimeter Perkin Elmer LS55. Excited state lifetime measurements were performed using a spectrofluorimeter Edinburgh Analytical Instruments FLS920, equipped with a time-correlated single-photon counting device. Measurements were performed using a total concentration of $\{Zn[Ru(phen)_2)H_2\mathbf{L}]\}^{6+}$ of 2 x 10^{-5} mol/dm^3. The concentration of BPA was varied between 0 and 2 x 10^{-4} mol/dm^3.

6.2.2 Results and discussion

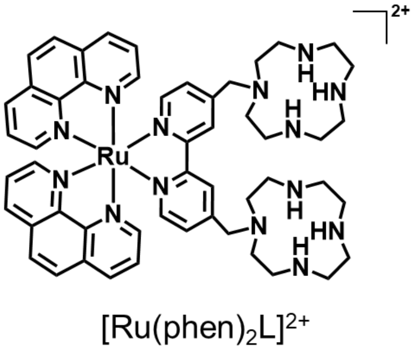

Figure 6. 1: Chemical structure of [Ru(phen)2 La]]$^{2+}$

The idea of detecting the presence of BPA in aqueous solution forming a supramolecular host-guest adduct between BPA and a metal complex could be exploited considering that BPA is an aromatic moiety having two phenolic –OH groups. Therefore, not only hydrophobic and π-stacking interactions could be exploited but also BPA hydrogen bonding capability.

Nonetheless, these interactions would be too weak to create a stable adduct. To overcome this problem, two 1,4,7,10-tetraazacyclododecane (cyclen) units were linked to a $Ru^{II}(phen)_2(bipy)$ core.

The cyclen substituents can coordinate transition metals. In particular, Zn^{II} was chosen because it can expand its coordination sphere, allowing further bonds although already coordinated by the macrocycles.

To verify the effective ability of the Zn^{II} complexes with $[Ru(phen)_2)\mathbf{L_a}]^{2+}$ to bind BPA, a speciation study was performed on the complexes formed by $[Ru(phen)_2)\mathbf{L_a}]^{2+}$ with Zn^{II}, in order to determine the potential ternary complexes formed with BPA and their stability constants in aqueous solution.

Since the metal coordination in water competes with the ligand protonation, the protonation constants of $[Ru(phen)_2\mathbf{L_a}]^{2+}$ were determined. Results are reported in Table 6.1. Figure 6.2 reports the distribution diagrams of the protonated forms of **L** at different pH values.

Table 6.1. Protonation constant of $[Ru(phen)_2\mathbf{L_a}]^{2+}$ in NaCl 0.1 M aqueous solution and 298 K.

Equilibria	LogK
$[Ru(phen)_2L_a]^{2+} + H^+ = [Ru(phen)_2(H\ L_a)]^{3+}$	11.02
$[Ru(phen)_2(H\ L_a]^{3+} + H^+ = [Ru(phen)_2(H_2\ L_a)]^{4+}$	10.15
$[Ru(phen)_2(H_2\ L_a)]^{4+} + H^+ = [Ru(phen)_2(H_3\ L_a)]^{5+}$	8.53
$[Ru(phen)_2(H_3\ L_a)]^{5+} + H^+ = [Ru(phen)_2(H_4\ L_a)]^{6+}$	7.59
$[Ru(phen)_2(H_4\ L_a)]^{6+} + 2H^+ = [Ru(phen)_2(H_6\ L_a)]^{8+}$	7.01
	pK_a
$BPA = BPA(H_{-1})^- + H^+$	8.4
$BPA(H_{-1})^- = BPA(H_{-2})^{2-} + H^+$	10.9

The basicity of $[Ru(phen)_2\mathbf{L_a}]^{2+}$ is consistent with the presence of two cyclen moieties within its framework. Indeed the first two protonation constant are slightly lower than the first found in literature for cyclen(log K =11.27) [46]. Moreover, the values very similar to each other indicates that each H^+ is located on two different macrocyles in $[Ru(phen)_2(H_2\mathbf{L})]^{4+}$. Similarly, a third and fourth protonation constant are found to be similar to each other and slightly lower than the second protonation constant of the cyclen (log K = 9.8). The $[Ru(phen)_2(H_4\mathbf{L})]^{6+}$ cation formed is the most abundant species at neutral pH, as shown in figure 6.2. Then, the binding of two further H^+ is found only at very acidic pH (Figure 6.2.3) and only the simultaneous constant for the addition of two H^+ ions to the $[Ru(phen)_2(H_4\mathbf{L})]^{6+}$ can be determined, as generally observed when two protonation equilibria occur in very similar pH regions (Tab 6.1)

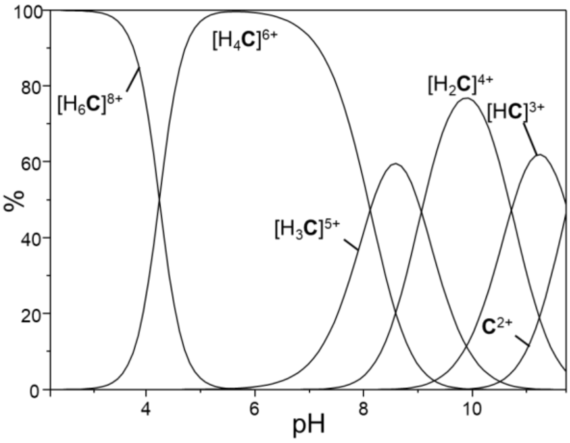

Figure 6.2: Distribution diagram of the protonated species of complex $[Ru(phen)_2\mathbf{L_a}]^{2+}$ (the $[Ru(phen)_2\mathbf{L_a}]$ unit is indicated with **C**).

Furtemore, the pK_as determined for BPA in our experimental condition are in good agreement with those reported in the literature (table 6.1).

Thus 2 equivalents of Zn^{II} were coordinated to the $Ru^{II}(phen)_2(bipy)$, obtaining a complex with two metal centres set at a fixed distance. Indeed, as shown in table 6.2 $[Ru(phen)_2\ \mathbf{L_a}]^{2+}$ forms stable mono- and binuclear complexes in aqueous solution. Once 1 equivalent of Zn^{II} is added, a stable $\{Zn[Ru(phen)_2\ \mathbf{L_a}]\}^{4+}$ is formed. It shows a marked tendency to bind up to two H^+ ions, as demonstrated by the protonation constants higher than 7 log units. These results are consistent with the presence of two cycle not bound to the metal centre, which are able to bind either a H^+ or a second Zn^{II}. Therefore, upon addition of 1 equivalent of Zn^{II} the mono and bi-protonated species $\{Zn[Ru(phen)_2(H\ \mathbf{L_a})]\}^{5+}$ and $\{Zn[Ru(phen)_2(H_2\ \mathbf{L_a})]\}^{6+}$ are the most abundant species from acidic to alkaline pH values (Figure 6.2.4 a); on the other hand, upon addition of 2 equivalents of Zn^{II}, dinuclear species are formed from neutral to alkaline pH values (Figure 6.3 b).

Furthermore, it was found out that when $\{Zn_2[Ru(phen)_2\ \mathbf{L_a}]\}^{6+}$ complex is formed at neutral pH values, Zn^{II} is not saturated by the coordination with the ligands, but it also binds water molecules with a marked tendency to give hydroxylated species (Figure 6.2.4 b). Also, the formation of a stable $\{Zn_2[Ru(phen)_2\ \mathbf{L_a}](OH)_3\}^{3+}$ is actually observed at slightly alkaline pH values., with only the simultaneous association constant of $3OH^-$ being observed, as happens for processes taking place in the same pH region.

Table 6.2. Formation constants of the Zn^{II} complexes with $[Ru(phen)_2\ \mathbf{L_a}]^{2+}$ and of their adducts with deprotonated BPA (indicated with $BPA(H_{-2})$). Errors are shown in parentheses

Equilibria	LogK*
$[Ru(phen)_2\ \mathbf{L_a}]^{2+} + Zn^{2+} = \{Zn[Ru(phen)_2\ \mathbf{L_a}]\}^{4+}$	14.75 (5)
$\{Zn[Ru(phen)_2\ \mathbf{L_a}]\}^{4+} + H^+ = \{Zn[Ru(phen)_2(H\ \mathbf{L_a}\ ]\}^{5+}$	8.68 (3)
$\{Zn[Ru(phen)_2(H\ \mathbf{L_a}\ ]\}^{5+} + H^+ = \{Zn[Ru(phen)_2(H_2\ \mathbf{L_a})]\}^{6+}$	7.15 (6)
$\{Zn[Ru(phen)_2\ \mathbf{L_a}]\}^{4+} + Zn^{2+} = \{Zn_2[Ru(phen)_2\ \mathbf{L_a}]\}^{6+}$	6.46 (3)
$\{Zn_2[Ru(phen)_2\ \mathbf{L_a}]\}^{6+} + 3OH^- = \{Zn_2[Ru(phen)_2\ \mathbf{L_a}\ (OH)_3]\}^{3+}$	15.61 (7)
$\{Zn_2[Ru(phen)_2\ \mathbf{L_a}]\}^{6+} + BPA^{2-} = \{Zn_2[Ru(phen)_2\ \mathbf{L_a}]BPA(H_{-2})\}^{4+}$	7.78 (5)
$\{[Zn_2[Ru(phen)_2\ \mathbf{L_a}]BPA\}^{4+} + OH^- = [Zn_2[Ru(phen)_2\ \mathbf{L_a}]BPA(H_{-2})(OH)\}^{3+}$	5.5 (4)
$\{Zn_2[Ru(phen)_2\ \mathbf{L_a}]BPA(OH)\}^{3+} + OH^- = [Zn_2[Ru(phen)_2\ \mathbf{L_a}]BPA(H_{-2})(OH)_2\}^{2+}$	3.83 (5)

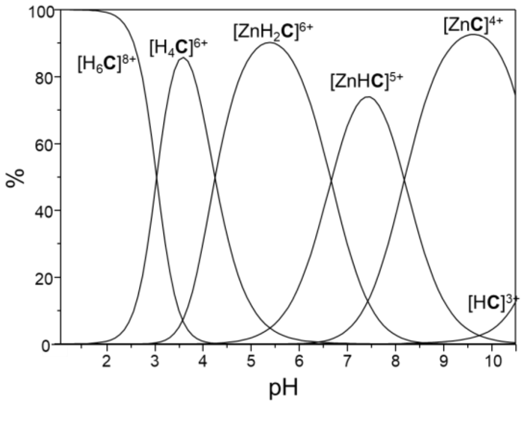

a)

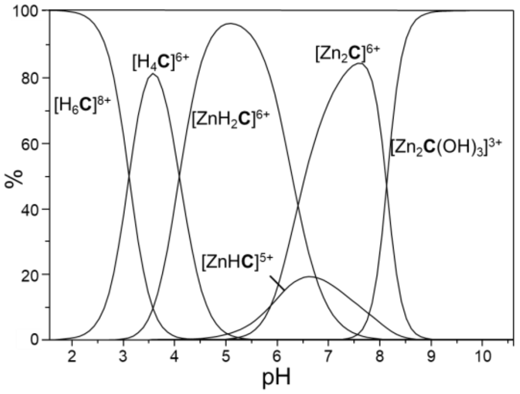

b)

Figure 6.3. Distribution diagrams of the complexes formed by the $[Ru(phen)_2\ \mathbf{L_a}]^{2+}$ (the $[Ru(phen)_2\ \mathbf{L_a}]$ unit is indicated **C** for clarity) with Zn^{II} in 1:1 (a) and 1:2 molar ratio (b) ($[Ru(phen)_2\ \mathbf{L_a}]^{2+} = 1{\cdot}10^{-3}$ M).

The dizinc complex is thus suitable to bind BPA its dianionic form at neutral pH, as shown by the distribution diagram in Figure 6.4. In the alkaline pH region, the formation of hydroxylated ternary complexes, still containing the $BPA(H_{-2})^{2-}$ is also observed. Interestingly enough, potentiometric measurements showed that nor the complex in the absence of Zn^{II} nor the mono-zinc complex can bind BPA. at any pH value. Indeed, in both cases, the coordination of BPA with the complex would involve at least one H-bond interaction between the phenolic –OH and the amino group in the cyclen, or the coordination of BPA to a single Zn^{II}. Apparently, none of these possible interactions are strong enough to form a stable adduct.

Instead, the presence of two spaced metal cations, able to simultaneously interact with the two phenolic functions of the substrates, is the necessary requirement to obtain double deprotonation of BPA and its coordination to the dizinc receptor.

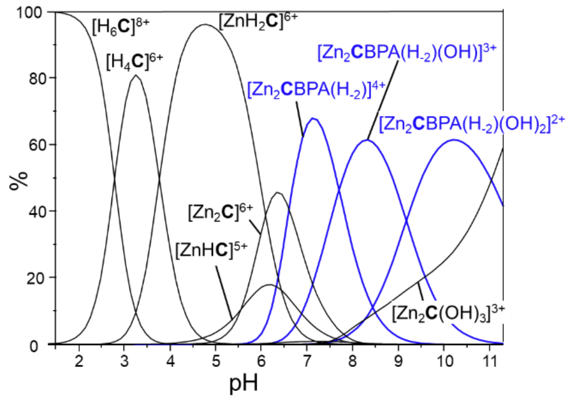

a)

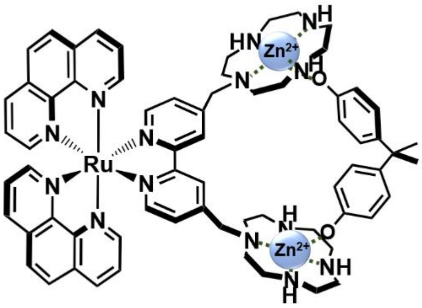

b)

Figure 6.4 Distribution diagrams of the complexes formed by the [Ru(phen)$_2$) **L$_a$**]$^{2+}$ (the [Ru(phen)$_2$) **L$_a$**] group is indicated with **C** for clarity) with Zn^{II} and BPA 1:2:1 molar ratio ([Ru(phen)$_2$)**L$_a$**]$^{2+}$ = $1 \cdot 10^{-3}$ M) (a) and proposed structure of the BPA adduct with the dizinc complex (b).

Photophysical measurements

[Ru(phen)$_2$**L$_a$**]$^{2+}$ shows in water solution the characteristic absorption and luminescence properties expected for polypyridine Ru complexes (figure 6.5).

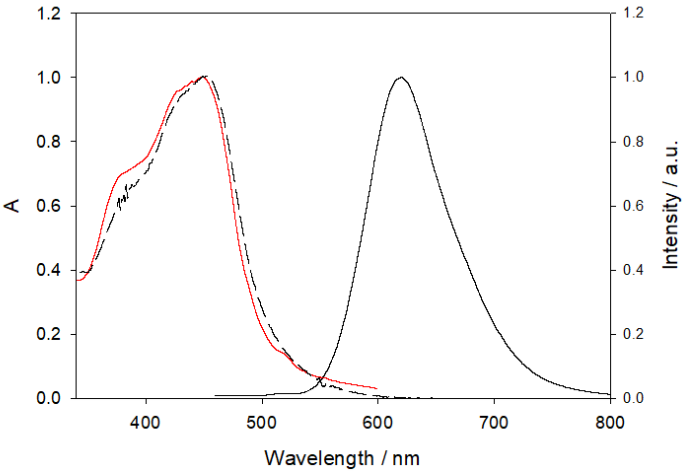

Figure 6.5 normalised absorption (black dashed line), emission (black line) and excitation (red line) spectra of [Ru(phen)$_2$ **L$_a$**]$^{2+}$.

In particular, [Ru(phen)$_2$ **L$_a$**]$^{2+}$ presents an absorption band in the visible region with maximum at 450 nm (ε = 11100 M^{-1} cm^{-1}) and an emission band in aerated solution with maximum at 620 nm, a luminescence quantum yield of 0.027, and an excited state lifetime of 460 ns; as expected, the corrected excitation spectrum is proportional to the absorption one in all the spectral range (220-560 nm). It is to note that all the photophysical properties are almost constant in a wide pH range (3 – 9). Thus, the spectra clearly demonstrate that the amines present in the two cyclen units are not able to quench the luminescence of the Ru complex, in agreement with what observed, for example, in Ru complexes with the 4-dimethylamino-2,2'bipyridine ligand ([9]). In this context, the addition of two equivalents of Zn^{II} ion at pH 7.4 does not cause noticeable intensity changes, indicating a negligible electronic effect on the bpy ligand caused by complexation that leads to the formation of {Zn$_2$[Ru(phen)$_2$**L$_a$**]}$^{6+}$.

On the contrary, the addition of an increasing amount of BPA to the system containing [Ru(phen)$_2$)**L$_a$**]$^{2+}$ at a concentration of 20 μM with Zn^{II} in a 1:2 stoichiometric ratio caused a quenching on the luminescence intensity of the Ru complex as it can be seen in figure 6.6. This intensity decrease is not accompanied by a concomitant change in the excited state lifetime, ruling out the contribution from a dynamic quenching mechanism, and in agreement with the formation of a stable adduct indicated by the speciation study discussed above.

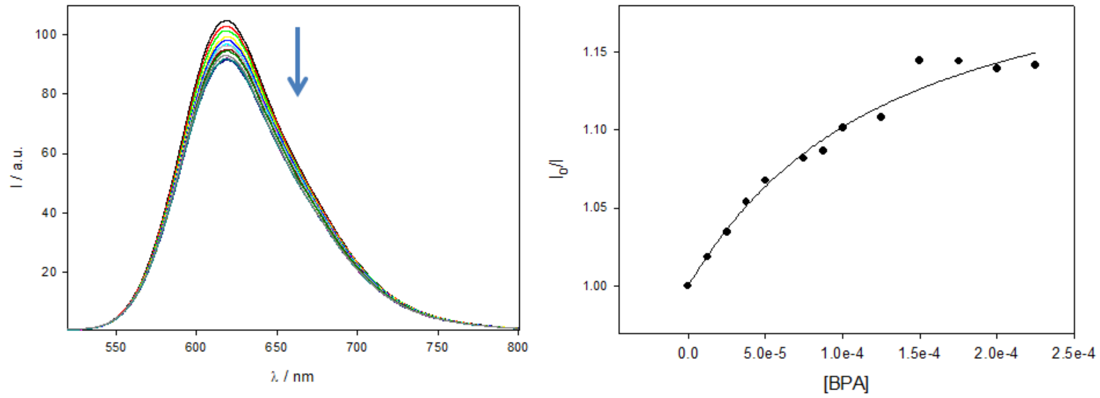

Figure 6.6 left: emission intensities of {Zn [Ru(phen)$_2$) **L$_a$**]}$^{6+}$ upon increasing concentration of BPA in water at pH = 7.4; right: ratio of luminescence intensity of the dizinc complex without BPA and luminescence internsity upon increasing concentration of BPA (black dots,λ_{exc} = 440 nm; λ_{em} = 620 nm) and fitting curve obtained using equation 6.2.1 (black line). [Ru(phen)$_2$) **L$_a$**]$^{2+}$ complex concentration of 20 μM with Zn^{II} in a 1:2 stoichiometric ratio

The equation 6.1 reported below was used to fit the I$_0$/I *vs* BPA concentration.

$$\frac{I_0}{I} = \frac{[Ru]_t}{\left\{[Ru]_t - [BPA]_t - \frac{1}{K_a} + \sqrt{([Ru]_t + [BPA]_t + 1/K_a)^2 - 4[Ru]_t \times [BPA]_t}\right\}/2} \qquad \text{Eq. 6.1}$$

Where $[Ru]_t$is the initial (total) concentration of $[Ru(phen)_2\mathbf{L_a}]^{2+}$; $[BPA]_t$ is the total concentration of BPA; and K_a the apparent association constant $[Ru(phen)_2\mathbf{L_a}]^{2+}$ and BPA. This equation is valid for static quenching with a 1:1 association fin case of the complete quenching of the luminophore.

In conclusion, despite the observed emission intensity changes suffer from a limited overall quenching even when BPA is in an equimolar amount respect to $[Ru(phen)_2\mathbf{L_a}]^{2+}$, the quenching detected demonstrated that this strategy can be promising for the detection of BPA even at lower concentrations, and the data reported here can be used to improve the design of the metal complex reporter.

6.3 BPA detection with nanomaterials

6.3.1 Experimental section

BPA was purchased from Sigma Aldrich. Hyaluronic acid 300 KDa cosmetic grade were purchased from Stanfordchem, California, US. Tetraethyl orthosilicate (TEOS, 99.9%), Trimethylsilyl chloride (TMSCl 99%), dimethylformamide (DMF 99.8%), Rhodamine B isothiocyanate mixed isomers (98%) (RITC), were purchased from Sigma AldrichDEAC-Si(OEt)$_3$,

PluSNPs@DEAC synthesis The synthesis of PluSNPs was performed according to the procedure already published in literature[23].
200 mg of PLURONIC F-127, 38 mg of NaCl were solubilized in 3.1 mL of acetic acid 1M. after a complete solubilisation, 360 µL of TEOS were added to the mixture at RT. The desired amount of the triethoxysilane derivative of DEAC (4 µmol, 0.5 % vs moles of TEOS, prepared according to literature [10]) were carefully solubilized with 300 µL of DMF and then added to the reaction mixture. The reaction was carried out under magnetic stirring for 2 hours and then 20 µL of TMSCl were

added. After 20 hours, PluSNPs were purified *via* dialysis versus MilliQ water for three days. The sample was finally diluted to 10 mL of MilliQ water, obtaining a 20 µM solution.

HA@RB synthesis: in a typical preparation, according to literature procedure [11], 30 mg of hyaluronic acid 193 ± 2 KDa (0.26 µmol) were dispersed in 8 ml of DMSO in a scintillation vial and 4.5 mg of Rhodamine B isothiocyanate (8.4 µmol) were successively added under magnetic stirring. The reaction was left to proceed for 24 h at room temperature. The resulting dispersion was diluted with 13 ml of deionized water and dialyzed against water for at least three days.

Photophysical measurements

Absorption spectra were recorded using a double beam spectrophometer UV/Vis Perkin Elmer Lambda-45 in the 300-800 nm range. The registration of the emission and excitation spectra was performer using a spectrofluorimeter Perkin Elmer LS55. Excited state lifetime measurements were performed using a spectrofluorimeter Edinburgh Analytical Instruments FLS920, equipped with a time-correlated single-photon counting device. Measurements were performed using a total concentration of HA@RB and PluSNPs@DEAC of 1,26 x 10^{-7} mol/dm^3. The concentration of BPA was varied between 0 and 6.5 x 10^{-4} mol/dm^3.

6.3.2 Results and discussion

In part B of this thesis, we already investigated the interaction between PluSNPs and HA derivatized with several dyes. Moreover, the interaction between PluSNPs and HA@RB was already reported in literature and explained in the introduction (Section 1.4.1)[11]. Here, we exploited the property of hyaluronic acid and Pluronic nanoparticles to self-assemble in aqueous solution through weak interaction between the polymeric arms of nanoparticles and the hydrophobic regions of HA. These interactions lead to the unfolding of HA and to the formation of a layer of HA surrounding the PluSNPs, as pointed out by the increase of rhodamine quantum yield; indeed, compared to the quantum yield of the HA@RB in water solution, dye is less subjected to the self-quenching process usually observed in some HA regions characterized by high local concentration of the dye itself.

BPA is an aromatic compound having greater affinity for non-polar environments rather than for aqueous ones, thus not only the hydrophobic regions of PluSNPs, but also the hydrophobic pockets of HA@RB could be exploited for BPA detection due to their ability to form weak hydrophobic interactions with the target molecule.

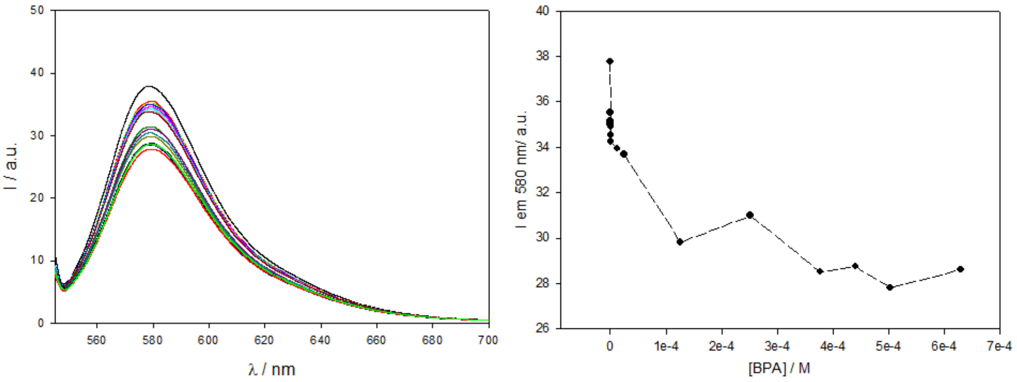

Figure 6.7: left: luminescence intensity of HA@RB upon addition of increasing concentration of BPA in water solution; right: luminescence intensity at 580 nm (maximum of RB emission peak). λ_{exc}= 530 nm; $\lambda_{em\ max}$ = 580 nm. [HA@RB] = $1x10^{-7}$ M.

Figure 6.7 shows the titration of BPA using HA@RB as probe considering a very fast equilibration time. In this condition, a sub-micromolar concentration of HA@RB is able to detect concentration of BPA ranging from = $1.26x10^{-7}$ M to = $1x10^{-4}$ M, after which the signal of rhodamine remains almost constant.

Despite these results show that the derivatized HA has a high affinity towards BPA, the obtained trend is fluctuating, probably because of a kinetic component requiring some time to equilibrate the HA@RB system at the working concentration.

Therefore we used a 1:1 ratio of the two as detecting probe for BPA.

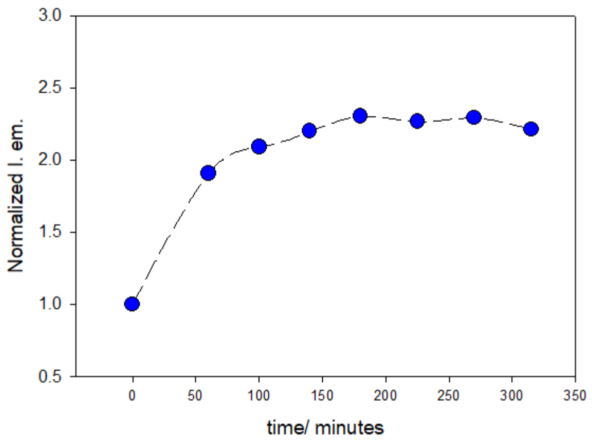

Figure 6.8: kinetic of equilibration of PluSNPs-HA@RB 1:1.) λexc = 530 nm; λem max = 580 nm. [HA@RB] = 1.26x10^{-7} M.

The HA-PluSNPs 1:1 shows a rather slow kinetic of equilibration. Indeed, at a concentration of 1.26x10^{-7} M it takes almost two hours to show a stable rhodamine emission, which is 2.5 times the initial signal due to interaction between PEG of PluSNPs and HA.

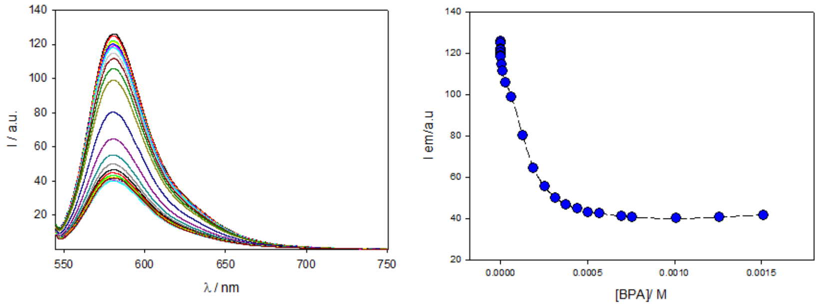

Figure 6.9 left: luminescence intensity of Rhodamine in PluSNPs-HA@RB (1:1) after equilibration and upon increasing concentration of BPA; right: trend of rhodamine maximum emission versus concentration of BPA.) λ_{exc} = 530 nm; $\lambda_{em\ max}$ = 580 nm. [HA@RB] = 1.26x10^{-7} M.

As it can be seen in figure 6.9, the probe shows an intense emission signal that strongly decreases upon addition of BPA. Going in details, a concentration of HA filament of 1.26x10^{-7} M corresponds to a concentration of rhodamine of 5µM and 28 dyes per filament (since the HA@RB DoF = 3.5%). In these conditions, in the BPA concentration range of 2.5x10^{-7} - 5x10^{-4} M a quenching of the rhodamine intensity up to 69% is observed, indicating that is possible to monitor a sub-µM concentration of the analyte. The system results stable and the interaction between BPA and PluSNPs-

HA@ROD appears fast during all the titration experiment. After $5x10^{-4}$ M, a plateau is reached, indicating that the all the sites of PluSNPs-HA@ROD were occupied.

Ideally, there are three possible mechanisms allowing the BPA detection: (i), BPA is selectively recognized by HA@ROD, (ii) both the PluSNPs and the HA are competing for the binding of BPA, and (iii) the PluSNPs-HA@ROD nanosystem binds BPA in a cooperative way.

In order to deeply investigate which of these possibilities is taking place, the experiments were repeated using PluSNPs@DEAC 0.5%.

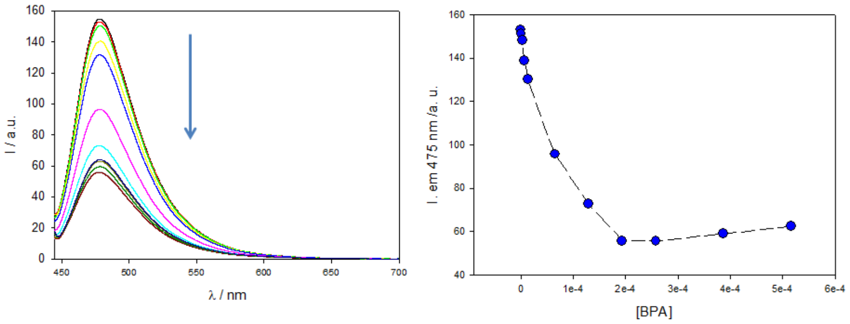

Figure 6.10: left: luminescence intensity of PluSNPs@DEAC upon addition of increasing concentration of BPA in water solution; right: luminescence intensity at 475 nm (maximum of DEAC emission peak) λ_{exc} = 430 nm; [PluSNPs] = $1.26x10^{-7}$ M.

PluSNPs show an intense emission peak in water. Upon addition of BPA, the luminescence intensity of DEAC is quenched. The overall decrease is of 60% up to $2x10^{-4}$ M of BPA. Higher concentrations do not lead to an additional quenching, thus the BPA concentration range in which PluSNPs shows a change in its fluorescence intensity – in these working conditions – covers 2 orders of magnitude of BPA concentration, starting from micro molar concentration.

Subsequently, the titration with BPA using the PluSNPs@DEAC-HA@RB as probe was carried out in the same conditions of the previous ones, thus mixing the two components of the probe in a 1:1 ratio.

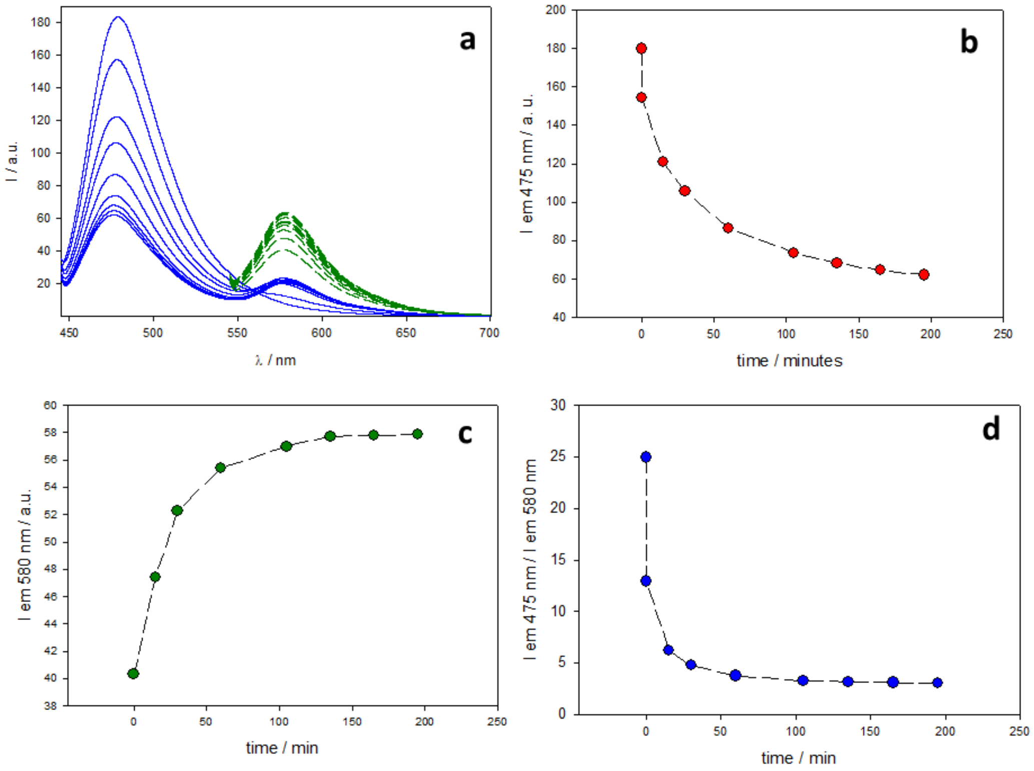

Figure 6.11: Kinetic of the equilibration process of PluSNPs@DEAC and HA@RB in 1:1 ratio at 1.26×10^{-7} M (λ_{exc} = 430 nm) (a); trend of the signal of DEAC at λ_{em} 475 nm *vs* time upon excitation at λ_{exc} = 430 nm (b); trend of the signal of RB at λ_{em} = 580 nm *vs* time upon its direct excitation at λ_{exc} = 530 nm (c);); trend of the signal of DEAC/RB at λ_{em} = 475 nm/580 nm *vs* time upon excitation at λ_{exc} = 430 nm (d).

After approximately 2 hours the emission of the two dyes remains constant over time, indicating that equilibrium of the system is reached. In figure 6.11b,c,d the variation of luminescence of both DEAC upon excitation at λ_{exc} = 430 nm and RB upon excitation at λ_{exc} = 530 nm are reported. Also, the ratio between the two emission signals upon excitation at λ_{exc} = 430 nm is shown. When DEAC is in close contact with RB, thanks to the good overlap between DEAC emission spectrum and RB absorption spectrum, DEAC emission can be quenched due to an energy transfer (ET) process and RB (acceptor) can be sensitised by the DEAC, acting as donor.

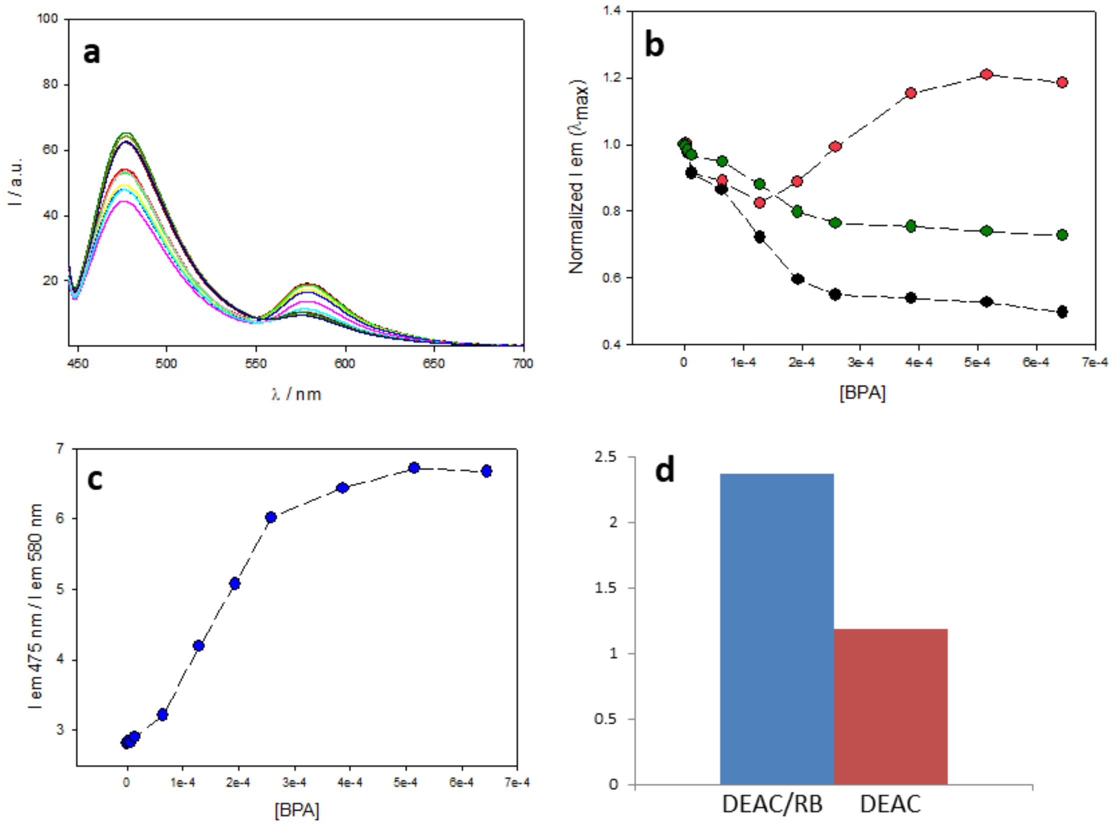

Figure 6.12: luminescence intensity of PluSNPs@DEAC-HA@RB 1:1 upon addition of increasing concentration of BPA in water solution (a); trends of luminescence intensities of DEAC (red dots, $\lambda_{exc} = 430$ nm, $\lambda_{em} = 475$ nm), rhodamine upon sensitization (black dots, $\lambda_{exc} = 430$ nm, $\lambda_{em} = 580$ nm), rhodamine upon direct excitation (green dots, $\lambda_{exc} = 530$ nm, $\lambda_{em} = 580$ nm) (b); ratio of luminescence intensities of DEAC/RB upon DEAC excitation ($\lambda_{exc} = 430$ nm)(c); bar plot of the signal increase of DEAC/RB ratio (blue) and DEAC (red) in the PluSNPs@DEAC-HA@RB 1:1 system (d).

Upon addition of BPA the overall trend (as shown in Figure 6.12 a) consists in a quenching of the RB, as observed when HA@RB alone is used as probe; at the same time, a partial recovery of the DEAC emission is observed.

Nonetheless, going into the details, up to $1\text{x}10^{-4}$ M of BPA, both the DEAC and the RB signals are slightly quenched. It’s noteworthy that the overall effect on DEAC dyes follows two opposite trends: the direct effect of BPA on DEAC is a quenching process, as explained for PluSNPs interacting with the target; on the other hand, the BPA hindering the ET from DEAC to RB would lead to a recover of the DEAC luminescence.

Therefore, the initial trend of DEAC emission can be either due to two situations: i) the most suitable environment for BPA is somewhere in the middle between

PluSNPs and HA and the increase of DEAC emission for lower ET and its quenching for direct interaction with BPA are balanced in a manner that creates the initial small decrease of DEAC emission; ii) even in a 1:1 ratio of PluSNPs and HA, there is a small fraction of nanoparticles not surrounded by HA; in this case the quenching observed is the result of the interaction of BPA with that fraction of nanoparticles, that, as already explained, causes the DEAC quenching. After the small fraction of nanoparticles is saturated, the main phenomenon is the interaction with hyaluronic acid with BPA, which therefore removes the polymer from the shell of nanoparticles.

This second option is also supported by the trends of RB emission. Upon its direct excitation (green dots in Figure 6.12) a quenching of only ca 13% is observed for [BPA]= 1x10^{-4} M, while for the same concentration of BPA a 22% decrease is reached in HA@RB alone system (figure 6.7, right). The minor effect observed on RB in the PluSNPs-HA system could be the due to the fact that although BPA mostly interacts PluSNPs-HA but also with the small fraction of PluSNPs alone.

Moreover, the trend of RB emission upon sensitization from DEAC (black dots in Figure 6.12b) is similar to the one obtained by direct excitation, but its quenching is the result of both RB quenching because of its direct interaction with BPA and RB quenching because of lower percentage of ET taking place from DEAC. Indeed a 28% decrease is observed.

Thus, only taking into account RB emission, using PluSNPs and HA joined together increases the sensitivity of the probe compared to HA@RB itself.

Moreover, although up to 1x10^{-4} M of BPA the DEAC signal is quenched, after this point it starts to increase again, indicating that upon BPA interaction with HA, it may sequestrate the polymer away from nanoparticles. Therefore, the more BPA is added the less HA surrounds nanoparticles and the less energy transfer occurs. The presence of a plateau region where nor DEAC nor RB emission signals change indicates that 4x10^{-4} M (3100 equivalents *vs* PluSNPs and HA) is the saturation point, thus the concentration at which all the interaction sites of the probe are occupied. Even in this situation an ET is still present from DEAC to RB (and a total recovery of PluSNP@DEAC emission is never observed).

Therefore, the use of PluSNPs boosts up the ability of HA to sequestrate BPA. Indeed, as previously explained, the HA results unfolded upon interaction with PluSNPs and this conformation makes it more accessible to BPA molecules.

Furthermore, this system allows to monitor at the same time two emission signals. The ratio between the two signals (i.e., intensity of DEAC emission / intensity of the sensitized RB emission, as in Figure 6.12c) further improves the ability of this reporter to detect smaller differences in the concentration of BPA in the range of activity of the probe. Indeed, in figure 6.12d, a comparison between the increase of DEAC/RB emission signal and the increase of DEAC at its maximum wavelength is shown: selectively monitoring the DEAC emission recovery, a 1.2 fold increase is observed; on the contrary, a 2.5-fold increase in the signal can be detected when the ratio DEAC/RB is analysed.

Despite also PluSNPs could be an efficient probe themselves (approximately a 60% decrease of emission is observed), it is worth to consider that using them joined with HA gives two advantages: the first is that the range of applicability of the probe is slightly larger for PluSNPs@DEAC-HA@RB compared to only PluSNPs@DEAC. Indeed, having the same LoD in the micromolar scale, the former can be suitable to detect up to $5x10^{-4}$ M of BPA versus $2x10^{-4}$ M of the PluSNPs alone; the second is that monitoring an increase of the signal is preferable, especially in complex matrices (as ground water) where other background noise could be present.

Considering all the results obtained so far, it seems that the third mechanism is taking place, thus using PluSNPs and HA together improves the sensing ability of the single partners, that work cooperatively to the sequestration and thus detection of BPA.

6.4 Conclusion

In this chapter two different approaches for BPA detection were studied. Both of them are built up using supramolecular chemistry strategies, thus creating adducts between BPA and the probe.

Thus, for what concern the dizinc complex, the appropriately design of the probe exploiting weak interaction such as hydrophobic interactions or metal coordination with ionisable molecules was proved to be able to detect BPA at neutral pH. At this pH the cyclen-coordinated Zn^{II} ions trigger the deprotonation of the two phenolic –OH of BPA, allowing their simultaneous coordination with the dizinc complex. Therefore, the $Ru^{II}(phen)_2bipy$ core can act not only as a spacer unit but also as a signalling moiety, since its luminescence signal is quenched upon BPA binding. Despite the overall variation of signal is not exceptional, this study demonstrated that metal complexes can be advantageous and promising approach to develop more efficient luminescent reporters for elusive analytes in aqueous solution, such as BPA.

The second system shown for BPA detection relies on some features of nanomaterials such as the high luminescence signal of dye-doped PluSNPs and their proven interaction with fluorescent HA derivatives.

PluSNPs@DEAC, for example, are nanomaterials very soluble in aqueous media thanks to PEG arms, but they also have hydrophobic regions in their inner shell able to host small organic molecules. Relying on this feature they were proved to be sensitive luminescent probe for BPA themselves. Furthermore, hyaluronic acid derivatized with rhodamine is a polymer that in water environment has a conformation that allows rhodamine molecules to allocate in HA hydrophobic pockets, leading to a noticeable quenching of the dye due to RB high local concentration. Similarly, it can host organic molecules such as BPA, that was proven to accumulate in this region leading to a further quenching of rhodamine.

Finally, combining in a 1:1 ratio these two nanomaterials, already able to somehow detect BPA *per se*, resulted in a sensitive probe to detect BPA, by monitoring two emission signals simultaneously changing and thus representing a promising ratiometric luminescence sensor.

In conclusion, both of the two probes demonstrate that the exploitation of supramolecular interaction can be a promising approach for the detection of emerging pollutants, as an efficient alternative to time-consuming analysis requiring sometimes difficult sample preparation. On the other hand, exploiting luminescent signal is a time saving and low equipment requiring way to detect BPA (and ideally other emerging pollutants) in water samples.

6.5 References

[1] V IÄ C T O R M A T A M O R O S A N D and J O S E P M . B A Y O N A, ‘Elimination of Pharmaceuticals and Personal Care Products in Subsurface Flow Constructed Wetlands’, *Environ. Sci. Technol.*, pp. 5811–5816, 2006.

[2] L. Gunnarsson, M. Adolfsson-Erici, B. Björlenius, C. Rutgersson, L. Förlin, and D. G. J. Larsson, ‘Comparison of six different sewage treatment processes—Reduction of estrogenic substances and effects on gene expression in exposed male fish’, *Science of The Total Environment*, vol. 407, no. 19, pp. 5235–5242, Sep. 2009, doi: 10.1016/j.scitotenv.2009.06.018.

[3] J. Michałowicz, ‘Bisphenol A – Sources, toxicity and biotransformation’, *environmental toxicology and pharmacology*, p. 21.

[4] S. Flint, T. Markle, S. Thompson, and E. Wallace, ‘Bisphenol A exposure, effects, and policy: A wildlife perspective’, *Journal of Environmental Management*, vol. 104, pp. 19–34, Aug. 2012, doi: 10.1016/j.jenvman.2012.03.021.

[5] L. N. Vandenberg, R. Hauser, M. Marcus, N. Olea, and W. V. Welshons, ‘Human exposure to bisphenol A (BPA)’, *Reproductive Toxicology*, vol. 24, no. 2, pp. 139–177, Aug. 2007, doi: 10.1016/j.reprotox.2007.07.010.

[6] L. Wang *et al.*, ‘A fluorometric aptasensor for bisphenol a based on the inner filter effect of gold nanoparticles on the fluorescence of nitrogen-doped carbon dots’, *Microchim Acta*, vol. 186, no. 1, p. 28, Jan. 2019, doi: 10.1007/s00604-018-3153-3.

[7] Y. Liu *et al.*, ‘Preparation of molecularly imprinted polymeric microspheres based on distillation–precipitation polymerization for an ultrasensitive electrochemical sensor’, *Analyst*, vol. 142, no. 7, pp. 1091–1098, 2017, doi: 10.1039/C7AN00059F.

[8] C. V. Esteves, D. Esteban-Gómez, C. Platas-Iglesias, R. Tripier, and R. Delgado, ‘Steric Effects on the Binding of Phosphate and Polyphosphate Anions by Zinc(II) and Copper(II) Dinuclear Complexes of *m* -Xylyl-bis-cyclen’, *Inorg. Chem.*, vol. 57, no. 11, pp. 6466–6478, Jun. 2018, doi: 10.1021/acs.inorgchem.8b00539.

[9] Marco Montalti, Alberto Credi, Luca Prodi, M. Teresa Gandolfi, ‘Handbook of Photochemistry, Chapter 4’, 3rd ed., Taylor & Francis, 2006.

[10] E. Rampazzo *et al.*, ‘Pluronic-Silica (PluS) Nanoparticles Doped with Multiple Dyes Featuring Complete Energy Transfer’, *J. Phys. Chem. C*, vol. 118, no. 17, pp. 9261–9267, May 2014, doi: 10.1021/jp501345f.

[11] F. Palomba *et al.*, ‘Specific, Surface-Driven, and High-Affinity Interactions of Fluorescent Hyaluronan with PEGylated Nanomaterials’, *ACS Appl. Mater. Interfaces*, vol. 12, no. 6, pp. 6806–6813, Feb. 2020, doi: 10.1021/acsami.9b17974.

Chapter 7 –

General conclusions

The key feature of nanomaterials is large surface/volume ratio which influences their optical, mechanical or magnetic properties. This unique characteristic of nanomaterials made them suitable for their use in a variety of fields, ranging from technology, computer science, food industry, telecommunications and medicine. Indeed, in the last decades the new discoveries in the field of nanomaterials opened up a series of new applications, such as their use as sensors. In particular, the possibility to tailor with high precision their interactions – both with small molecules or large macromolecules – can endow nanomaterial with high selectivity toward a target analyte. This feature, together with the possibility to obtain high signal amplification, which allow to reach great sensitivity, makes nanomaterial-based probes very attractive platforms for chemical and biological sensing.

The main challenges for a sensor are not only its sensitivity, stability and selectivity, but also its applicability in complex matrices and its ability to provide information about the target in an easy, cheap and time-saving way. Therefore, the conjugation of the advantages offered from nanomaterials with the benefits of optical transducers provides a new class of sensors.

During this PhD thesis, the detection of several targets as i) a protein associated with inflammatory states in cells (Part A); ii) synthesised nanomaterials; iii) double strand DNA from animal sample and hybrid DNA (Part B) and iv) a small molecule belonging to the family of the emerging pollutants (Part C) were studied exploiting different luminescent nanomaterials.

In the first part, an oligonucleotide sequence was specifically designed to bind NF-κB protein thanks to a consensus sequence. In this case the exploitation of FRET signal was proven to give qualitative information on the fate of NF-κB protein in live cells for at least 24 hours.

Indeed, binding states between the probe and the NF-κB causes a variation in the conformation of the triplex-hairpin probe that can be monitored in the complex environment of cells over time.

We demonstrated that the probe is efficiently delivered in the cytosol and in the nucleus of PC3 cells after 2 hours of incubation and it can recognize NF-κB protein in both the cells compartments. Interestingly, different rate of binding in the nucleus and cytosol can be observed. In fact the FRET signal recorded in the nucleus remained constant over all the time of the experiments, although after 12 hours the percentage of fluorescent cells drastically decreased. On the other hand, in the cytosol the FRET signal is evolving within 6 hours toward a low-FRET thus indicating binding events taking place.

In conclusion, despite improvements on the design of the triplex-hairpin can be performed to carry on a quantitative analysis on the FRET percentage, in this chapter was demonstrated that the hairpin-triplex probe used is a promising alternative to the most known studied double helix DNA hairpins.

In the part B of this thesis, the derivatization of hyaluronic acid with several luminescent dyes was performed, exploiting procedures of conjugation reactions through activating agents. In this way nanogels stable in aqueous solution were obtained and their photophysical characterization was provided.

We then investigated the interactions between each HA- derivatives and PluSNPs.

Considering the HA@dansyl, due to the dye solvatochromic properties, the derivatized nanogel showed strong changes in its photophysical properties upon interaction with nanoparticles, resulting a promising probe for the evaluation of the polarity of the surrounding environment.

In the case of pyrenes, we obtained different results using two amino-pyrene differing only for a one-carbon spacer. Interestingly, upon interaction with PluSNPs the HA@PA system showed a variation of intensity of emission of the static excimer and monomeric forms. On the other hand, the HA@PMA system did not show the formation of excimers, but instead a very intense emission of monomer. Then, upon titration with PluSNPs, variations in its luminescence and lifetimes were observed and related to an exposition of the dye to an environment having different rigidity and providing a different protection from the diffusion of oxygen.

To increase the potentialities offered by this toolbox, we investigated not only organic dyes, but also two ruthenium complexes; thus obtaining probes with relatively long lifetimes and a rich redox chemistry. Studying HA@Ru(bpy) interactions with PluSNPs it turned out that the photophysical properties of HA@Ru(bpy) did not change upon addition of nanoparticles but an interaction between HA@Ru(bpy) and PluSNPs could be detected by DLS analysis. Moreover, HA@Ru(bpy) interaction with double strand DNA was studied. Interestingly, the interaction was proved by a slight increase in the luminescence intensity and also from an increase in lifetime decay, due to the protection of the ruthenium complex from the oxygen quenching upon interaction with DNA.

On the other hand, since DPPZ is a known intercalator for DNA, the HA@Ru(DPPZ) was synthesised and its interaction with two different DNA samples was studied: a salmon sperm double strand DNA (dsDNA) having a sequence of 2000 base pairs and ha hybrid DNA having a sequence of 45 base pairs.

It turned out that the HA@Ru(DPPZ) is sensitive both toward a dsDNA and towards a hybrid DNA since its luminescence increases in both cases, with a higher sensitivity for salmon sperm DNA due to the longer sequence of this target.

Therefore, all the HA-derivatives proved to be promising nanomaterials for sensing applications in solution.

Moreover, not only nanomaterials were used as target, but also a small molecule was investigated. Indeed, since BPA belongs to the class of emerging pollutant (EP) – posing high concern for the environment ¬– its detection in water samples is of great interest. Thus, in the last section of this thesis two different approaches for BPA detection were studied. Both of them are built up using supramolecular chemistry strategies, thus creating adducts between BPA and the probe. At first, a dizinc complex was used, exploiting weak interaction such as hydrophobic interactions or metal coordination with ionisable molecules and it was proved to be able to detect BPA at neutral pH thanks to the simultaneous coordination of the two -OH groups of BPA with the dizinc complex. Moreover, since the $Ru^{II}(phen)_2bipy$ core can act as a spacer unit for the two zinc atoms but also as a signalling moiety, its luminescence signal was proven to be slightly quenched upon BPA binding. This complex thus demonstrated to be a promising tool for the detection of BPA.

Finally, we tested systems constituted by HA@RB, PluSNPs@DEAC separately and in combination among them, as sensor for BPA. Indeed, combining in a 1:1 ratio these two nanomaterials, already able to somehow detect BPA per se, resulted in a sensitive probe to detect BPA, by simultaneously monitoring the variation of two emission signals and thus representing a promising ratiometric luminescence sensor.

In conclusion, in this PhD thesis I focused on the synthesis and characterization of luminescent nanomaterial-based probes. Moreover, their sensing ability in solution and (in the case of triplex-hairpin) also in complex biological environment were proved.

The results presented in this PhD work prove that natural occurring polymers properly derivatized are highly promising tools in the sensing field and they are efficiently able to detect both macromolecules of biological interest and small molecules of environmental concern. Therefore this research represents a first encouraging step towards the design of improved optical sensors for environmental and biomedical applications.

APPENDIX - PRYNCIPLES OF PHOTOPHYSICS

A.1 ELECTRONIC EXCITED STATE - JABLOSNKY DIAGRAM

Electromagnetic radiation and matter can interact in different ways. Photochemistry is interested in the conversion of the energy (hν) of a photon absorbed by a chemical species in electronic energy, causing the transfer of an electron toward an orbital having higher energy. The species turns from its electronic ground state A to an electronic excited state A*, which possesses a different electronic configuration:

$$A + h\nu \rightarrow A^*$$

This different electronic distribution causes the excited states of a chemical species to have physicochemical properties so different from those of the ground state that they can be considered different chemical species. For this reason, it is possible to define photochemistry as the chemistry of excited states. A photon can be absorbed and provoke the formation of an electronic excited state only if its energy hν exactly corresponds to the energy difference between the excited and the ground state. Absorption electronic transitions occur in a time scale of the order of femtoseconds (10^{-15} s, Franck Condon Principle), creating excited states which are transient and can deactivate in different ways, shown in the Jablonski diagram (Figure 1). In this diagram electronic states (the singlets S0, S1 and the triplet T1) are represented by thicker lines. The distinction between states with different spin multiplicity is due to the fact that transitions between these states are partially not allowed. Thinner lines represent the vibrational levels of the electronic states. After the energy absorption and reaching an excited vibrational level of an S2 electronic excited state, the molecule goes rapidly ($< 10^{-12}$ s) to the ground vibrational level of that excited state (vibrational relaxation); then internal conversion occurs, passing from the ground vibrational level of S2 to the isoenergetic vibrational level of S1, the electronic state at lower energy ($< 10^{-12}$ s). Another vibrational relaxation is then observed toward the ground vibrational state of S1, and at this stage the excited molecule can deactivate in two ways:

1- Non-radiative deactivation: the energy is released as vibrational energy generating heat. If this process occurs between two states with the same spin multiplicity, the process is called internal conversion (10^{-12}-10^{-6} s) and it , while if the states have different spin multiplicity the phenomenon is known as intersystem crossing (10^{-11} -10^{-6} s). The following vibrational relaxation leads in the first case to the ground vibrational level of S0, in the second case to that of T1;

2- Radiative deactivation: it is a process that generates luminescence and it is defined fluorescence if it occurs between states with the same spin multiplicity, phosphorescence if it occurs between states with different spin multiplicity. Similarly to S1, T1 can deactivate to S0 by radiative deactivation (phosphorescence, 10^{-4}-10^{2} s) or by non-radiative deactivation (intersystem crossing, 10^{-3}-10 s, and successive vibrational relaxation to S0). Long-lived states such as T1 can undergo photochemical reactions, for example with oxygen, producing other chemical species. Generally speaking, since the time scale to decay to S1 and T1 are shorter than that necessary to pass from S1 and T1 to S0, only lowest energetic states of each spin multiplicity (that is S1 and T1) live enough to undergo luminescence (Kasha's rule) or photochemical reactions[1].

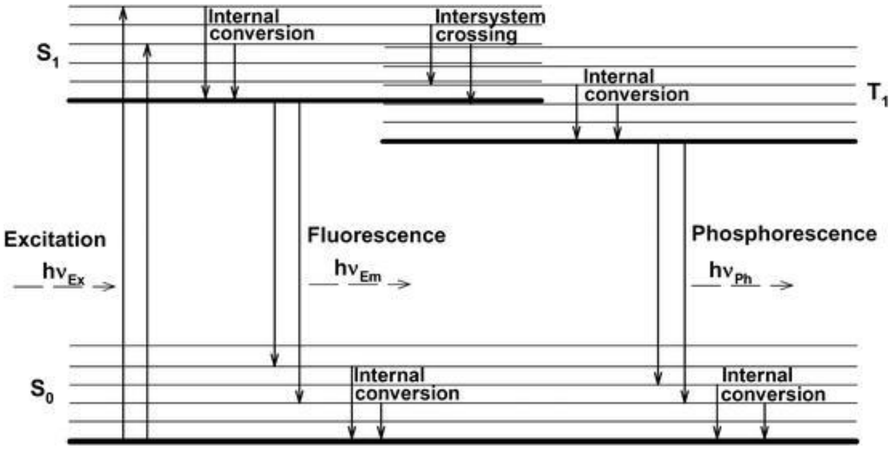

Figure 1. Jablonsky diagram for a generic molecule: horizontal lines symbolizes the vibrational levels in the electronic ground state (S_0), in the first (lowest) excited singlet state (S_1) and in the first excited triplet state (T_1).*Vertical arrows* represent transitions between levels. [2]

A.2 SOLVATOCHROMISM

Many relevant chemical and physical phenomena such as thermodynamics and reaction kinetics, as well as the position and intensity of the electronic absorption and emission bands, are often strongly dependent on the solvent. The basis of these effects on chemical equilibria and spectroscopic properties is the solvation of reagents and products. The solvation depends on the intermolecular forces between solute and surrounding solvent molecules, which include non-specific forces, such as electrostatic and polarization forces, and specific forces such as hydrogen bonds. The influence of solvents on the chemical equilibrium position was discovered in 1896 by Claisen and Wislicenus independently of each other. *These* results were examined by Stobbe, who in 1903 divided the solvents into two groups, based on their ability to isomerize some tautomeric compounds, with subsequent subdivision in solvent donors of hydrogen bonds (HBD, protic solvents) and non-hydrogen bond donors (non-HBD, aprotic solvents). Hantzschlater instead observed the displacement of the absorption and emission maxima at longer or shorter wavelengths of some molecules (fluorophores) as the polarity of the solvation environment varies.

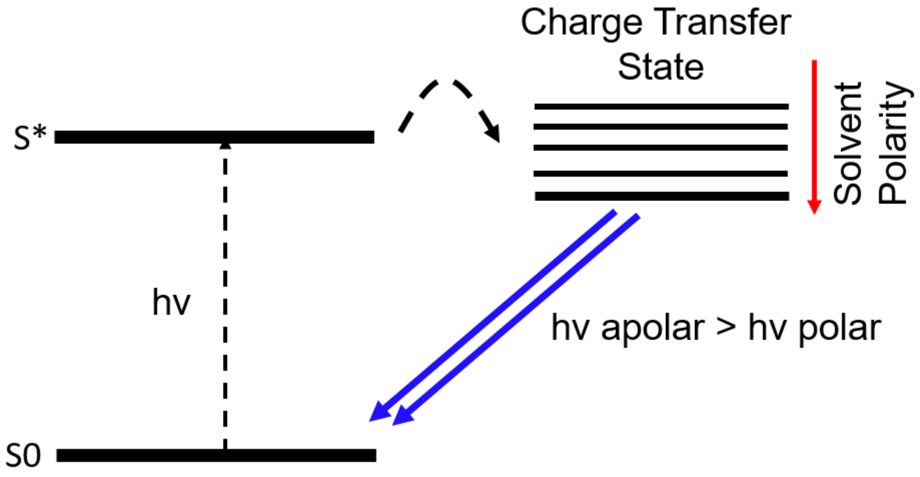

Figure 2. Schematization of Jablonsky diagram for a positive solvatochromic dye

This phenomenon has taken the name of solvatochromism. The solvatochromism manifests itself in molecules having a different dipole moment for the ground state and the excited state. Solvents can therefore stabilize the two electronic states in a different proportion, thus varying the energy gap between them and therefore the energy of the transition. In general, the transitions between two states, both in absorption and in emission, take place in a very short time, much lower than that of the motion of the nuclei, therefore considered to be stationary. Therefore, there is no reorganization of the solvent molecules causing the scheme of solvation of the excited state and that of the ground state to remain unchanged (Frank-Condon principle). However, if the residence time in an excited state is large enough, a reorientation of the solvent molecules can occur, with associated internal conversion, which brings the molecule into a lower energy vibroe-lectronic state and, from this new energy level, it can take place a radiative relaxation with fluorescence emission that brings the molecule to the ground state[3]. In this case, the energy emitted by the solvatochromic dye molecule will be as low as the stabilization effect of the excited state operated by the solvent is greatest. There are two types of solvatochromism, negative and positive. If, as the solvent polarity increases, the fundamental state of the molecule is more stabilized than its first excited state, we observe hypsochromic shift (towards high energies in the spectrum) and the solvatochromism is called negative. Vice versa, if as the solvent polarity increases the excited state is stabilized more than the fundamental one, the solvatochromism is called positive and we observe a batochromic shift (towards low energies). The solvatochromic probes are widely used for the study of polarity in complex systems or in the diagnostic field as bioluminescent sensors in imaging techniques [4], [5].

A.3 ELECTRONIC EXCITATION ENERGY TRANSFER

With the term electronic excitation energy transfer we indicate the process in which an excited molecule of a donor D* decays to its ground state D with the simultaneous transfer of its excitation energy to a molecule of acceptor A, which is thus led to an excited state A*:

$$D^* + A \to D + A^*$$

it is possible to observe this phenomenon exciting D in a spectral region in which it absorbs but A does not: if energy transfer occurs, D* emission is quenched and at the same time the appearance of the emission of A* is observed, which is called sensitized emission. In the case in which D and A are different molecules of the same chemical species we speak about homo energy transfer. It is possible to observe also intramolecular energy transfer in the case of a (super)molecule containing a donor and an acceptor, separated by a spacer L:

$$D^* - L - A \ \to \ D - L - A^*$$

Two possible mechanisms of energy transfer exist, radiative one and non-radiative one. The radiative mechanism (also called trivial energy transfer) does not require the direct interaction of D and A, but it occurs via the electromagnetic field produced form the photons emitted by D, which can be absorbed by A, provided that an overlap between the emission spectrum of D and the absorption one of A exists. This mechanism consists of two different steps:

$$D^* \to \ D + h\nu' \ \text{(Emission of the Donor)}$$

$$A + h\nu' \to \ A^* \ \text{(Absorption of the Acceptor)}$$

It is possible to correlate the probability of absorption of A of a photon emitted by D*, that is the probability of energy transfer ($a_{D^*\to A}$), with the overlap between the emission spectrum of D and the absorption one of A. In particular a relation stands between $a_{D^*\to A}$ and the overlap integral J, defined as

$$J = \int_0^\infty F_D(\lambda)\varepsilon_A(\lambda)\lambda^4 d\lambda$$

where F_D is the normalized emission spectrum of D (the area under the spectrum is equal to 1) and $\varepsilon_A(\lambda)$ is the absorption spectrum of A in $dm^3 \cdot mol^{-1} \cdot cm^{-1}$. So as J increases, the probability of radiative energy transfer linearly increases. This probability is also directly proportional to the concentration of A, to the optical path length and inversely proportional to the luminescence quantum yield of D. The radiative energy transfer can occur over extremely long distances: solar irradiation on Earth is a striking example. It is necessary that the transition of absorption in the acceptor is spin-allowed so that the radiative energy transfer can occur: thus singlet(D*)-singlet(A*) and triplet(D*)-singlet(A*) transfers are allowed, while singlet(D*)-triplet(A*) and triplet(D*)-triplet (A*) transfers are not allowed.

The *non-radiative mechanism*, on the other hand, requires an intermolecular interaction between D and A mediated by the electromagnetic field. The energy transfer between the partners occurs in resonance conditions, involving isoenergetic non-radiative transitions between D* and A. Also in this case the probability of energy transfer is directly proportional to J. The theoretical description of the process leads to obtain that the interaction between D* and A consists of a Coulombic term (Förster mechanism) and of an exchange term (Dexter mechanism) (Figure 3).

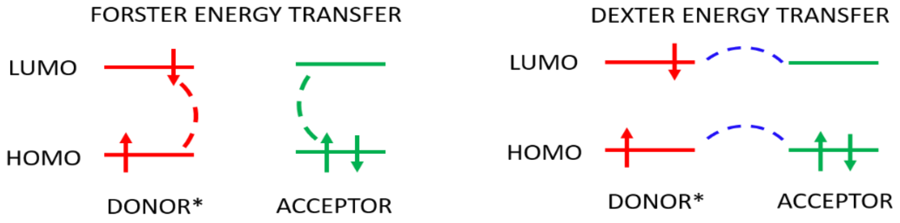

Figure 3. energy transfer via Coulombic mechanism (left) and with exchange mechanism (right)

The Coulombic mechanism arises from the coupling of the electronic transition moments of electric dipole of the transitions D*->D and A->A*. This interaction is governed by Förster's equation, which correlates the energy transfer kinetic constant with the distance R_{DA}:

$$k_{ET} = \frac{1}{\tau_D}(\frac{R_0}{R_{DA}})^6$$

Where τ_D is the lifetime of the donor in the absence of the acceptor and R_0 is the Förster distance, that is the distance between D and \A at which the energy transfer rate (k_{ET}) is equal to the decay rate of the donor in the absence of the acceptor ($k_{ET} = \frac{1}{\tau_D}$). At this distance half of the molecules of D decay via energy transfer. Förster distance is correlated to the overlap between the emission spectrum of D and the absorption spectrum of A by means of the following relation:

$$R_0^6 = 2.303\,\frac{9000\,\chi^2 \Phi_D}{n^4 N_A 128\pi^5}\,J$$

Where χ is the orientational factor which describes the relative orientation of the electric dipole moment of D and A (it is assumed to be equal to 2/3 in the case of freely rotating D and A), Φ_D is the fluorescence quantum yield of D in the absence of A, n is the refractive index of the solvent, N_A is the Avogadro's constant, is the luminescence spectrum of D normalized to 1m and J is the spectral overlap. The higher the overlap between the emission spectrum of A and the absorption spectrum of A, the higher the value of R_0. Typical values are about 20-100 Å. It is possible to define an efficiency of energy transfer

$$\eta = \frac{k_{ET}}{k_{ET} + k_D}$$

which is linked to R_{DA}^6 by means of the following relation

$$\eta = \frac{R_0^6}{R_0^6 + R_{DA}^6}$$

which highlights that the efficiency of the energy transfer process is equal to 0.5 when $R_{DA} = R_0$. It is possible to experimentally obtain η from the fluorescence quantum yield of D in the presence of A (Φ_{DA}) and in its absence (Φ_D), or from lifetimes in the two conditions (τ_{DA} , τ_D):

$$\eta = 1 - \frac{\Phi_{DA}}{\Phi_D}$$

$$\eta = 1 - \frac{\tau_{DA}}{\tau_D}$$

The processes of Förster type energy transfer are generally allowed if the transition in D and in A does not involve spin changes of the single species. On the contrary Dexter type energy transfer dominates. The exchange interaction requires a simultaneous double electronic exchange involving the LUMO of D and the HOMO of A (Figure 3) and it is a short-range interaction, becoming important when R_{DA} is ≤ 5 Å. According to Dexter model, the kinetic constant for the exchange mechanism decays exponentially with R_{DA} :

$$k_{ET}^{ex} = \frac{2\pi}{\hbar} K J^{ex} e^{\frac{2R_{DA}}{L}}$$

where K is a factor related to the specific orbitalic interaction, J^{ex} is the normalized overlap integral and L is an average Van der Waals radius which simulates molecular dimensions[6].

A4 ELECTRONIC ABSORPTION SPECTRA

For the acquisition of electronic absorption spectra, a double beam spectrophotometer UV/Vis Perkin Elmer Lambda-45 was used. The amount of light absorbed is provided by the ratio of the intensity of incident light (I_0) and the intensity of transmitted light (I_t) and is expressed by Absorbance (A):

$$A = log_{10} \frac{I_0}{I_t}$$

A is related to the chromophore concentration by the Lambert Beer equation as following:

$$A = c\varepsilon l$$

Where c is the chromophore concentration express in mol/L, ε is the molar extinction coefficient (mol/L)$^{-1}$cm^{-1} and l is the optical path of the sample (1 cm optical path of the cuvette).

A5 LUMINESCENCE QUANTUM YIELD

The registration of the emission and excitation spectra were performed using a spectrofluorimeter Perkin Elmer LS55 and a spectrofluorimeter Edinburgh FLS920.

An important parameter to photophysically characterize samples is ttheir luminescence quantum yield (Φ_{PL}, QY), defined as the ratio between the number of emitted photons over the number of photons absorbed by a species at the same excitation wavelength:

$$\Phi_{PL} = \frac{number\ of\ emitted\ photons}{number\ of\ absorbed\ photons}$$

A fast and useful method to determine the luminescence quantum yield is to compare the emission of a sample with a reference species having a known quantum yield, upon excitation of both reference and sample at the same wavelength. The chosen reference has to emit in the same spectral region of the sample and the emission spectra must be recorded in the same experimental conditions. For the assessment of Φ_{PL} we adopted the following experimental procedure: the absorption spectra of the sample and of the reference were registered and, when possible, isoabsorption points were used as excitation wavelength for the registration of emission spectra. The following equation was used to determine the value of luminescence quantum yield:

$$\Phi_{PL} = \Phi_{ref} \frac{I_x}{I_{ref}} * \frac{A_{ref}}{A_x} * \left(\frac{n_x}{n_{ref}}\right)^2$$

Where Φ_{ref} is the fluorescence QY of the reference, I_{ref} and I_x are the emission intensities of the reference and the sample, respectively; A_{ref} and A_x are the absorbance at the excitation wavelength of the reference and the sample; n_{ref} and $n_x$are the refractive index of the solvents.

A6 EXCITED STATE LIFETIME MEASUREMENTS

Excited state lifetime measurements were performed using a spectrofluorimeter Edinburgh Analytical Instruments FLS920, equipped with a time-correlated single-photon counting device, which is able to measure lifetimes in a range between 0.5 ns and 30 µs. The time-correlated single-photon counting is based on the probability that a single photon emitted by a luminescent sample is collected by a proper high sensitivity detector: this probability is statistically correlated with the variation of the concentration of the excited states in solution.

A.7 DYNAMIC LIGHT SCATTERING

Dynamic Light Scattering (DLS) measurements were performed using a Malvern Instruments DLS ZetaSizer Nano-ZS (Figure 5). With this instrument it is possible to determine the dimension of particles having a diameter between 1 nm and 10 µm.

It exploits the study of Brownian motions to determine the hydrodynamic diameter of particles suspended in solution. The hydrodynamic diameter is obtained by the correlation of the scattering intensity fluctuations recorded over time upon irradiation of the sample with a 633 nm laser. The Brownian motion of the particles is described by translational diffusion coefficient (D) that is related to the hydrodynamic diameter through the Stokes-Einstein’s equation

$$d(H) = \frac{kT}{3\pi\eta D}$$

where d(H) is the hydrodynamic diameter, k is the Boltzmann constant, T is the temperature, η(T) is the viscosity of the solvent and D is the diffusion coefficient.

Through this equation the hydrodynamic diameter, thus the diameter of a sphere having the same diffusion coefficient of the particles, can be obtained. The fluctuation of the instensity of the scattering produced in a short time-scale is analysed using the correlation function.

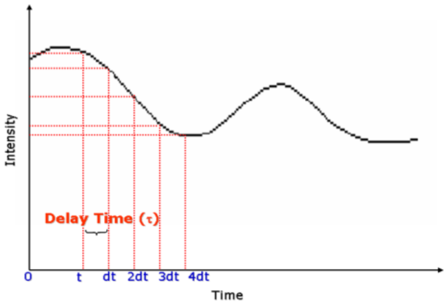

$$G(\tau) = \int_0^{\infty} I(t) \cdot I(t+\tau)dt$$

Figura 4 - Funzione di correlazione G, rappresentazione grafica e formula matematica.

The correlation indicates the degree of similarity of two measurements at different times. For particles of higher dimensions, the correlation will last for longer times than in the case of smaller particles.

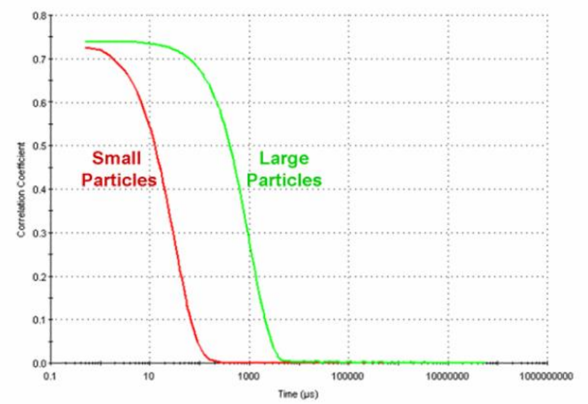

Figura 5 – trend of the correlation coefficient for large particles (green line) and small particles (red line) versus time

The particle size distribution is obtained from the relative scattering intensity graph of the several particle size classes (intensity size distribution). It is also possible to obtain this distribution as a function of particle volume, or particle number. Let us consider, for example, a sample containing two populations of spherical particles having a diameter of 5 and 50 nm respectively and present in the same number (Figure 4). As far as the number of particle is concerned, the graph consists of two peaks, one at 5 nm and the other at 50 nm, with a 1:1 ratio. If we convert the number distribution in volume distribution, the two peaks ratio is 1:1000, because the volume of a sphere is equal to $\frac{4\pi}{3}\left(\frac{d}{2}\right)^3$. If we switch to intensity distribution, the ratio becomes equal to 1:106 according to Rayleigh approximation.

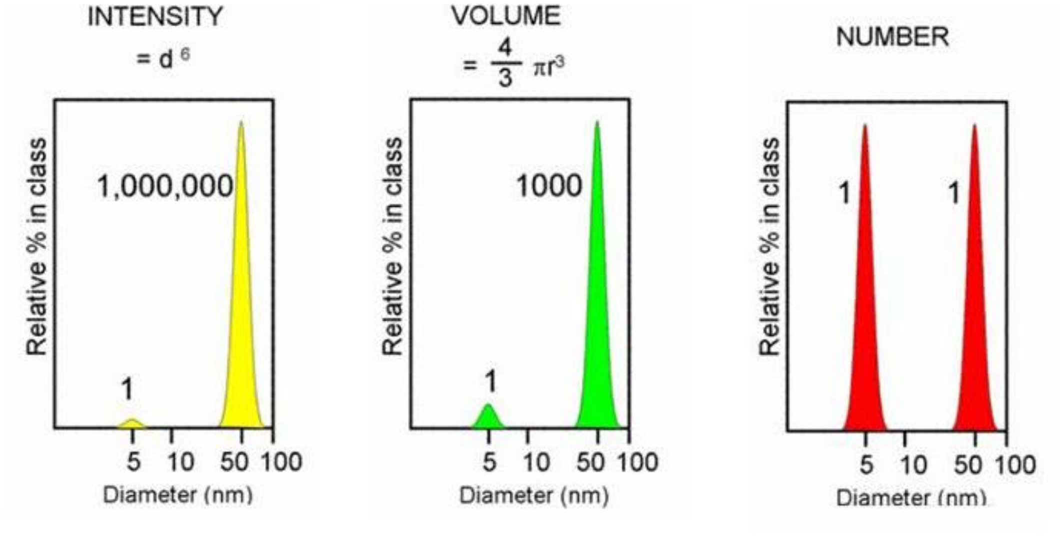

Figure 6: number, volume and intensity distribution of a sample containing spherical particles of 5 nm and 50 nm diameter in equal numbers.

REFERENCES

[1] M. T. G. Marco Montalti, Alberto Credi, Luca Prodi, Handbook of Photochemistry, Third Edition, Taylor & Francis, Third edit., 2006.

[2] Usai C., Diaspro A. (2013) Fluorescence: General Aspects. In: Roberts G.C.K. (eds) Encyclopedia of Biophysics. Springer, Berlin, Heidelberg. https://doi.org/10.1007/978-3-642-16712-6_823

[3] E. Buncel and S. Rajagopal, Acc. Chem. Res., 1990, 23, 226–231.

[4] L. Malacrida, D. M. Jameson and E. Gratton, Sci. Rep., 2017, 7, 1–11.

[5] O. Golfetto, E. Hinde and E. Gratton, Biophys. J., 2013, 104, 1238–1247.

[6] J. R. Lakowicz, Principles of Fluorescence Spectroscopy, Springer US, 3rd editio., 2006.